Synthesis and photocatalytic properties of TiO2/BiVO4 nanocomposites and heterostructures

Drisya Karathuparathottathil Damodharan

DOCTORAT MATIERE BRETAGNE MOLECULES LOIRE ET MATERIAUX

Le Mans Université

THESE DE DOCTORAT(COTUTELLE)

Cinvestav

LE MANS UNIVERSITE
COMUE UNIVERSITE BRETAGNE LOIRE

ECOLE DOCTORALE N° 596
Matière, Molécules, Matériaux
Spécialité : «Physique »
Date de Soutenance 31 Mars 2021

Par
« Drisya Karathuparathottathil Damodharan »

Synthesis and photocatalytic properties of $TiO_2/BiVO_4$ nanocomposites and heterostructures

Thése N^0 :2021LEMA1011

Rapporteurs avant soutenance :

Pablo Taboada,	Professor, Faculty of Physics, University of Santiago de Compostela, Spain
José A. Chávez Carvayar	Professor, Instituto de Materiales, UNAM, Mexico

Composition du Jury:

Président :	Maria de la Luz Olvera Amador	Professor Department of Electrical Engineering, Cinvestav - Mexico
Examinateurs :	Sylvain Marinel	Professor, Laboratoire CRISMAT, Université de CAEN NORMANDIE,
	Maria de la Luz Olvera Amador	Professor Department of Electrical Engineering, Cinvestav, Mexico
	Arturo Maldonado Alvarez	Professor Department of Electrical Engineering, Cinvestav, Mexico
	Pablo Taboada,	Professor Faculty of Physics, University Santiago de Compostela, Spain
	José A. Chávez Carvayar	Professor, Instituto de Materiales, UNAM, Mexico
Co-Encadrant	Mathieu Edely	PhD Resarch Engineer , IMMM- Le Mans, France
Dir. de thèse :	Velumani Subramaniam	Professor, CINVESTAV-IPN, Av.IPN 2508, Mexico City, Mexico
Dir. de thèse :	Abdelhadi Kassiba	Professor, IMMM-Le Mans, France

Acknowledgement

First, I would like to express my sincere gratitude to my thesis advisor Dr. Velumani Subramaniam from CINVESTAV- Mexico for this great opportunity, his ceaseless support, exceptional guidance, and encouragement throughout the period of doctoral studies. For the Ph.D. Co-graduation program, I am extremely grateful to my advisor from Le Mans University Prof. Abdelhadi Kassiba for providing a great learning and research experience along with his excellent guidance throughout the realization of the Ph.D. research works.

Besides my advisors I sincerely thank Dr.Eng. Mathieu Edely for his precious guidance during my research stay in Le Mans University.

I would like to express my sincere thanks to the reviewers of my Ph.D. thesis Prof.Pablo Taboada and Prof. Jose Chavez Carvayar and to the Jury members Prof.Sylvain Marinel, Prof. Maria de la luz Olvera Amador, Prof. Arturo Maldonado Alvarez

I would like to extend my gratitude to Dr.R.Sathyamoorthy (Kongunadu Arts and Science College, Coimbatore, India) for his trust in me that has made all this possible.

I wish to acknowledge CONACYT for the financial support for the whole period of my Ph.D. Also, Conacyt-Sener 263043 project, SEP-Cinvestav 200 and IMMM Le Mans for their financial support.

I thank the Ph.D. committee members, from CINVESTAV, Dra. Maria de la luz Olvera Amador, Dr. Arturo Maldonado Alvarez, Dr. Jose Saul Arias Ceron, Dr. Mauricio Ortega and Dr. Jose Chávez Carvayar, and from France, Prof. Jens Dittmer for their valuable comments and suggestions on this work.

Also, my sincere thanks go to all the administrative staffs from CINVESTAV- IPN, Zacatenco and Le Mans University, France.

I extent my gratitude to Dr. Anthony Rousseau for HRTEM and Dr. Sandy Auguste, for the High temperature XRD measurement (Le Mans University) and her being a good friend of me.

Also, I take this opportunity to thank Dr. Jaime Vega for his technical assistance and Miguel Galvan for the Raman analysis, Miguel Luna for profilometry analysis and Dr. Juan Carlos Duran Alvarez from UNAM for the BET and electrochemical characterizations.

Next, I would like to thank my dear friends and colleagues, Myriam Solís- Lopez, Francisco Alvarado César, Christeena Theresa Thomas, Mercy Rani Babudurai, Araceli- Romero Nunez, Atzin Ferrel, Ashok Adikari, Ganesh Regmi, Karthik Sekar, Michael Onyekachi Nwakanma, Jorge Rios Ramirez, Roberto Hernandez Maya, Jorge Narro, Alejandra, Fernanda, Dorian, Hugo, Francisco Javier, Javier covarrubias, , Rohini Neendoor Mohan, Aruna Devi, Latha Marasamy, Ravichandran for all their help throughout these years.

I am thankful to my dear friends from Le Mans University, Wafae Halim, Manel Missaoui, Jiangguli Peng, Paula Pamies, Sandeep Sathyan, Zhuo Yu, Wei Li for making my Co-graduation research stay memorable.

I wish to express all my love and gratitude to the family of Sra. Elvira Gonzalez Garcia for being my support system and also for her encouraging words. And I thank Family of Sra. Celia César Mauleón for being the helping hand in many situations. I take this opportunity to thank both of them for making me feel safe and considering as a family member.

Also, I am thankful to the Family of Dr. Velumani Subramaniam, especially to his wife Malathy ma'am for such relaxing lovely talks and gatherings.

No words will be enough to express my love and gratitude to Mr. Ravi Prakash, Sajna, Aneesh, Shyam, KPG Associates- Mumbai, and their family members for their unconditional love, support and constant encouragement.

Last, but not the least it's my pleasure to acknowledge my parents (Damodharan K.T & Girija Damodharan), brothers (Anand & Aravind), Uncle (Krishna Mohan), Aunt (Smitha) and my beloved grandmother (Bhageerathi Amma) for their prayers and blessings that always accompanied me throughout this journey.

List of Publications

- K.T. Drisya, M. Solís -López, J.J Ríos - Ramírez, J.C. Durán - Alvarez, A. Rousseau, S. Velumani, R.Asomoza, A.Kassiba, A. Jantrania, H. Castaneda, *Electronic and optical competence of $TiO_2/BiVO_4$ nanocomposites in the photocatalytic processes*, Sci. Rep. 10 (2020) 13507. 10.1038/s41598-020-69032-9

- Araceli Romero-Núñez, Juan Carlos Durán-Álvarez, K.T. Drisya, Myriam Solís-López and S. Velumani *Introduction to Photocatalysis and $BiVO_4$ Based Materials for Visible Light Photocatalysis,* Sustainable Materials Solutions for Solar Energy Technologies – ELSEVIER- Accepted
- K.T. Drisya, Thomas Ch-Th, M. Solís-López, A. Romero-Núñez, S. Velumani, *Characterization of $BiVO_4$ Modified TiO_2 and its Application in the Water Treatment,* 2020 17th International Conference on Electrical Engineering, Computing Science and Automatic Control (CCE). Mexico City, 978-1-7281-8987-1/20/$31.00 ©2020 IEEE
- T Ch-Th, K.T. Drisya, M Solís-López, A Romero-Núñez, S Velumani, *GO/$BiVO_4$ Nanocomposites for Escherichia coli K12 photocatalytic inactivation,* 2020 17th International Conference on Electrical Engineering, Computing Science and Automatic Control (CCE). Mexico City, 978-1-7281-8987-1/20/$31.00 ©2020 IEEE

Participation in the conferences

- K.T Drisya, M. Solís-López , R. Hernádez-Maya, J.C Durán Álvarez, Abdel Hadi Kassiba, S.Velumani, 'Photocatalytic oxidation of Arsenic(III) in water using the sol-gel synthesized $BiVO_4/TiO_2$ nanocomposite' symposium F2 (SF2-0025 oral presentation), Advances in Functional Semiconducting Materials at the XXVII International Materials Research, IMRC 2018 August 19 - 24, Cancun, Mexico-**Oral presentation**
- K.T Drisya, M. Solís-López, R. Hernádez-Maya, S.Velumani , Jorge Sergio Narro Rios, Francisco Alvarado Cesar, 'Synthesis and characterization of $BiVO_4/TiO_2$ thinfilms' symposium F2(SF.2 P030- Poster presentation), Advances in Functional Semiconducting Materials at the XXVII International Materials Research Congress, IMRC 2018 August 19-24 , Cancun, Mexico -**Poster**
- K.T.Drisya, Christeena Th-Th, M. Solís-López, R. Hernádez-Maya,'Chromium removal from drinking water using red mud as adsorbent' (Poster presentation) ICSWTN - 2018, CIVESTAV, Mexico city -**Poster**
- KT. Drisya, M. Solís-López, R. Hernández-Maya, S. Velumani, 'Photocatalytic AB113 Removal Properties of $BiVO_4$ /TiO_2 nanocomposites' Symposium F8, XXVI International Materials Research Congress, IMRC 2017 August 20-25, Cancun, Mexico -**Poster**

- M. Solís-López, KT. Drisya, R. Hernádez-Maya, P. Reyes, S. Velumani, 'Photocatalytic Orange-G degradation using $TiO_2/BiVO_4$ as photocatalyst' Symposium F8, XXVI International Materials Research Congress, IMRC 2017 August 20-25, Cancun, Mexico-**Poster**
- KT. Drisya, M. Solís-López, S. Velumani, S. Auguste, M. Edely, A. Rousseau, A. Kassiba 'Sputter deposition and characterization of TiO_2-$BiVO_4$ heterostructures for visible light driven photocatalysis' SF NANO-C'NANO Dijon, France December,2019 -**Poster**
- KT. Drisya, M. Solís-López, S. Auguste, M. Edely, A. Rousseau, A. Kassiba, Velumani. 'Sputter deposition and characterization of TiO_2-$BiVO_4$ heterostructures for visible light driven photocatalysis', MREB Taller 2020, Cinvestav- IPN , Mexico city -**Poster**

Abbreviations

Pc	Photocatalytic
Pb	Lead
Cr	Chromium
Cd	Cadmium
Zn	Zinc
Fe	Iron
Mn	Manganese
As	Arsenic
Hg	Mercury
AS(V)	Arsenate
As(III)	Arsenite
BOD	Biological Oxygen Demand
UV	Ultra Violet
VB	Valence band
CB	Conduction band
TO	Titanium dioxide
BVO	Bismuth vanadate
eV	Electron volt
Rf	Radio frequency
AB113	Acid blue 113
g/1	Gram per Litre
OCP	Open Circuit Potential
AOP	Advanced Oxidation Potential
IUPAC	International Union of Pure and Applied Chemistry
IR	Infra Red
SC	Semiconductor
Eg	Band gap energy
e^-	Electron
h^+	Hole
$OH^{\cdot}$	Hydroxyl ion
O_2^-	Superoxide radical
Eqn	Equation

NHE	Normal Hydrogen Electrode
SHE	Standard Hydrogen Electrode
Nm	Nanometer
CBM	Conduction band minima
VBM	Valence band maxima
Abs	Absorbance
Vis	Visible
A^o	Angstrom
RSM	Response surface methodology
CCD	Central composite design
AlPO	Aluminium Phosphate
ANOVA	Analysis of variance
ml	Millilitres
cms	Centimetres
Pa	Pascal
w	Watts
d	Interplanar distance
Ɵ	Bragg angle
k	Shape factor
D	Crystallite size
λ	Wavelength
FWHM	Full width half maximum
HOMO	Highest occupied molecular orbitals
LUMO	Lowest occupied molecular orbitals
kV	Kilo volt
BF	Bright field
DF	Dark field
FFT	Fast fourier transform
SAED	Selected area diffraction
Z	Atomic mass
mm	Millimetres
M	Molar
Hz	Hertz

KHz	Kilo hertz
kW	Kilo watts
Mg/Ll	Milligrams per litre
µL	Microlitre
a.u	Arbitrary unit
m-BVO	Monoclinic-Bismuth vanadate
a-TO	Anatase Titanium dioxide
δ	Dislocation density
SEM	Scanning electron microscope
TEM	Transmission electron microscope
DRS	Diffuse reflectance spectroscopy
AFM	Atomic force microscopy
XRD	Xray diffraction
BET	Brunauer-Emmet-Teller
EIS	Electron impedance spectroscopy
fb	Flat band
E_{fb}	Flat band potential
LE	Level
PA	Prepared Arsenic
$[As]_0$	Initial concentration of Arsenic
BK7	Boroflat glass
I_{int}	Integrated intensity
η_{BVO}	Fraction of Bismuth vanadate
η_{TO}	Fraction of Titanium dioxide

CONTENT

	Page number
1. Introduction	
1.1 General context	1
1.2 Advanced Oxidation Process	4
1.2.1 Photocatalysis and mechanism	5
1.2.2 Photocatalytic reaction	6
1.2.3 Semiconductor photocatalysis and photocatalysts	7
1.2.4 Role of surface on the photocatalytic process	9
1.2.5 Effect of pH and concentration	9
1.3 Electronic band engineering for efficient photocatalysts	9
1.4 State of art: Materials and performance	10
1.4.1 Titanium dioxide- properties	10
1.4.2 Bismuth Vanadate- properties	11
1.4.3 Titanium dioxide/Bismuth vanadate structures	13
1.5 Objectives of the Study	15
References	17
2. Experimental methodology and instrumentation	22
2.1 Sol- gel synthesis	22
2.1.1 Main steps for sol-gel synthesis process	22
2.1.2 Synthesis of $BiVO_4$	23
2.1.3 Synthesis of TiO_2/ $BiVO_4$ composites	23
2.2 Deposition of films by rf -sputtering	25
2.2.1 Working principle	25
2.2.2 RF-sputtering of TiO_2/ $BiVO_4$ films	26
2.3 Characterization Techniques	27
2.3.1 X- Ray diffraction analysis	27
2.3.2 Raman analysis	29
2.3.3 UV-Visible spectroscopy	31
2.3.4 Scanning electron microscopy	33
2.3.5 Transmission electron microscopy	33
2.3.6 Atomic force microscopy	35

2.3.7 Profilometry- thickness measurement 37
2.3.8 Brunauer-Emmet-Teller (BET) surface area measurement 37
2.3.9 Photoelectrochemical characterizations 39
2.4 Photocatalytic dye degradation- Quantification methodology 39
2.4.1 Kinetics of photocatalytic reactions 41
2.4.2 Photocatalytic arsenic removal- quantification methodology 42
References 44

3. Sol- gel synthesis and characterizations of TiO_2/ $BiVO_4$ nanocomposite 45
3.1 Optimization of synthesis method for TO/BVO nanocomposites 45
3.2 X-Ray diffraction analysis 46
3.3 Raman analysis 49
3.4 Scanning Electron Microscope (SEM) analysis 50
3.5 UV- Vis bandgap analysis 53
3.6 Transmission Electron Microscope (TEM) Analysis 55
3.7 Photocatalytic degradation tests using ACID BLUE 113 as model 58
3.8 Electrochemical properties of TiO_2/ $BiVO_4$ material 62
References 68

4. PC Oxidation of As(III) and optimization using CCD and RSM 72
4.1 Analysis of Variance (ANOVA) for the optimization of the processing parameters; Experimental design based on statistical analysis 72
4.1.1 The steps involved in the process 73
4.2 Characterizations 80
4.2.1 X-ray diffraction analysis 81
4.2.2 Raman analysis 82
4.2.3 UV- Vis band gap analysis 82
4.2.4 Scanning Electron Microscope (SEM) analysis 83
4.2.5 Brunauer Emmet Teller (BET)- Surface area analysis 84
4.3 Photocatalytic degradation tests 85
References 91

5. Deposition, characterization and PC application of RF-sputter deposited TO/BVO films 95

5.1 Optimization of the parameters 95

5.1.1 Effects of the chamber atmosphere and substrate temperature 97

5.1.2 Effect of RF- power 98

5.1.3 Post annealing temperature- insitu analysis 99

5.2 X-ray diffraction analysis; Substrate effects on the deposited films 100

5.3 Raman analysis 105

5.4 UV- Vis band gap analysis 107

5.5 Transmission Electron Microscope **(**TEM) Analysis 108

5.6 Profilometry- thickness measurement 112

5.7 Atomic force micrograph analysis 113

5.8 Photocatalytic degradation tests 114

References 119

6. Conclusion 123

Abstract

This thesis presents the development of photoactive heterostructures of Bismuth vanadate ($BiVO_4$) and Titanium dioxide (TiO_2) and their application in photocatalysis under visible light irradiation, considering their abundance, non-toxicity, and high stability. The higher recombination rate in both materials, and the large band gap of TiO_2 (3.2eV) limit their applications. Hence, band gap engineered TiO_2/$BiVO_4$ nanocomposites were synthesized by a modified Sol-gel method in the powder form with the stoichiometry TiO_2 (**x**): $BiVO_4$(**1-x**) (x = 0.2, 0.5, 0.8) and another set with the low stoichiometry of $BiVO_4$, TiO_2 (**x**): $BiVO_4$(**100-x**) (x = 99.5, 99, 98.5, 98, 97.5%) was also synthesized considering the photocatalytic response from different contaminants. Considering their application in water treatment the powder was deposited as films using Radio-frequency sputtering. Films of two different architectures were developed: the first one is the composition of x=0.5 from sol- gel synthesized structures was chosen to make the target. And in the other, a layered heterostructure film with TiO_2 layer over $BiVO_4$ was deposited varying deposition time, power, chamber atmosphere and substrates. The optical, morphological, and electrochemical characterizations were performed. The UV-Visible characterizations confirmed the redshift in band gap depending on the stoichiometry of $BiVO_4$ (≈2.4eV) and TiO_2 (≈3.2eV). The X-ray diffractograms confirmed the formation of desired crystalline Monoclinic-$BiVO_4$ (101, 103) and Anatase TiO_2 (101) phases. The heterostructure formation was identified from TEM micrographs which clearly show the presence of junctions between phases. The electrochemical impedance spectroscopy corroborated the presence of surface states at the interface between the heterostructures causing higher charge separation efficiency within the structures which influenced the photocatalytic efficiency of the materials. A complete degradation of the organic dyes such as acid blue and methylene blue was observed using the powder structures within 20 minutes of irradiation. Arsenic(As) (III) oxidation and removal was performed using Central Composite Design (CCD) by Response Surface Method (RSM) and a complete removal of As was observed within an hour of irradiation. The deposited films demonstrated near and above 90 % of organic dye degradation within 180 minutes of irradiation, among which the layered architecture was more efficient. The re-usability test results confirmed the stability of the films without much reduction in their performance.

Key words: **Photocatalysis, Heterostructures, TiO_2/$BiVO_4$, Sol-gel, rf-sputtering, Band gap, dye degradation, Water treatment**

Resumen

Esta tesis presenta el desarrollo de heteroestructuras fotoactivas de vanadato de bismuto ($BiVO_4$) y dióxido de titanio (TiO_2) para su aplicación en el tratamiento fotocatalítico de agua con luz visible al considerando su abundancia, no toxicidad y alta estabilidad. Por separado ambas estructuras están limitadas para ciertas aplicaciones ya que presentan altas tasas de recombinación de portadores fotogenerados, además la energía de banda prohibida del TiO_2 (3.2eV) se encuentra en el intervalo de luz ultravioleta. Considerando la respuesta fotocatalítica de diferentes contaminantes, se diseñaron dos series de heteroestructuras a base de $TiO_2/BiVO_4$ y fueron sintetizadas mediante un método de sol-gel modificado. La primera serie posee una estequiometría de TiO_2 (**x**): $BiVO_4$(**1-x**) (x = 0.2, 0.8, 0.5), mientras que la segunda corresponde a baja estequiometría de $BiVO_4$ (TiO_2 (**x**): $BiVO_4$(**100-x**) (x = 99.5, 99, 98.5, 98, 97.5%). Considerando su aplicación en el tratamiento del agua, las heteroestructuras en polvo fueron inmovilizadas en forma de películas delgadas mediante la técnica de pulverización catódica por radiofrecuencia. Se desarrollaron películas de dos arquitecturas diferentes: la primera utilizando la composición optimizada de la heteroestructura (X = 0.5) y la segunda corresponde a una capa de TiO_2 sobre una capa de $BiVO_4$ variando el tiempo de deposición, la potencia, la atmósfera de la cámara y los sustratos. Se realizaron las caracterizaciones ópticas, morfológicas y electroquímicas. Los espectros de absorción UV-Visible confirmaron el corrimiento al rojo en la banda prohibida en función de la estequiometría de $BiVO_4$ (≈2.4eV) y TiO_2 (≈3.2eV). Los difractogramas de rayos X confirmaron la formación de las fases cristalinas $BiVO_4$-Monoclínica (101, 103) y TiO_2 Anatasa (101). La formación de la heteroestructura se identificó a partir de microscopía electrónica de transmisión (TEM), observando claramente planos de unión entre ambas fases. La espectroscopia de impedancia electroquímica corroboró la presencia de estados de superficie en la interfaz de la heteroestructura que provocan una mayor eficiencia de separación de carga dentro de las mismas. Estas características influyeron en la eficiencia fotocatalítica de los materiales. Se observó una degradación completa de los colorantes orgánicos como el azul ácido y el azul de metileno usando las heteroestructuras en polvo dentro de los 20 minutos de la irradiación. Así mismo, se realizaron ensayos de oxidación y eliminación de arsénico (III) utilizando un diseño compuesto central (CCD) por el método de superficie de respuesta (RSM) y se observó una eliminación completa de arsénico dentro de una hora de irradiación. Por su parte, las películas depositadas demostraron una degradación de colorante orgánico cerca y por encima del 90% dentro de los 180 minutos de

la irradiación, entre las cuales la arquitectura en capas resultó ser más eficiente. Los resultados de la prueba de reutilización confirmaron la estabilidad de las películas sin gran reducción en su rendimiento.

Palabras clave: Fotocatálisis, Heteroestructuras, $TiO_2/BiVO_4$, Sol-gel, pulverización catódica por radiofrecuencia, energía de banda prohibida, degradación de colorantes, Tratamiento de agua

Résumé

Cette thèse présente le développement d'hétérostructures photo activés de vanadate de bismuth ($BiVO_4$) et de dioxyde de titane (TiO_2) pour leur application en photocatalyse sous irradiation de la lumière visible, compte tenu de leur abondance, de leur non-toxicité et de leur grande stabilité. De point de vue application, les deux structures sont limitées leurs taux de recombinaison élevés et la large bande interdite du TiO_2 (3,2 eV) qui absorbe uniquement la lumière ultraviolette. Compte tenu de la réponse photo catalytique de différents polluants, deux séries d'hétérostructures à base de TiO_2 / $BiVO_4$ ont été conçues et synthétisées en utilisant la méthode sol-gel modifiée. La première série est élaborée pour des fortes stœchiométries de TiO_2 (**x**): $BiVO_4$(**1-x**) (x = 0.2, 0.8, 0.5), mientras que la segunda corresponde a baja estequiometría de $BiVO_4$ (TiO_2 (**x**): $BiVO_4$(**100-x**) (x = 99.5, 99, 98.5, 98, 97.5%).. En raison de leur application dans le traitement des eaux, les poudres préparées ont été déposées sous forme de couches minces en utilisant la technique de la pulvérisation cathodique en mode radiofréquence. Deux films d'architectures différentes ont été développés : le premier utilisant la composition optimisée de l'hétérostructure (X = 0,5) et le second correspond à une couche de TiO_2 sur une couche de $BiVO_4$ en faisant varier le temps de dépôt, la puissance, l'atmosphère de la chambre et les substrats. Des caractérisations optiques, morphologiques et électrochimiques ont été réalisées. Les spectres d'absorption UV-Visible ont confirmé le décalage vers le rouge dans la bande interdite en fonction de la stœchiométrie de $BiVO_4$ (≈2,4eV) et TiO_2 (≈3,2eV). Les diagrammes aux rayons X ont montré la formation des phases cristallines Monoclinique du $BiVO_4$ (101, 103) et d'Anatase du TiO_2 (101). La formation des hétérostructures a été identifiée par microscopie électronique à transmission (MET), qui montre clairement la présence des jonctions entre les plans. La spectroscopie d'impédance électrochimique a corroboré la présence d'états de surface à l'interface entre les hétérostructures, entraînant une plus grande efficacité de séparation des charges dans les structures, ce qui a influencé l'efficacité photo catalytique des matériaux. Une dégradation complète des colorants organiques tels que le bleu acide et le bleu de méthylène ont été observés en utilisant les hétérostructures en poudre après 20 minute l'irradiation. De même, des analyses d'oxydation et d'élimination de l'arsenic (III) ont été effectuées en utilisant une conception composite centrale (CCD) par la méthode de surface de réponse (RSM) et une élimination complète de l'arsenic a été observée après une heure d'irradiation. D'autre part, les films déposés ont démontré une dégradation des colorants organiques proche et supérieure à 90 % après 180 minute l'irradiation, parmi

lesquelles l'architecture en couches s'est avérée plus efficace. Les résultats des tests de réutilisation ont confirmé la stabilité des films avec une légère réduction de leurs performances.

Mots clés: Photocatalyse, Hétérostructures, TiO_2 / $BiVO_4$, Sol-gel, pulvérisation radiofréquence, énergie de bande interdite, dégradation des colorants, Traitement de l'eau

CHAPTER. 1

Introduction

1.1 General context

Environmental remediation, aimed at a sustainable and clean world, is one of the vital societal challenges. According to the World Health Organization (WHO) reports, over 785 million people lack essential drinking water. It also reports that half of the world population will be living in water-stressed areas by 2025, adding water crisis to the prominent list of global crises (fig. 1.1). Water pollution has an enormous contribution to this crisis, with heavy metals originating predominantly from agriculture (e.g., pesticides) and industrial (e.g., dyes, mines) effluents playing significant roles. The heavy metals (e.g., Pb, Cr, Cd, Zn, Fe, Mn, As, Hg) refer to the metallic elements with high toxicity, density, and atomic weight. These contaminants leach in to the groundwater, even from natural sources (e.g., rocks), and into the food chain through the intake of contaminated water, plants, and animals. These heavy metals present different toxicity levels and adverse health effects, including low oxygen content levels in the water, causing a higher Biological Oxygen demand (BOD) and algal blooms [1].

Many industrialized countries, including Mexico, are plagued by these heavy metals in their natural groundwater sources, e.g., arsenic. The arsenic (As) crystalline "metalloid" is one of the heavy metals, ranking among the most occurring element in the earth's crust, existing in various oxidation states (− III, 0, + III, + V), with the arsenite (III) and arsenate (V) states primarily present in an aqueous medium [2]. The inorganic forms commonly leach from several sources into water bodies, e.g., industrial wastes, biological activity, soils, mining activities, and fertilizers, containing minerals and occurring naturally [1]. Arsenic is highly carcinogenic, causing cancer in various human body organs, including lung, bladder, liver, renal, and skin cancer [2]. More so, the long-term exposure or intake of As-contaminated food or water causes serious diseases, e.g., respiratory poisoning, disturbance in nervous systems, cardiovascular diseases, conjunctivitis, hyperpigmentation. Consequently, there is a significant necessity for removing As from drinking water and edible materials [2], especially the inorganic forms considered to be the more harmful.

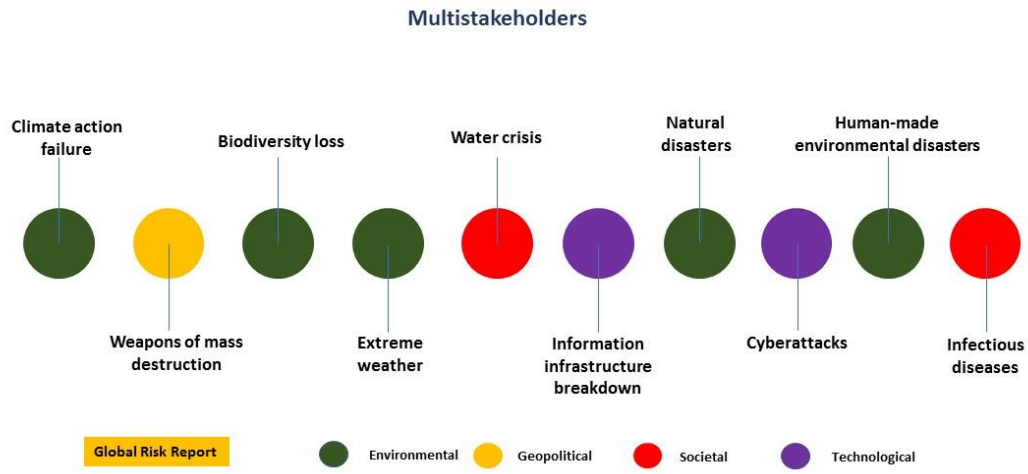

Fig. 1.1 Top 10 global risks in the next ten years; Global risk reports World economic forum 2020

The inorganic As removal employs various methods, including reverse osmosis, adsorption, chemical treatment, membrane filtration, ion exchange, electrochemical treatment, and co-precipitation [3,4]. Comparatively, As(III) presents a lower affinity to the mineral surfaces and possesses more migratory species, whereas As(V) gets readily adsorbed onto solid surfaces and its removal mechanism from aqueous samples being easier compared to As(III) [2]. Hence, a pre-oxidation process followed by adsorption must favor complete removal of the As(III). The adsorption methods provide easy complexation processes based on the formation of negatively-charged ions ($H_2AsO_4^{1-}$, $HAsO_4^{2-}$). The more challenging to remove As(lll) (H_3AsO_3, $H_2AsO_3^{-1}$) get oxidized and subsequently removed as As(V). In the aqueous media, the presence and potential removal of the As(lll) and As(V) in defined compounds depends upon the water's redox potential and pH [2].

Another primary source of contaminants in industrial effluents is the dye, contributing 17 to 20% of water pollution and decomposes into hazardous by-products. These water bodies' dyes cause decreased sunlight penetration and reduced photosynthetic activities in aquatic ecosystems, resulting in increased BOD [5]. Some classification of dyes includes dispersive dyes (polyester, nylon, and acetate) [6], reactive dyes (*Safira dye*, *HEXL*) [7], sulfur dyes, and vat dyes (viscous) [8]. Azo dyes refer to a class of synthetic dyes, widely used to treat textiles, leather articles, and some foods, with over 50% global annual production. They contain one or more -N=N- groups in their chemical structure and consist of highly substituted aromatic rings [9]. They have a high potential for toxicity and are carcinogenic; many of the azo dyes reduce into highly hazardous aromatic compounds, causing

eutrophication, resulting in insufficient oxidation and high-water concentrations [5]. Although some dyes can degrade naturally, azo dyes' chemical structure leads to recalcitrant characteristics, i.e., they degrade slowly under natural conditions and are also resistant to conventional wastewater treatment processes [6]. Many studies have explored various methods to treat dye-contaminated waters, including adsorption, precipitation, biological methods such as aerobic and anaerobic treatments, oxidation and reduction, reverse osmosis [3,4].

The photocatalytic process offers a green and low-cost methodology to address these environmental concerns for removing heavy metals and dyes in water bodies. The catalysts are reusable, eco-friendly and the by-products are mostly harmless to the environment and the living cells. Many photocatalytic processes utilize the advanced oxidation process (AOP) for a convenient and efficient contaminant degradation methodology [6,10]. Some AOP examples include Fenton processes, ozone treatment, photocatalysis (UV/Visible), and ultrasonic treatments [11].

Photocatalysis's characteristic photoactive materials play vital roles in the efficient generation/separation of photo-generated charges. Several scientific and technological approaches explored, including doping, metal loading, formation of the heterojunctions/heterostructures between photoactive compounds, aim to improve these materials' functions [12]. The photoactive oxides, among other potential options, present relevant compositions and enticing properties for photocatalytic applications, having bandgaps and energy levels (valence band (VB) and conduction band (CB) comparable to water's redox potential (fig. 1.2) [13]. Their desirable properties also include relative abundance, chemical stability, and corrosion resistance.

Titanium dioxide (TO), commonly used for photocatalytic activities, possesses the enticing properties of photoactive oxides, and it is also a low-cost material. It has a wide bandgap, ~ 3.2eV, and widely accepted due to its photocatalytic efficiency. However, it activates under the electromagnetic (EM) spectrum's ultraviolet region, which is approximately 3 to 5 percent of the whole solar spectrum. This narrow region of the EM severely limits its application, necessitating some form of bandgap engineering to make it efficient and a light-active photocatalyst within the visible EM region too [14]. Another limitation posing a significant drawback is the surface area, which decreases due to agglomeration.

Bandgap engineering refers to the process of controlling or altering the bandgap of a material, typically semiconductors, by controlling the alloys' composition or creating layered materials with alternating compositions [15,16]. Some bandgap engineering methods include doping, metal loading, surface functionalization or grafting sensitizing groups [17], heterojunctions' formation [18]. Several mechanisms for fabricating heterojunction/heterostructure film structures include spin coating, spray pyrolysis, drop-casting, electrodeposition [19], and sputter deposition [20].

Tuning the bandgap and forming composites with other metals or metal oxides to reduce agglomeration challenges in the TO materials [21] has continued to attract considerable attention from researchers [22]. Some metals and metal oxides employed for this purpose include $BiVO_4$, Fe_2O_3, WO_3, considering the low-cost, high adsorption capacity, and affinity [22-24]

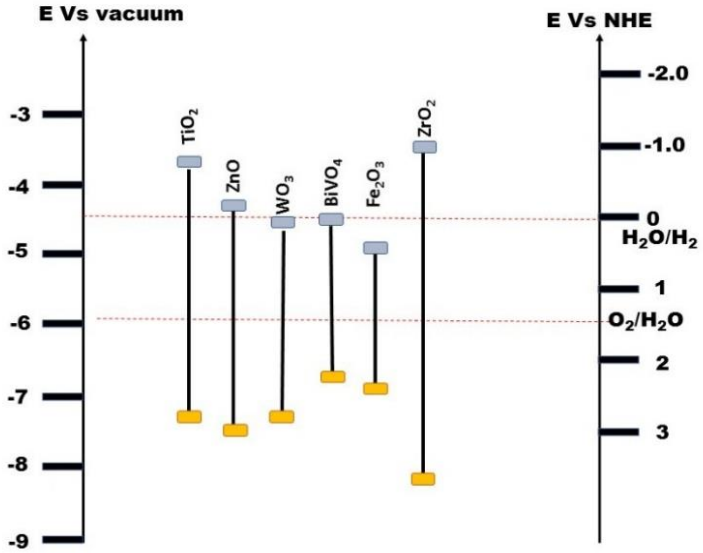

Fig. 1.2 Different oxide photocatalysts with bandgap and energy levels of VB and CB compared to water's redox potential

1.2 Advanced Oxidation Process

The advanced oxidation process (AOP) identifies a group of techniques that use favorable reactive oxidative species [25] to oxidize and mineralize a wide range of chemical compounds and biological contaminants [26]. The processes include wet air oxidation, ozone treatment, Fenton/photo-Fenton processes, ultra-violet or visible light photocatalysis, ultrasonic treatment, and other available methodologies to remove many toxic non-

biodegradable pollutants [11]. This study adopts photocatalysis due to its simplicity and cost-effectiveness. It does not produce any harmful by-products, targeting only the pollutants, and can simultaneously degrade a broad spectrum of other micropollutants present in the water.

1.2.1 Photocatalysis and mechanisms

A catalyst is a substance that accelerates a chemical reaction rate without being consumed during the reaction [27]. In photocatalysis, the photo-generated electrons get accelerated in the presence of a catalyst [28]. The International Union of Pure and Applied Chemistry (IUPAC) describes photocatalysis as changes in chemical reaction rates or initiation under UV, visible, or infra-red (IR) irradiation in the presence of photocatalyst absorbing light and involved in reaction partners' chemical transformation [29]. The light excites the photocatalyst and the reaction rate without consuming the photocatalyst [30]. Photocatalysis has a wide variety of applications from environmental remediation up to the medical field and processes leading to the degradation of different pollutants such as phenols, alkanes, alkenes, aromatics, pesticides, organic contaminants [30], heavy metals [1].

The photocatalytic process using semiconducting (SC) materials involves different stages as in the fig.1.3. Photons with energies higher or equal to the bandgap energy (E_g) of a given SC photocatalyst get absorbed, creating electron-hole (e-, h+) pairs. The ***electron*** (e^-) migrates to the VB, leaving behind a complementary ***hole*** (h^+) in the CB. The created e^- and h^+ catalyze the redox reactions on the photocatalysts' surface, leading to the contaminants' degradation.

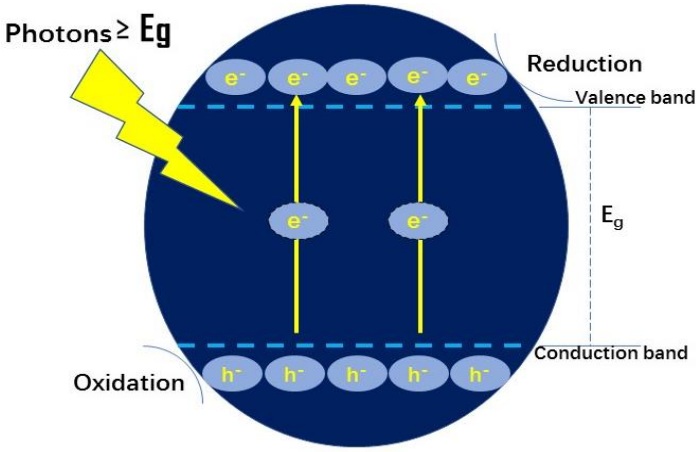

Fig. 1.3 Photons induced formation of electron-hole pairs in an SC material followed by the migration of charges to the SC surface where redox reactions occur

The positive holes may interact with electron donor species or OH^- radicals to form hydroxyl radicals (OH^*), which belong to the oxidizing radicals, while the electrons react with the oxygen to form superoxide radicals (O_2^-), potentially create several reactive oxidation species ($OH^\cdot$, O_2^-, H_2O_2, O_2). However, the main limitation to the process occurs when the photo-induced charge carriers recombine without participating in the reactions, i.e., when their lifetimes remain negligible. Several approaches, e.g., doping, heterostructure/heterojunction formation, can be performed to enhance photo-generated charge carriers' lifetime and overcome this limitation [18,19].

1.2.2 Photocatalytic reactions

The redox reactions supported by an SC photocatalyst follow reactions dedicated to the degradation of pollutants in water. They include,

$Photocatalyst + photons\ (h\nu) = e^- + h^+$ ***eqn. (1.1)***

$O_2 + e^- = O_2^-$ ***eqn. (1.2)***

$H_2O + h^+ = OH^\cdot + H^+$ ***eqn. (1.3)***

$O_2^- + H^+ = HO_2^\cdot + OH^\cdot$ ***eqn. (1.4)***

$Pollutant + e^- = products\ (reduction)$ ***eqn. (1.5)***

$OH^- + h^+ = OH^\cdot$ ***eqn. (1.6)***

$Pollutant + h^+ = products\ (oxidation)$ ***eqn. (1.7)***

Several factors influencing the efficiency of the photocatalytic process include,

- pH
- The initial concentration of the contaminant
- Intensity of radiation
- Dosage of the catalyst

Photocatalytic reactions may occur either as (i) homogeneous or (ii) heterogeneous reactions, depending on the media used for the reactions. Homogeneous photocatalysis occurs when the catalyst and reactant are in the same phase, e.g., Ozone and photo-Fenton systems, whereas heterogeneous catalysis involves different phases.

The effect of the factors mentioned above on the photocatalytic reaction is very significant. For instance, the solution pH affects the adsorption and dissociation of the contaminant molecule over the catalyst surface. When the pH is above the isoelectric point of the photocatalyst, its surface becomes negatively charged. Reducing the pH may cause the functional groups to become protonated, causing the photocatalyst surface to become more positively charged. Consequently, it may adsorb more anionic molecules and vice versa.

The contaminant's initial concentration greatly determines the optimal catalyst dosage chosen. Below specific values, there will not be enough active sites for the reaction; an enormous catalyst dosage, on the contrary, may cause the reaction media's opacity, hence blocking the irradiation into the solution or leading to a light scattering loss. In essence, the non-optimized catalyst dosage may cause a reduction in the performance of the system. The intensity of the incident radiation is another critical factor providing energy for the charge separation, thus requires optimization. Heterogeneous photocatalysis, explained in the later section, will provide an example of the pc reaction by a semiconducting photocatalyst and semiconductors or transitional metal oxides used for most reactions [30]. Heterogeneous reactions include charge transfer processes and redox reactions.

1.2.3 Semiconductor photocatalysis and photocatalysts

The early record of photo-electrochemistry and photocatalysis by Fujishima and Honda in 1972 reported using TO and platinum (Pt) for hydrogen production [31]. Subsequently, extensive deployment of semiconducting materials for different photocatalytic applications [31] depends on their electronic/transport characteristics, optical absorption properties, and electronic structure, which control the photo-activated charge carriers. Many of the semiconductor properties depend on the bandgap, which correlates with their structural properties.

Other physical conditions affect the bandgap of the materials, e.g., size, temperature. Thalluri et al. [32] reported a decrease in the bandgap of hydrothermally synthesized BVO from 2.49 to 2.39eV as the hydrothermal temperature increased from 350 to 700 °C. The sintering temperature affects the bandgap, changing the nanoparticles' electronic structure and the particles' crystalline feature. The bandgap's modification by quantum confinement effects may also benefit the nanoscale's semiconducting materials [32].

Several oxide semiconductor systems acting as catalysts find water remediation applications or water splitting for hydrogen evolution (fuel production). The bandgap, valence, and

conduction band edge energies relative to water's redox potential (fig. 1.4.a) play vital roles in the reactions, considering that the solution's pH significantly influences the photocatalytic process. In particular, for TO and BVO, though similar for other semiconducting materials, the pH (=12), for instance, modifies the semiconductors' band edges (fig. 1.4.b) and affects the solution's charge transfer.

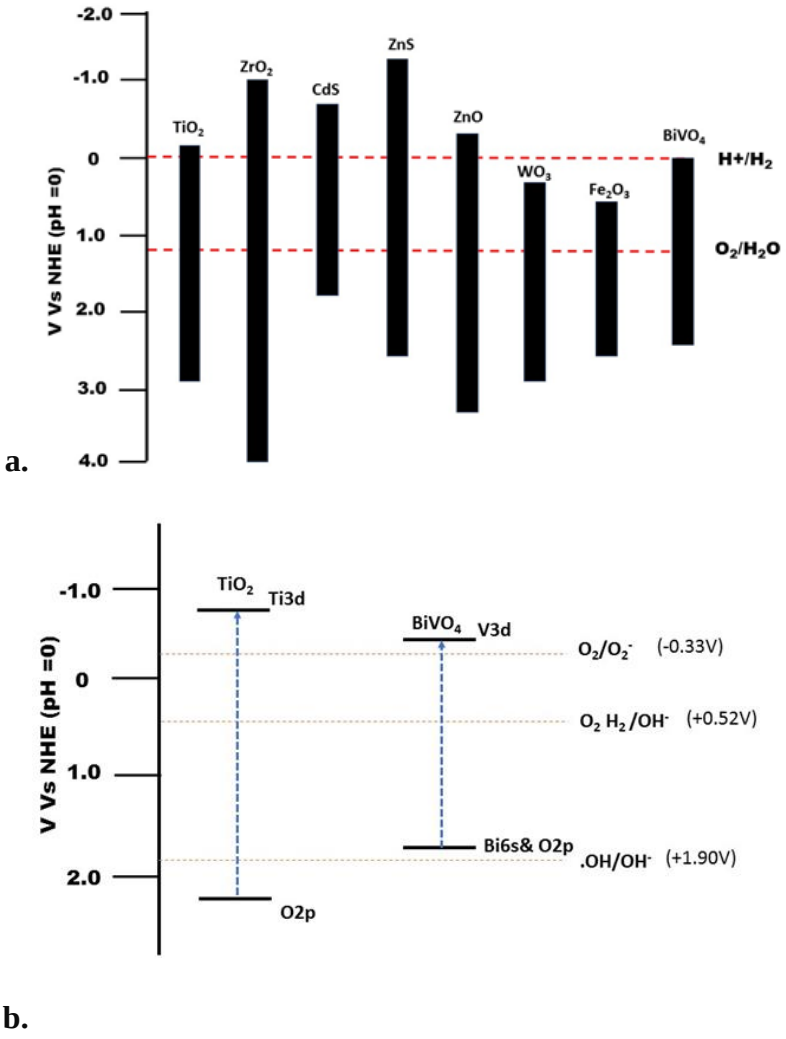

Fig. 1.4. (a) Band edge positions of different semiconductors (pH = 0) [33], **(b)** Band edge positions of TO and BVO at higher pH=12

For a visible light-activated process at pH = 0, the photocatalyst's conduction band must be more negative than the reduction potential of H^+/H_2 (0 vs. NHE (Normal hydrogen electrode)), and the valence band (VB) edge must be more positive than the oxidation potential of O_2/H_2O (1.23 vs. NHE). Thus, the VB edge's theoretical minimum for the process must be at 1.23 eV [33].

1.2.4 Role of the surface on the photocatalytic processes

The properties of the semiconducting material influence the catalytic performances. The redox reactions involved during the heterogeneous photocatalysis occur at the semiconductor's surface and high surface atoms ratio characterizing the nanostructured material compared to those involved in its core [34]. At the active sites of the surface involving electrons and holes, the photo-generated charge carriers react with the adsorbed molecules with reactive oxygen species as the main vectors for photocatalysis. The morphology and crystallinity at these surfaces depend on the synthesis method, the operating conditions, and the post-synthesis thermal treatment. Pardeshi et al. [35] reported that zinc oxide particles' efficiency in the photocatalytic process significantly depends on the morphology and crystallite size. The effect of temperature, e.g., during synthesis, can lead to the nanoparticles' agglomeration. After depositions, thermal treatments at high temperatures can cause morphology changes to a distinguished structure with a noticeable increase in particle size [35].

1.2.5 Effect of pH and concentration

The precursors' pH and concentration in chemical synthesis can influence the particles' morphology, size, and crystallinity. Sibiya et al. [36] showed that an increase in the pH could lead to reduced particle sizes, i.e., from pH of 6 to 7, with particle sizes about 5.76 and 7.96 nm, respectively, while at pH at 11, the size was as small as 1.92 nm. Mahdi et al. reported that an increase in the crystallinity with the precursor concentration for silver nanoparticles. [37]. The consequential effects of the pH and precursor concentrations greatly influence the nanoparticles' impact on the pc process's efficiency in the adsorption/desorption mechanism of the contaminants. When the pH increases above the isoelectric point, the photocatalyst surface becomes positively charged and adsorbs more cationic molecules. Conversely, the surface gets protonated when the pH is reduced and hence adsorbs more anionic molecules.

1.3 Electronic band engineering for efficient photocatalysts

Several efficient semiconductors investigated to address the water treatment by photocatalytic processes consider wide bandgap materials, e.g., TO and ZnO. However, a severe drawback to their efficiency lies in the energetic cost due to required UV excitation sources. Several strategies developed to deal with these materials' challenges involve engineering and tuning the bandgap to have some solar radiation's visible range activities. A common approach to tuning the semiconductors' bandgap involves doping by different metallic or non-metallic elements to modulate the electronic bandgap. Another alternative

solution exploit developing heterostructures using two semiconductors of worthy of interest. Improving the semiconductors' properties enhances the charge transfer groups (organic, metallic) within the material, the photo-generated charge carriers, the carrier lifetime, and an approach to boost the whole system's photo-response. The realization of the heterostructures requires the electronic band structure compatibility at the heterojunctions. The present work aims to develop TO/BVO heterostructures to enhance the composed system's photoactivity (fig. 1.5).

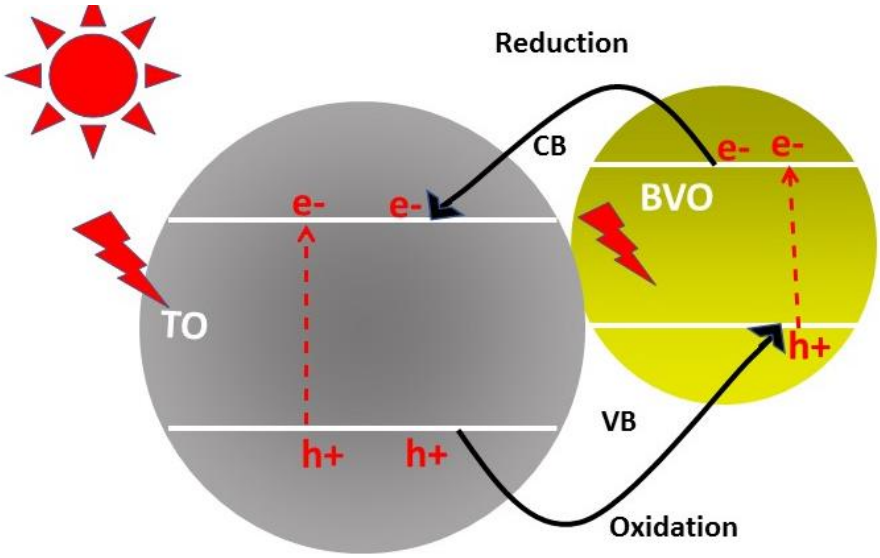

Fig. 1.5 Photocatalysis scheme for coupled semiconductors system

1.4 State of the art: materials and performance

1.4.1 Titanium Dioxide-Properties

The titanium dioxide semiconducting materials exist predominantly in three different forms; two different tetragonal forms and a rhombic phase, namely- rutile, anatase, and brookite. Rutile and anatase structures are structurally symmetrical, with each titanium atom surrounded by six oxygens, forming an octahedron TiO_6. The distortions and linkages in each form make the structures distinct from each other. Unlike the rutile and brookite phases, the anatase TiO_2 has an indirect bandgap, whereas the former phases are direct bandgap structures [38]. The positions of the band edges for VB and CB for the anatase phase relative to the potential redox for water splitting made it an excellent choice for photocatalysis performances.

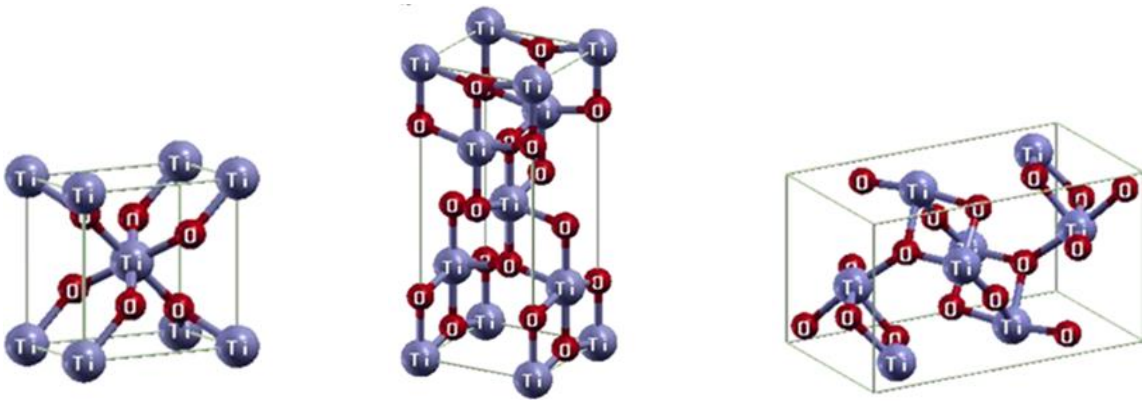

a. **b.** **c.**

Fig. 1.6 a) Rutile b) Anatase and c) Brookite phases of TO [38]

An essential allure of the TO is its property as an environment purifying catalyst. However, several factors, including its wide bandgap and spectral absorbance limited to the UV region, higher recombination, limit its applications. Different engineering approaches, e.g., structural and morphologies modifications, electronic band engineering, usually by introducing dopants or metal/semiconductor material loading, aim to improve the efficiency of TO, enhancing the properties such as surface area, chemical nature, porosity [39]. Modifying the TO materials' properties also helps improve the lifetimes of photo-generated charges, which are critical parameters in the photocatalysis process.

Lee et al. [40] identified that incorporating metals such as Pt, Pd, Ag, Au into TO can enhance the photo-response/pc efficiency by limiting the charge recombination inside the materials. The considered dopants exhibit lower Fermi levels, and photo-generated electrons from TO surface attain improved lifetimes, reducing recombination. Other potential materials include a semiconducting oxide, e.g., iron oxide, $BiVO_4$, V_2O_4.

1.4.2 Bismuth Vanadate-Properties

Bismuth-based materials have attracted excellent physicochemical properties and potentials for visible light photocatalysis considering their electronic structure, allowing high mobility and concentration of the photo-generated charge carriers. The electronic structure consists of Bi 6s (which can increase the charge carriers) and O 2p hybrid orbitals in the valence band [41], and a conduction band consisting of Bi 6p orbitals (fig.1.7) [42].

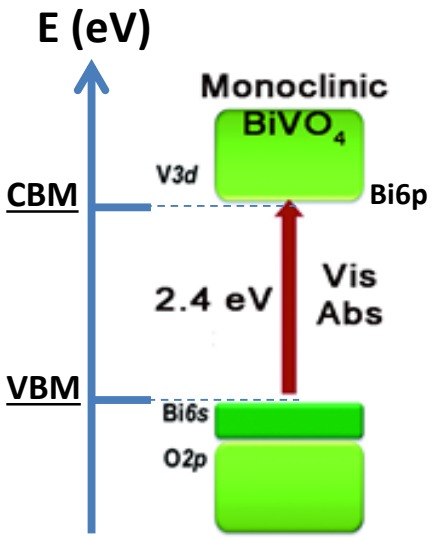

Fig. 1.7 Electronic energy diagram of the monoclinic phase of BVO showing the possibility of visible light absorption

BVO semiconductor has a bandgap of ~ 2.4 eV in its monoclinic scheelite polymorph and a ~ 3.1eV in the tetragonal phase [43]. It is non-toxic [44] and chemically stable in aqueous solutions, serving in heterogeneous photocatalysis using visible light-harvesting for redox reactions [43-46]. The crystalline structures of BVO may exist in tetragonal zirconia structure (z-t), tetragonal scheelite (s-t), or monoclinic BVO [45]. The zirconia type structure has a tetragonal crystal system with $I4_1/a$ where a= b= 7.303 Å; c=60584 Å. Scheelite type also has a tetragonal structure crystal system with a space group I 2/b, and a= b= 5.1470 Å; c= 11.7216 Å [47].

In the tetragonal-scheelite structure, four oxygen atoms in their tetrahedral sites coordinate every vanadium ion, and eight oxygen atoms from eight different units of VO_4 tetrahedron coordinating each bismuth ion. In the tetragonal scheelite structure, all the four V-O bonds have lengths equal to 1.72 Å and two similar values for the Bi-O bond length at 2.453 and 2.499 Å. The monoclinic scheelite structure has two different bond lengths of 1.77 and 1.79 Å for V-O bond lengths. For the Bi-O bonds, there exist four different values at 2.354, 2.372, 2.516, and 2.628 A° [43]. The monoclinic scheelite structure reportedly has higher photocatalytic activity, which may be due to several distortions in the metal polyhedral. These distortions further promote the charge carrier separations and favor the material's photocatalytic efficiency [48].

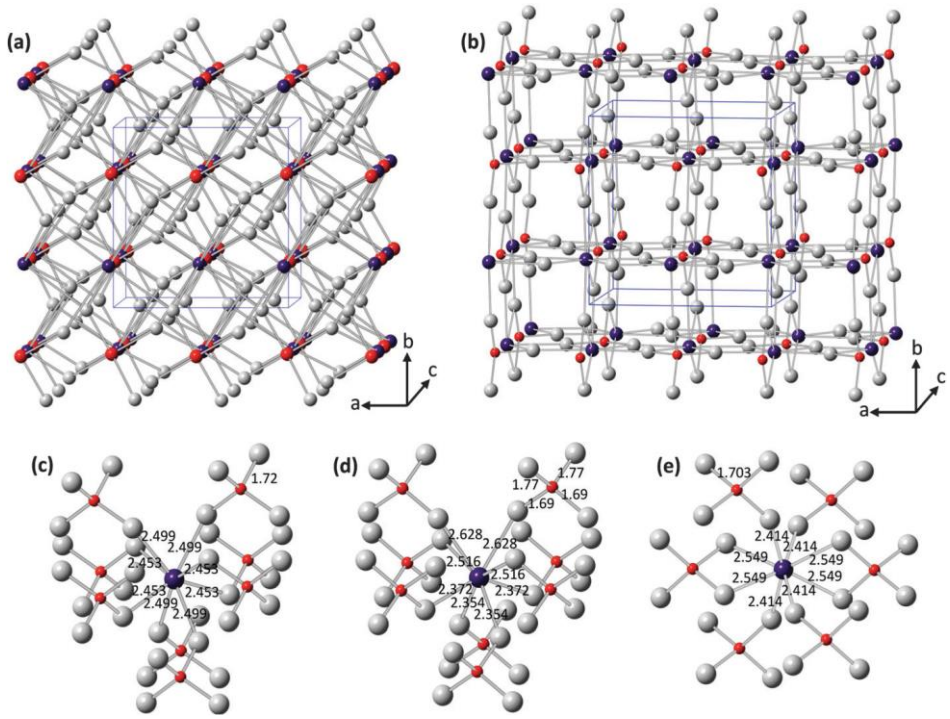

Fig. 1.8 (a)Tetragonal- scheelite structure b) Tetragonal- zircon structure [red; vanadium, purple; bismuth, grey; oxygen. The monoclinic- scheelite structure is similar to tetragonal scheelite as in (a) except for changes in atomic positions of Bi, V, and O atoms [47]

1.4.3 Titanium dioxide/ Bismuth vanadate structures

Several techniques reported in the literature for fabricating titanium dioxide/bismuth vanadate structures aim to tap into the combined structures' advantages. Cao et al. [49] reported the synthesis of peanut-shaped TO/BVO nanostructures by a hydrothermal method [49]. When used pristine, the pc activity of BVO was so low due to rapid recombination of the charge carriers. However, BVO plays the role of the visible light absorber in the composite structure. The composite structure exhibited good charge transfer properties due to the formation of the inter-band states; hence, it exhibited sound degradation of the rhodamine-G dye under the usage of the scavenger H_2O_2, with good reusability of the material. Yin Hu et al. [50] studied the effect of BVO loading in the TO/BVO nanocomposite with different weight percentages (0.5,2,9,30,50 and 80%). A high amount of BVO appears to block the active sites and cause faster recombination of the charge carriers.

The TO/BVO composites/heterostructure films occur in several configurations for pc applications. The type-1 configuration has the heterojunctions has a layer of TO film over BVO as a layered structure. Commonly used techniques to fabricating this configuration include radio-frequency (RF) deposition. The type-2 heterostructure commonly employs a

hydrogen-treated TO for its growth. It has a reported increase in photo-generated charge carriers' lifetime and has a visible light response, as confirmed by the photocurrent response characterizations [51]. The lattice distortion caused by hydrogen introduction in TO leads to a discontinuity in the band structure and further reduced the charge carriers' recombination rate [51]. A three-layered BVO-TO-BVO film prepared using a sol-gel method with the formation of layered heterojunctions reportedly had improved efficiency of the system compared to the other configurations [52]. Hongxing et al. [53] developed a TO/BVO/Ti film system using an electrodeposition process for efficient pc water splitting. Other studies reported the development of TO/BVO photoanodes for the same pc water splitting application [54,55].

TO and BVO compounds' combined properties offer great potentials as a photocatalyst, addressing the large bandgap of TO that limits the efficiency to approximately nearly 4% of the solar spectrum along with its low quantum efficiency [56]. A significant drawback for the BVO material is the fast recombination rate in BVO because the conduction band CBM is not high enough for H_2 production during the water-splitting reactions [57]. Hence, combined can compensate for the disadvantage and increase the efficiency compared to the individual structures. Hence, in this work, we aim to develop a composite material with an engineered electronic band structure and bandgap.

1.5 Objectives

This study aims to synthesize TO/BVO nanocomposite powders with different compositions using a novel modified one-step sol-gel method and subsequently depositing a layered TO/BVO films heterostructures using RF-sputtering. The characterizations of the synthesized and sputtered films, for the structural, morphological, topographical, and optoelectronic properties will allow the optimization for photocatalytic applications.

The thesis's general objective will include synthesizing nanocomposites and heterostructures of TO/BVO for photocatalytic application in dye degradation and water remediation problems.

Specifically, the objectives include;

- To design TO/BVO nanocomposite heterostructures which offer the possibility of obtaining band-gap engineered materials with efficient visible-light photoactivity
- To obtain the crystalline nanocomposite photocatalysts materials with desired anatase TO and monoclinic BVO phases and to form the heterostructure TO/BVO with optimum band edge positions to reduce the barrier gap and hence to promote the charge separation efficiency
- To obtain the photocatalysts with higher surface area to have sufficient active sites available for the pc reactions
- To study the effect of the structural, optical, electrochemical properties on the pc water treatment

This thesis is organized into six chapters, with the general introduction as the first chapter and will contain,

Chapter 2 A detailed description of the synthesis and sputtering methods for the TO/BVO nanostructures;

- Sol-gel synthesized nanocomposite powders
- RF- sputtering deposition of the films

Characterization (i.e., structural, morphological, optical, and electrochemical) of the synthesized and deposited nanomaterials and instrumentation details.

The photocatalytic experimental set up and the quantification methods for analyzing the pc degradation experiments' final response

Chapter 3 Characterization and analysis of the results of pc application of the sol-gel synthesized nanocomposites with three different stoichiometries and comparing the efficiency in the pc degradation for organic azo dye- acid blue 113 (AB113)

Chapter 4 Characterization of a different set of sol-gel synthesized nanocomposite materials and analysis of variance (ANOVA) procedure for optimizing pc oxidation process parameters of arsenite using a response surface methodology (RSM) and central composite design (CCD)

Chapter 5 Optimization of the RF-sputtering parameters for the deposition of films of TO/BVO of two different architectures

- Nanocomposite film
- Layered heterostructure film with a TO layer over a BVO layer on various substrates

Characterizations and pc tests

Chapter 6 Conclusions

References

[1] S. V. Vargas-Solano, F. Rodríguez-González, M. L. Arenas-Ocampo, R. Martínez-Velarde, S. B. Sujitha, and M. P. Jonathan, "Heavy metals in the volcanic and peri-urban terrain watershed of the River Yautepec, Mexico," *Environ. Monit. Assess.*, vol. 191, no. 3, p. 187, Mar. 2019.

[2] P. K. Dutta, S. O. Pehkonen, and A. K. Ray, "Photocatalytic Oxidation of Arsenic (III): Evidence of Hydroxyl Radicals," vol. 39, no. 6, pp. 1827–1834, 2005.

[3] P. V. A. Padmanabhan *et al.*, "Nano-crystalline titanium dioxide formed by reactive plasma synthesis," *Vacuum*, vol. 80, no. 11–12, pp. 1252–1255, Sep. 2006.

[4] U. I. Gaya and A. H. Abdullah, "Heterogeneous photocatalytic degradation of organic contaminants over titanium dioxide: A review of fundamentals, progress and problems," *J. Photochem. Photobiol. C Photochem. Rev.*, vol. 9, no. 1, pp. 1–12, Mar. 2008.

[5] A. Ajmal, I. Majeed, R. N. Malik, H. Idriss, and M. A. Nadeem, "Principles and mechanisms of photocatalytic dye degradation on TiO_2 based photocatalysts: A comparative overview," *RSC Adv.*, vol. 4, no. 70, pp. 37003–37026, 2014.

[6] J. Koh, *Textile Dyeing*, no. Ici. InTech, 2011.

[7] S. D. Ovhal and P. Thakur, "Kinetics of photocatalytic degradation of methylene Blue in a TiO_2 slurry reactor," *Res. J. Chem. Environ.*, vol. 14, no. 4, pp. 9–13, 2010.

[8] R. Kant, "Textile dyeing industry an environmental hazard," vol. 4, no. 1, pp. 22–26, 2012.

[9] A. Gürses, "Sustainable colorants," in *The Impact and Prospects of Green Chemistry for Textile Technology*, Elsevier, 2019, pp. 21–55.

[10] S. Talebi, N. Chaibakhsh, and Z. Moradi-Shoeili, "Application of nanoscale ZnS/TiO_2 composite for optimized photocatalytic decolorization of a textile dye," *J. Appl. Res. Technol.*, vol. 15, no. 4, pp. 378–385, 2017.

[11] M. Antonopoulou, E. Evgenidou, D. Lambropoulou, and I. Konstantinou, "A review on advanced oxidation processes for the removal of taste and odor compounds from aqueous media," *Water Res.*, vol. 53, pp. 215–234, 2014.

[12] G. Crini, "Non-conventional low-cost adsorbents for dye removal: A review," *Bioresour. Technol.*, vol. 97, no. 9, pp. 1061–1085, 2006.

[13] Q. Lu, Y. Yu, Q. Ma, B. Chen, and H. Zhang, "2D Transition-Metal-Dichalcogenide-Nanosheet-Based Composites for Photocatalytic and Electrocatalytic Hydrogen Evolution Reactions," *Adv. Mater.*, vol. 28, no. 10, pp. 1917–1933, Mar. 2016.

[14] L. Wei, C. Yu, Q. Zhang, H. Liu, and Y. Wang, "TiO 2 -based heterojunction photocatalysts for photocatalytic reduction of CO 2 into solar fuels," *J. Mater. Chem. A*, vol. 6, no. 45, pp. 22411–22436, 2018.

[15] C.-Z. Ning, L. Dou, and P. Yang, "Bandgap engineering in semiconductor alloy

nanomaterials with widely tunable compositions," *Nat. Rev. Mater.*, vol. 2, no. 12, p. 17070, 2017.

[16] R. Shao *et al.*, "Bandgap engineering and manipulating electronic and optical properties of ZnO nanowires by uniaxial strain," *Nanoscale*, vol. 6, no. 9, pp. 4936–4941, 2014.

[17] K. Ordon *et al.*, "Investigations of the charge transfer phenomenon at the hybrid dye/BiVO 4 interface under visible radiation," *RSC Adv.*, vol. 9, no. 53, pp. 30698–30706, 2019.

[18] K. Hashimoto, H. Irie, and A. Fujishima, "TiO_2 Photocatalysis : A Historical Overview and Future Prospects," vol. 44, no. 12, pp. 8269–8285, 2006.

[19] Y. Li, W. Wang, Z. Zhan, M. Woo, C. Wu, and P. Biswas, "Applied Catalysis B: Environmental Photocatalytic reduction of CO_2 with H_2O on mesoporous silica supported Cu / TiO_2 catalysts," *"Applied Catal. B, Environ.*, vol. 100, no. 1–2, pp. 386–392, 2010.

[20] Y. Wang *et al.*, "Synthesis of one-dimensional TiO_2/V_2O_5 branched heterostructures and their visible light photocatalytic activity towards Rhodamine B," *Nanotechnology*, vol. 22, no. 22, 2011

[21] Q. Han, R. Setchi, and S. L. Evans, "Synthesis and characterisation of advanced ball-milled Al-Al 2 O 3 nanocomposites for selective laser melting," *Powder Technol.*, vol. 297, pp. 183–192, Sep. 2016.

[22] S. I. Siddiqui and S. A. Chaudhry, "Iron oxide and its modified forms as an adsorbent for arsenic removal: A comprehensive recent advancement," *Process Saf. Environ. Prot.*, vol. 111, pp. 592–626, Oct. 2017.

[23] T. A. Kurniawan, M. E. T. Sillanpää, and M. Sillanpää, "Nanoadsorbents for Remediation of Aquatic Environment: Local and Practical Solutions for Global Water Pollution Problems," *Crit. Rev. Environ. Sci. Technol.*, vol. 42, no. 12, pp. 1233–1295, Jun. 2012.

[24] D. La, T. Nguyen, L. Jones, and S. Bhosale, "Graphene-Supported Spinel CuFe2O4 Composites: Novel Adsorbents for Arsenic Removal in Aqueous Media," *Sensors*, vol. 17, no. 6, p. 1292, Jun. 2017.

[25] S. Yang, P. Wang, X. Yang, G. Wei, W. Zhang, and L. Shan, "A novel advanced oxidation process to degrade organic pollutants in wastewater: Microwave-activated persulfate oxidation," *J. Environ. Sci.*, vol. 21, no. 9, pp. 1175–1180, 2009.

[26] O. Tsydenova, V. Batoev, and A. Batoeva, "Solar-enhanced advanced oxidation processes for water treatment: Simultaneous removal of pathogens and chemical pollutants," *Int. J. Environ. Res. Public Health*, vol. 12, no. 8, pp. 9542–9561, 2015.

[27] C. Lettmann, K. Hildenbrand, H. Kisch, W. Macyk, and W. F. Maier, "Visible light photodegradation of 4-chlorophenol with a coke-containing titanium dioxide photocatalyst," *Appl. Catal. B Environ.*, vol. 32, no. 4, pp. 215–227, 2001.

[28] P. Ganguly, S. Panneri, U. S. Hareesh, A. Breen, and S. C. Pillai, "Recent Advances in Photocatalytic Detoxification of Water," in *Nanoscale Materials in Water*

Purification, Elsevier, 2019, pp. 653–688.

[29] S. E. Braslavsky *et al.*, "Glossary of terms used in photocatalysis and radiation catalysis (IUPAC recommendations 2011)," *Pure Appl. Chem.*, vol. 83, no. 4, pp. 931–1014, 2011.

[30] R. Ameta, M. S. Solanki, S. Benjamin, and S. C. Ameta, "Photocatalysis," in *Advanced Oxidation Processes for Waste Water Treatment*, Elsevier, 2018, pp. 135–175.

[31] F. Imtiaz, J. Rashid, and M. Xu, "Semiconductor Nanocomposites for Visible Light Photocatalysis of Water Pollutants," *Concepts Semicond. Photocatal.*, 2019.

[32] S. R. M. Thalluri, C. Martinez-Suarez, A. Virga, N. Russo, and G. Saracco, "Insights from Crystal Size and Band Gap on the Catalytic Activity of Monoclinic BiVO4," *Int. J. Chem. Eng. Appl.*, no. September 2013, pp. 305–309, 2013.

[33] D. Kong, Y. Zheng, M. Kobielusz, Y. Wang, Z. Bai, W. Macyk, X. Wang, J.Tang, "Recent advances in visible light driven water oxidation and reduction in suspension systems," *Mat. Today.*, vol.21, no. 8, pp.897-924, 2011.

[34] A. C. Dodd, A. J. McKinley, M. Saunders, and T. Tsuzuki, "Effect of particle size on the photocatalytic activity of nanoparticulate zinc oxide," *J. Nanoparticle Res.*, vol. 8, no. 1, pp. 43–51, 2006.

[35] S. K. Pardeshi and A. B. Patil, "Effect of morphology and crystallite size on solar photocatalytic activity of zinc oxide synthesized by solution free mechanochemical method," *J. Mol. Catal. A Chem.*, vol. 308, no. 1–2, pp. 32–40, 2009.

[36] P. N. Sibiya and M. J. Moloto, "Effect of precursor concentration and pH on the shape and size of starch capped silver selenide (Ag_2Se) nanoparticles," *Chalcogenide Lett.*, vol. 11, no. 11, pp. 577–588, 2014.

[37] M. Kamali, S. A. A. Ghorashi, and M. A. Asadollahi, "Controllable synthesis of silver nanoparticles using citrate as complexing agent: Characterization of nanopartciles and effect of pH on size and crystallinity," *Iran. J. Chem. Chem. Eng.*, vol. 31, no. 4, pp. 21–28, 2012.

[38] M. Mohamad, B. U. Haq, R. Ahmed, A. Shaari, N. Ali, and R. Hussain, "A density functional study of structural, electronic and optical properties of titanium dioxide: Characterization of rutile, anatase and brookite polymorphs," *Mater. Sci. Semicond. Process.*, vol. 31, pp. 405–414, 2015.

[39] A. Wold, "Photocatalytic properties of titanium dioxide (TiO2)," *Chem. Mater.*, vol. 5, no. 3, pp. 280–283, Mar. 1993.

[40] S. Y. Lee and S. J. Park, "TiO_2 photocatalyst for water treatment applications," *J. Ind. Eng. Chem.*, vol. 19, no. 6, pp. 1761–1769, 2013.

[41] X. Meng and Z. Zhang, "Bismuth-based photocatalytic semiconductors: Introduction, challenges and possible approaches," *J. Mol. Catal. A Chem.*, vol. 423, pp. 533–549, 2016.

[42] H. AN, Y. DU, T. WANG, C. WANG, W. HAO, and J. ZHANG, "Photocatalytic properties of BiOX (X = Cl, Br, and I)," *Rare Met.*, vol. 27, no. 3, pp. 243–250, 2008.

[43] K. Tolod, S. Hernández, and N. Russo, "Recent Advances in the BiVO4 Photocatalyst for Sun-Driven Water Oxidation: Top-Performing Photoanodes and Scale-Up Challenges," *Catalysts*, vol. 7, no. 12, p. 13, Jan. 2017.

[44] W. Jiang *et al.*, "Efficient photoelectrochemical water oxidation using a TiO 2 nanosphere-decorated BiVO 4 heterojunction photoanode," *RSC Adv.*, vol. 8, no. 72, pp. 41439–41444, 2018.

[45] M. Han, X. Chen, T. Sun, O. K. Tan, and M. S. Tse, "Synthesis of mono-dispersed m-$BiVO_4$ octahedral nano-crystals with enhanced visible light photocatalytic properties," *CrystEngComm*, vol. 13, no. 22, pp. 6674–6679, 2011.

[46] V. I. Merupo, S. Velumani, K. Ordon, N. Errien, J. Szade, and A. H. Kassiba, "Structural and optical characterization of ball-milled copper-doped bismuth vanadium oxide ($BiVO_4$)," *CrystEngComm*, vol. 17, no. 17, pp. 3366–3375, 2015.

[47] Y. Park, K. J. McDonald, and K. S. Choi, "Progress in bismuth vanadate photoanodes for use in solar water oxidation," *Chem. Soc. Rev.*, vol. 42, no. 6, pp. 2321–2337, 2013.

[48] S. Tokunaga, H. Kato, and A. Kudo, "Selective preparation of monoclinic and tetragonal $BiVO_4$ with scheelite structure and their photocatalytic properties," *Chem. Mater.*, vol. 13, no. 12, pp. 4624–4628, 2001.

[49] B. Cao, J. Peng, and Y. Xu, "Simulated Sunlight-Driven Degradation of Rhodamine B by Porous Peanut-Like TiO_2/$BiVO_4$ Composite," *J. Clust. Sci.*, vol. 24, no. 3, pp. 771–785, 2013.

[50] Y. Hu, D. Li, H. Wang, G. Zeng, X. Li, and Y. Shao, "Role of active oxygen species in the liquid-phase photocatalytic degradation of RhB using $BiVO_4$/TiO_2 heterostructure under visible light irradiation," *J. Mol. Catal. A Chem.*, vol. 408, pp. 172–178, 2015.

[51] A. P. Singh, N. Kodan, B. R. Mehta, A. Held, L. Mayrhofer, and M. Moseler, "Band Edge Engineering in $BiVO_4$/TiO_2 Heterostructure: Enhanced Photoelectrochemical Performance through Improved Charge Transfer," *ACS Catal.*, vol. 6, no. 8, pp. 5311–5318, 2016.

[52] M. Wang *et al.*, "Synthesis of $BiVO_4$-TiO_2-$BiVO_4$ three-layer composite photocatalyst: Effect of layered heterojunction structure on the enhancement of photocatalytic activity," *RSC Adv.*, vol. 6, no. 79, pp. 75482–75490, 2016.

[53] D. Hongxing, L. Qiuping, and H. Yuehui, "Preparation of nanoporous BiVO 4 /TiO 2 /Ti film through electrodeposition for photoelectrochemical water splitting," *R. Soc. Open Sci.*, vol. 5, no. 9, p. 180728, Sep. 2018.

[54] O. Monfort *et al.*, "Journal of Environmental Chemical Engineering Photooxidative properties of various BiVO4 / TiO2 layered composite fi lms and study of their photocatalytic mechanism in pollutant degradation," vol. 5, pp. 5143–5149, 2017.

[55] B. Y. Cheng, J. S. Yang, H. W. Cho, and J. J. Wu, "Fabrication of an Efficient BiVO4-TiO2 Heterojunction Photoanode for Photoelectrochemical Water Oxidation," *ACS Appl. Mater. Interfaces*, vol. 8, no. 31, pp. 20032–20039, 2016.

[56] X. Lin *et al.*, "Visible light photocatalytic activity of $BiVO_4$ particles with different morphologies," *Solid State Sci.*, vol. 32, pp. 61–66, 2014.

[57] C. Yang *et al.*, "Adhesive-free in situ synthesis of a coral-like titanium dioxide @ poly (phenylene sulfide) microporous membrane for visible-light photocatalysis," vol. 374, no. May, pp. 1382–1393, 2019.

CHAPTER. 2

Experimental methodology and instrumentation

This chapter presents the sol-gel used for preparing the TO/BVO nanocomposites and a description of the RF-sputtering technique for preparing layered heterostructure films. It also described the various characterizations (XRD, Raman, BET, SEM, UV-Vis absorption, TEM, and electrochemical techniques) for the synthesized nanomaterials. The chapter also describes some operating principles for the techniques and experimental setup used in the study.

2.1 Sol-gel Synthesis

The sol-gel synthesis is a wet chemical method commonly used to synthesize nanoparticles, e.g., metal oxides. It is known as a 'soft route' because it employs comparatively lower temperatures than other traditional ceramic processes. The process starts with the precursor solutions containing the metal alkoxides or metal-organic salts for metal oxide deposition, and familiar sources of the precursors include metal chlorides [1]. The precursors dissolved in some base solvents, e.g., alcohols, water, help prepare the solution, labeled "sol." The sol is a suspension of the colloidal particles in the liquid form [2], and undergoes a hydrolysis reaction with the solvents, and forms a gel under continued condensation reactions. The gel presents a network of semi-rigid solution that has transformed from sol.

2.1.1 Main steps for the sol-gel synthesis process

- Hydrolysis: Hydrolysis and partial condensation of the alkoxides results in the formation of the sol
- Gelation/polymerization: this step involves forming the M-O-M (Metal-Oxygen-Metal) or M-OH-M (Metal-Hydroxyl-Metal) bonds by polycondensation, creating a gel-like structure
- Reaction duration: this refers to the time it takes for the condensation of the molecules, allowing for the potential removal of the excess solvents
- Drying: this step allows for the collapse of the porous network to form the xerogel.

- Dehydration/calcination: this commonly used final step allows for removing the surface M-OH groups and other residual solvents at a higher temperature. For the TO/BVO synthesis in this study, the temperature is 500°C.

The precursors react with the solvents (e.g., water or alcohol) during hydrolysis to form links between adjacent molecules and metal oxide linkages during the polymerization. These polymeric links are further enhanced through gelation to form a gel network, and the aggregation results in the aging of the gel. During the drying process with the application of temperature gradients, the gel gets shrink with the solvents' evaporation. Finally, calcination at a higher temperature (e.g., 500°C) helps eliminate the chemically bound water and other chemical residues that might still be present. Some experimental parameters affecting the reactions include pH of hydrolysis, amount of used water solvent, gelation temperature, calcination temperature.

2.1.2 Synthesis of BVO

BVO nanoparticles were prepared by the sol-gel method by using 0.01mol $Bi(NO_3)_3.5H_20$ dissolved in 50ml of HNO_3(10%) and adding 0.02 mol citric acid. The mixture was stirring until a colorless solution was observed (solution A). A 0.01 mol of NH_4VO_3 was dissolved in 50 ml of deionized water and then heated at 80 °C with magnetic stirring until a clear lemon-yellow solution was obtained. Subsequently, 0.02 mol of citric acid was added until a brown solution was obtained (solution B). Solution A was then added dropwise to solution B leading to a final mixture with intense blue coloration. In the next step, the pH adjustment was carried out with an NH_4OH solution to obtain a pH of 6.5 needed to catalyze the hydrolysis process. The mixture was then stirring at the same temperature until a gel formation, which was afterward dried at 100 °C overnight. The obtained powder was calcinated for 2 hours at 500 °C and finally ground and kept in a desiccator before its characterization and use in pc tests.

2.1.3 Synthesis of TO/BVO composites

The titanium (IV) oxide, anatase nano powder (99.7% trace metals basis) used for the studies was purchased from Sigma-Aldrich and used without further chemical processing. Three TO/BVO composites with different nominal compositional ratios were selected at 0.2:0.8, 0.5:0.5, and 0.8:0.2. The different ratios were prepared by maintaining a constant concentration of BVO in the precursor (section 2.2) and changing the amount of the added TO. The synthesis of the nanocomposites was conducted according to the BVO synthesis

protocol [3]. $Bi(NO_3).H_2O$ was dissolved in HNO_3 and later citric acid was added and this transparent solution constitute the solution A. The solution B was prepared by dissolving the NH_4VO_3 in the distilled water at 60°C. Once this solution turns lime yellow color, the citric acid was again added. Both the solutions A and B was mixed together to form the solution C as in fig.2.1. Then the system was maintained at 60°C. Before the pH adjustment stage, the TO with mass corresponding to the ratio to be synthesized (0.2:0.8, 0.5:0.5, and 0.8:0.2) was incorporated. Subsequently, the mixture was placed in an ultrasonic bath for 30 min to allow the components of the mixture to blend perfectly. Next, pH adjustment, drying, and calcination of the sample was performed. The drying was done during the overnight at 100° C to remove all the aqueous remaining. The volatile compounds were removed by calcination at 500 ° C for 2 hours [4].

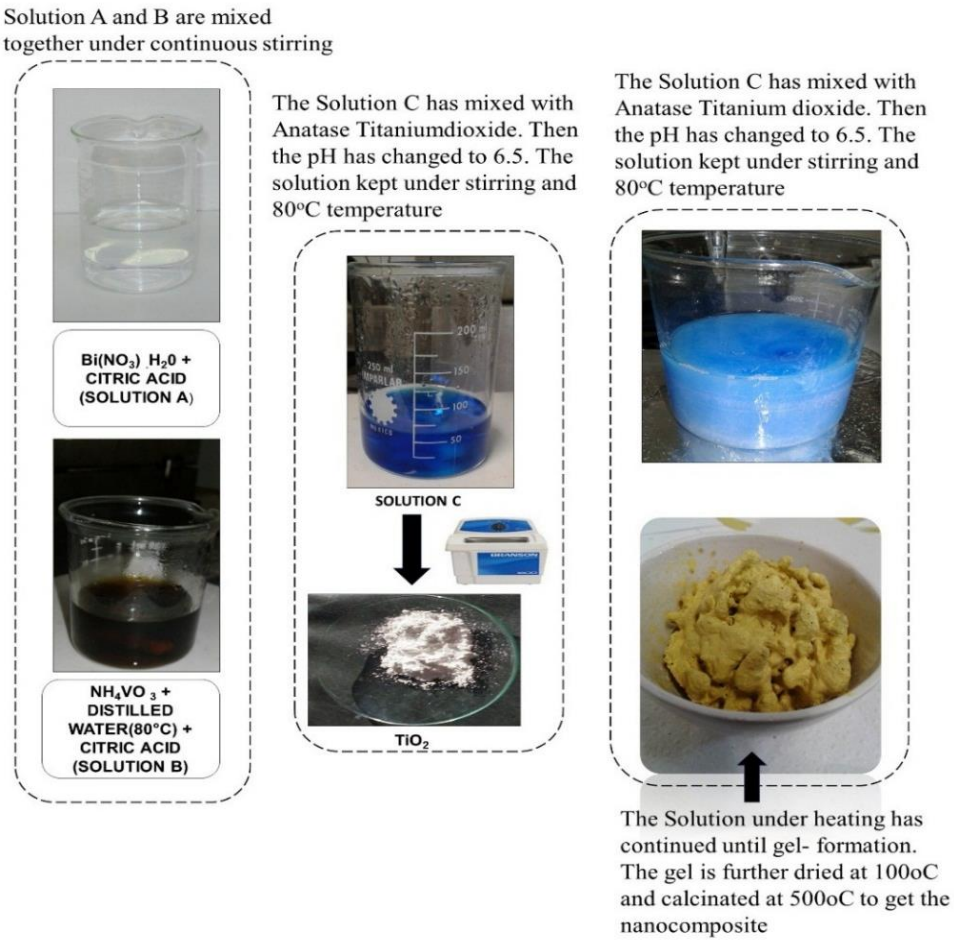

Fig. 2.1 Sol-gel Synthesis step

2.2 Deposition of films by RF Sputtering

Radio-frequency sputtering is a robust technique for depositing layers of various materials, including metals and ceramics. The optimization of the RF-sputtering parameters for the deposition of films of TO/BVO in this study considered obtaining two different architectures,

- Nanocomposite film
- Layered heterostructure film with a TO layer over a BVO layer on various substrates

2.2.1 Working principle

The experimental set-up for RF-sputtering deposition is illustrated below:

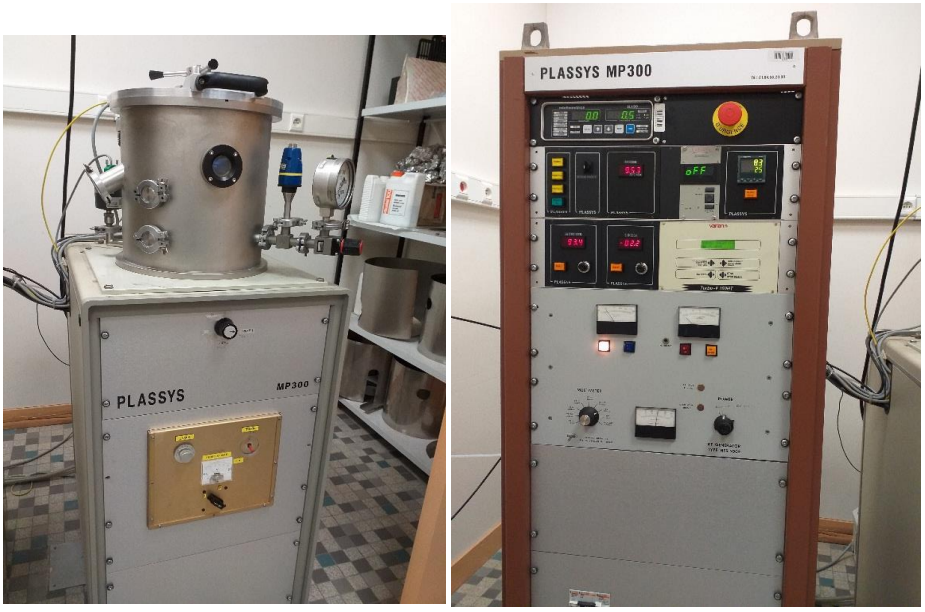

Fig. 2.2 Plassys MP300 RF sputtering equipment

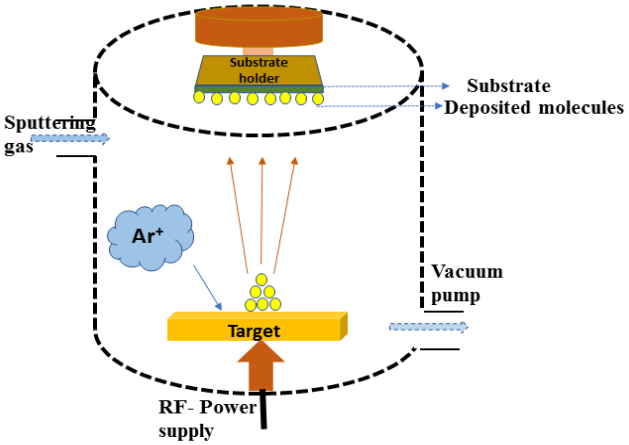

Fig. 2.3 Schematic representation of the sputtering process

The sputtering target is connected to the cathode, while the substrate holder is the anode. The deposition chamber contains a defined partial pressure of argon or argon-oxygen mixture. With voltage application, the gas is ionized and then forms a plasma inside the chamber between the target and substrate. The Ar^+ ions bombard the target surface, knocking off atoms that migrate to the substrate get deposited over the substrate's surface. Some advantages of the RF-sputtering deposition include:

- The sputtering can be at room or higher temperatures, with better morphology and crystalline features of the deposited films.
- The choice of the relevant substrates ensures good adhesion between the film and the substrate and favors the relevant crystalline phases.
- A suitable deposition rate can be achieved within a limited time.
- Better uniformity of the film can be realized by choosing the film deposition parameters (e.g., power, pressure).
- Long term stability, good controllability, and reproducibility of the deposition process
- Alloys and compounds with different vapor pressure can be deposited.
- Insulators and semiconductor oxide films can also be deposited without causing any charge accumulation on the target surface.
- It can be scaled up to larger areas with a comparatively cheap deposition method.

2.2.2 RF-sputtering of TO/BVO films

Films of TO/BVO were deposited by RF-magnetron sputtering using the PLASSYS MP300 machine (fig. 2.4). The target pellets of the BVO, TO, and the sol-gel synthesized nanocomposite BVO: TO (0.5:0.5) have been made with a hydraulic pressure system, with a diameter of 2cms under the pressure of 9 Tons. Furthermore, the pellets have been introduced into the Novotherm oven for the sintering process. Then, the sintering has been done for 2 hours under 500°C. The sintered target and the substrates have been introduced into the sputtering chamber. Later the chamber was evacuated to a pressure of $5 \cdot 10^{-6}$ Pa. The deposition process has been initiated once the desired vacuum is achieved. The deposition parameters were optimized before beginning the depositions. The substrate with and without heating was tested and found that both conditions required annealing after the deposition.

For the low energy consumption, the Argon alone condition has been chosen. The incident powers have been used at 25, 50, and 75W, and an optimized value at 50W was chosen. It was also investigated the deposition atmosphere with Ar alone and (Ar-O_2) mixture. As the films with Ar alone have shown desired crystalline features, the depositions were done under the pure Argon condition at room temperature.

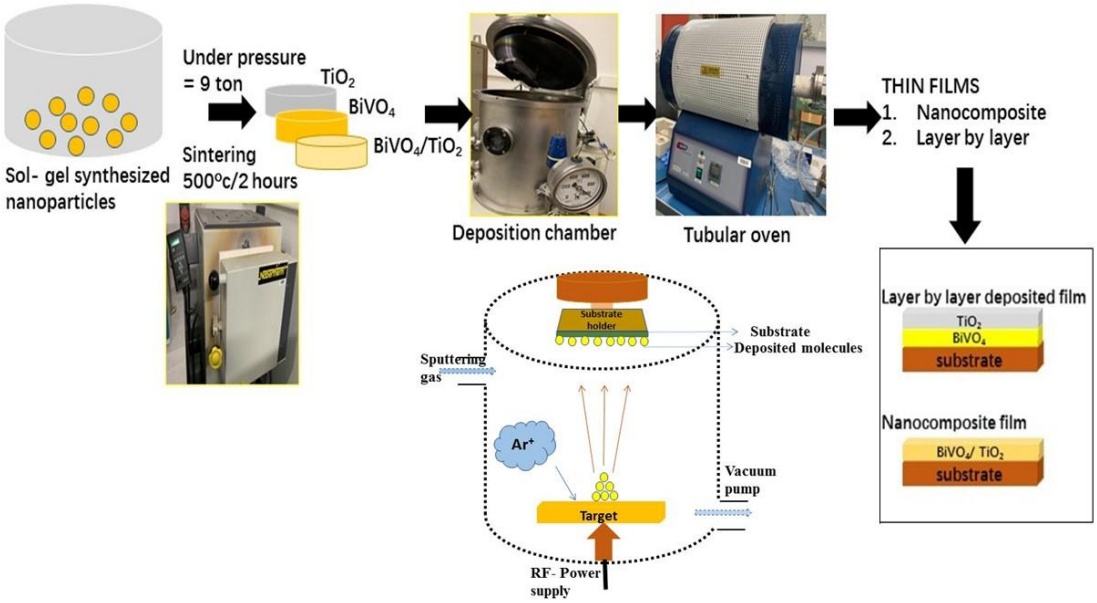

Fig. 2.4 Schematic of the RF- sputter deposition of the films

In the forthcoming lines, two different configurations of TO/BVO films were realized by the RF-sputtering technique. On the one hand, composites films were formed by the coexistence of BVO and TO domains. On the other hand, a layered configuration was realized by deposition of TO layer onto BVO layer on different substrates. The nature of the substrates was considered in the present studies due to the expected effects on the physical features of deposited compounds. This will be discussed in the chapter.5.

2.3 Characterization methods

2.3.1 X-Ray Diffraction Analysis

The synthesized samples' structural characterizations were performed using a diffractometer (Bruker-D2 Phaser) at 30kV with Cu K_α radiation (ƛ=1.5418Å). The films were characterized using a *PANalytical Empyrean* diffractometer equipped with a cryostat, which allows in-situ measurement of XRD patterns between room temperature up to 750°C.

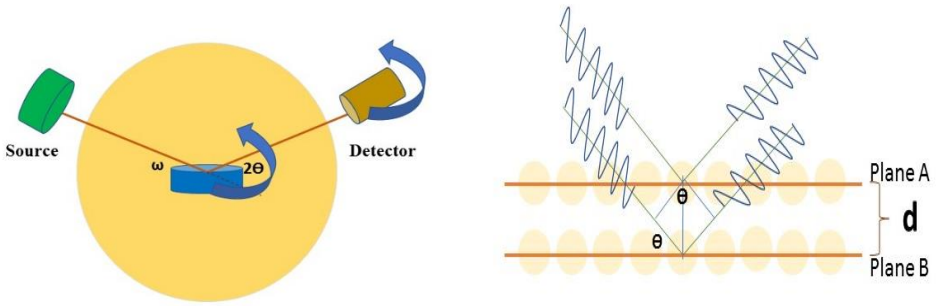

Fig. 2.5 Illustration of the principle of xrd.

Fig. 2.6 PANalytical Empyrean X-ray diffractometer

The diffraction patterns were recorded as a function of 2θ ranging from 10° to 80°. Using the diffraction line width (FWHM), we can estimate the size (D) of crystalline domains through Scherrer's equation:

$$D = {K\lambda}/{\beta cos(\theta)} \qquad (1)$$

Where D is the crystallite size, K is the shape factor with a value close to unity, λ is the X-ray wavelength, Cu Kα=0.154 nm, β is the full-width half maxima (FWHM) of the peak at a particular plane in radians, and θ is the Bragg angle. The measurements have been carried out under variable ω and step size conditions to find the best measurement conditions.

The position of the detector is identified as the 2θ (along X-axis) value, and the intensity of the radiation is noted as Counts (along Y-axis). Different phases of the materials can have distinct diffraction patterns, and their analysis was realized by the software PanAnalytical HighScore.

2.3.2 Raman Analysis

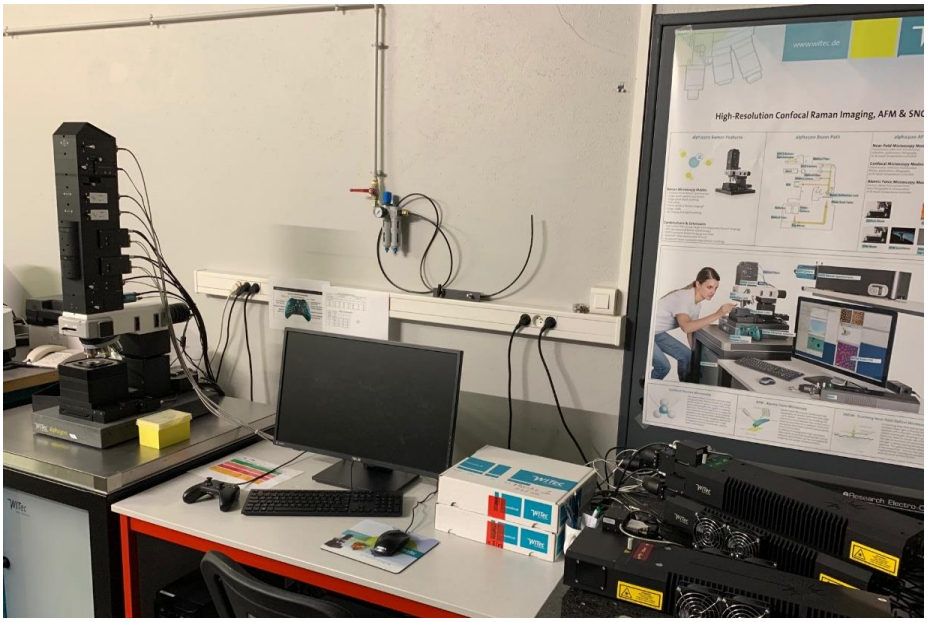

Fig. 2.7 WiTech Raman spectrometer

Raman analysis is a characterization technique based on the Raman effect emanating from the interaction of the inelastically scattered radiations by the molecular vibrations. Raman analysis was carried out for the molecular vibrational analysis using a Witec Alpha 300R microscope. The excitation wavelength used for the measurement was 532nm under the power of 5mW. A coherent irradiation source is used (such as a laser source). When molecules absorb photons with defined wavelengths, the emitted photons may have the same or different higher or lower wavelengths. Phonons are involved in these processes and account for the molecular vibrations. Due to irradiation, scattering occurs (both elastic and inelastic scattering).

Raman scattering is the elastic one that constitutes both stokes and anti-stoke scattering. Three different types of scattering can occur,

- Stokes scattering
- Anti- stoke scattering

- Rayleigh Scattering

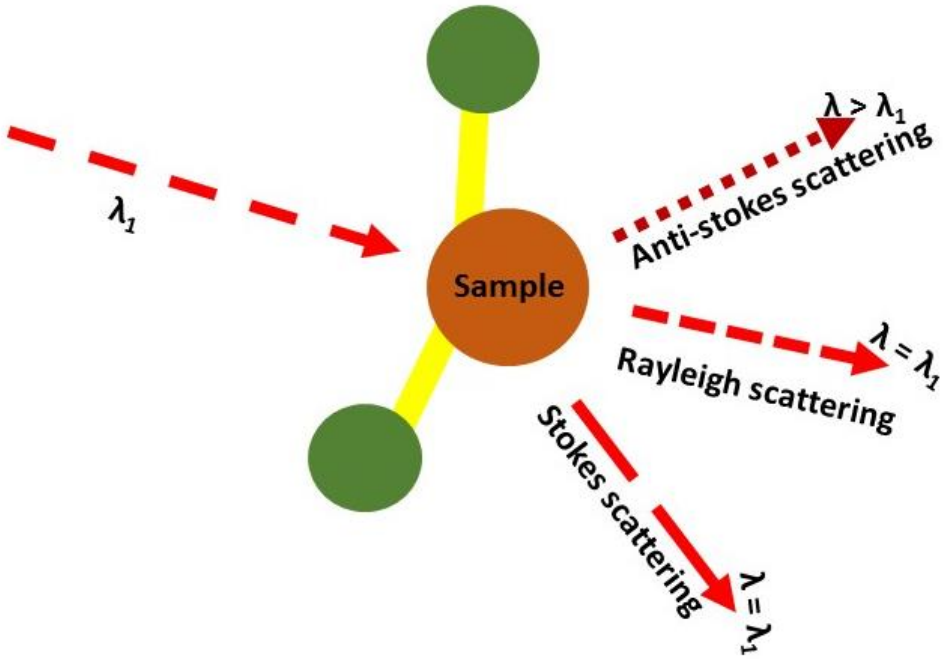

Fig. 2.8 Principle of Raman spectrum

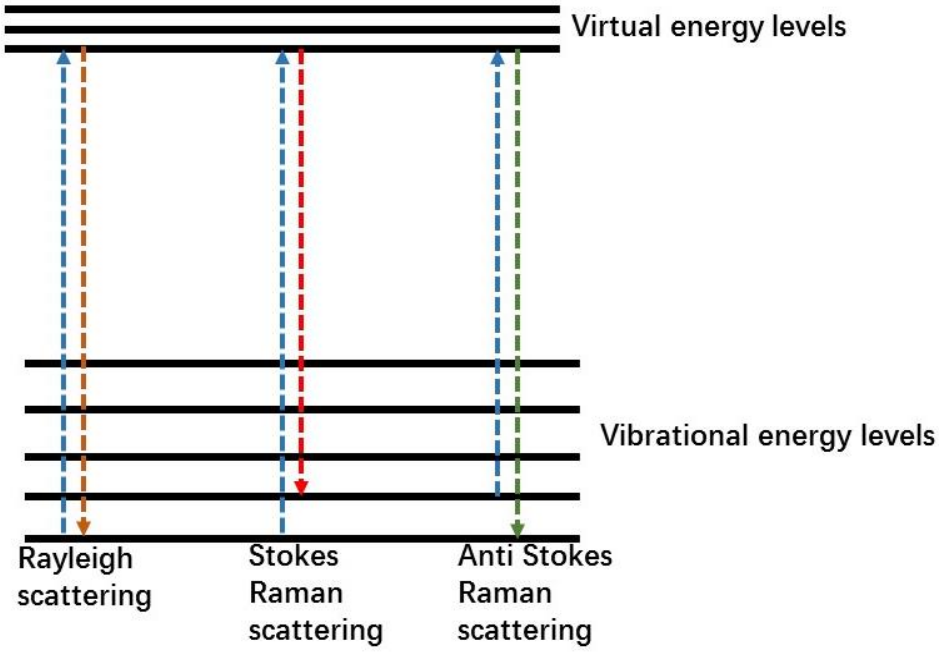

Fig. 2.9 Representation of molecular scatterings

The energy difference between the incident and Raman scattered photons will give information on the vibrational nature of the sample molecule.

$$\boldsymbol{\Delta\nu\ (cm^{-1}) = \frac{1}{\lambda 1} - \frac{1}{\lambda}} \qquad (2)$$

$$\boldsymbol{\lambda 1}\ \textit{is the wavelength of the initial incident photon}$$

$$\boldsymbol{\lambda}\ \textit{is the scattered wavelength}$$

The Raman process is then based on the scattering of the coherent laser source used for the measurements. The peak positions of the raman lines are determined by the vibrational energies associated with the molecular bonding. This technique determines vibrational, rotational, and other frequency modes [5,6].

Raman studies were performed on different TO/BVO forms as powders or in the form of composite or layered films. The vibrational properties of the samples provide information on their crystalline features from their crystalline phases and the crystalline quality.

2.3.3 UV-Vis spectroscopy

Fig. 2.10 Agilent Cary v-670 Spectrophotometer

UV- Vis spectroscopy measures the optical absorbance of the materials on a wide spectral range and evaluates their electronic bandgaps. For our experiments, the optical spectra of the samples were obtained from a UV-Vis spectrophotometer (Agilent Cary-Fig. 2.10). The main parts of the spectrometer consist of a light source, sample holder, a monochromator for the light analysis, and a detector. The absorption spectra arise due to the transitions from the

valence to the conduction band in condensed matter samples. The spectrometer configuration must be then equipped by integrating sphere, and the measurements concern the diffuse reflectance spectra (DRS). The absorption curves can be deduced based on the Tauc -plot. In the case of doped materials or defects, the band levels of dopant may act as an inter-band. These levels may contribute to the absorption of other wavelengths compared to pure materials. Thus, the UV-Vis spectrophotometry technique is a suitable tool to analyze the difference in the band gap properties due to the doping or defect effects. In the case of molecular systems absorption spectra can be recorded. The transitions require photon energy that is equal to the difference between the Highest Occupied Molecular Orbitals (HOMO) and the Lowest Occupied Molecular Orbitals (LUMO) of the considered molecules. Similar measurements were carried out to study the pc processes for water purification from pollutants such as organic dyes or the compounds that may give the absorbance response. The principles of the measurement of organic dyes in a solution are described below.

The sample is prepared in deionized water with a defined concentration of organic dyes. The measure on a blank solution (usually water or alcohol solvent were the contaminant model is prepared) is performed as a first step. This is to create a baseline, where the transmitted intensity is recorded under different wavelengths. In the current studies, water is the bblank solution. When the light passes through the sample (with an initial intensity I_0), the light is absorbed by the sample molecules, and the transmitted intensity (I) will be detected.

Hence transmittance is given as;

$$\boldsymbol{T = \frac{I}{I_0}} \qquad \textbf{(3)}$$

And the absorbance was obtained from the optical transmittance (absorbance as the negative logarithm of transmittance) value as;

$$\boldsymbol{A = -\log(T)} \qquad \textbf{(4)}$$

Hence the spectrum can be represented as the absorbance versus the wavelength.

And the absorbance can also be represented using the expression (Beer Lambert's law) [7];

$$\boldsymbol{A = \varepsilon \cdot c \cdot d} \qquad \textbf{(5)}$$

i.e., the absorbance is represented as a function of the concentration and the length of the light-path, d, while $\boldsymbol{\varepsilon}$ represents the extinction coefficient. Equation (5) determines the

absorbance of a sample at a particular wavelength, concentration (mol/l or g/l), and the length of the cuvette (or path length, in cm).

2.3.4 Scanning electron Microscopy

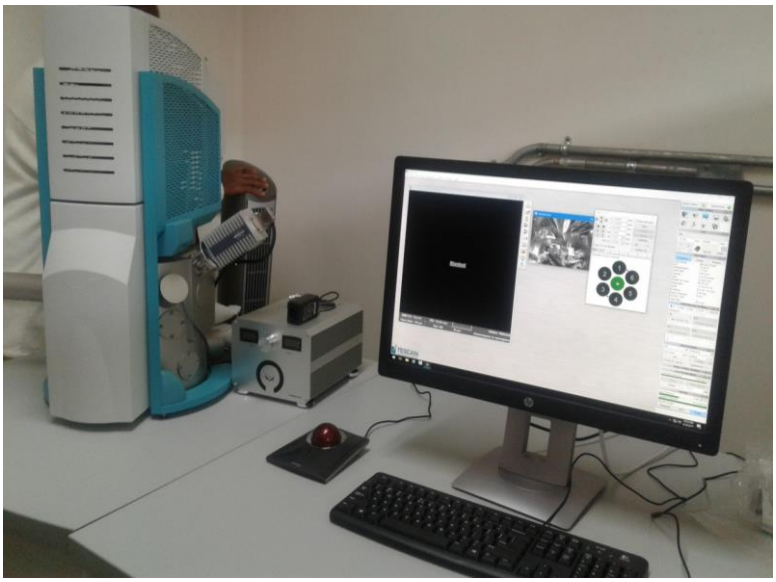

Fig. 2.11 SEM-VEGA3 (MREB-CINVESTAV)

A scanning electron microscope is used for the morphology and chemical analysis of the materials under a high energy electron beam. Electrons from a schottky-field emission cathode are accelerated by a potential difference between the cathode and anode [8]. The source of electrons is usually a tungsten filament or a field emission gun. The whole system contains the path of the electron beam with apertures and electromagnetic lenses to produce a concentrated beam of electrons. Once the beam impinges on the sample surface, electrons are ejected and received by the detector. There are different types of detectors, such as a secondary electron detector, a backscattered electron detector, and X-ray detector, which detects the way of interaction of the electron beams over the sample surface [8].

Powder samples were dispersed ultrasonically in methanol. A few drops of the dispersion were dried directly on carbon tape to carry out the SEM analysis (MIRA3 and VEGA3 TESCAN). The compositions were analyzed using an energy dispersive X-ray spectrometer (EDS) coupled with the SEM.

2.3.5 Transmission Electron Microscope

The morphological and grain analysis of the nanocomposites have been carried out using the transmission electron microscope. The measurement has been done with the JEOL JEM

2100 HR Transmission Electron Microscope (Jeol ltd. Tokyo, Japan). As the name indicates, the images are formed by the transmitted electrons.

Fig. 2.12 JEOL JEM 2100 HR TEM (Jeol ltd.) (IMMM- Le Mans)

The electron source is a material with a higher work function. Once the acceleration voltage is applied to the source, electrons are ejected. As the acceleration voltage increases, the wavelength of the electron beam decreases due to its wave nature and results in better resolution. The magnification of images depends on the illuminated area of the sample. TEM has two modes of operation; Bright-field (BF) and Dark-field (DF). The bright-field is the standard mode of operation. In BF, the samples with high atomic number, thickness, and density appear darker and appear brighter when the factors mentioned earlier are low. Hence, we can see the atomic weight contrast (Z- Contrast) images. The selected area diffraction (SAED) allows the selection of particular areas, which generates the fourier transform (FFT) of the periodic lattice. Depending on the crystallinity of the material, the FFT pattern can change. In amorphous ones, the FFT pattern will be like a diffused ring (fig.2.14 a), whereas in the case of the crystalline lattice, there forms a pattern with defined points (2.14 b).

In the TO/BVO samples, the obtained TEM images were mapped to extract the FFT pattern over all the grain areas shown. The TEM image shows a clear overlap between two

nanocomposites, the FFT pattern over all the image was extracted. The entire area was divided into regions, depending on the bright and dark channels that show the crystalline growth. Only when a particular region showed a single result of atomic plane spacing in the calculated FFT, that area is assigned to the characteristic crystalline plane of either BVO or TO, depending on the interplanar distance value reported in their respective diffraction card. Slab structures were generated utilizing the BIOVIA Materials Studio Package to correlate this experimental result with a computational model. In our case, both lattice parameters and space groups define the crystalline structure from BVO and TO. The graphical resemblance, along with the unitary slab thickness, extracted from the simulated crystal, cleavage parallel to the FFT calculated planes, may give the information on the crystallinity of the mapped area.as discussed in the chapter. 3.

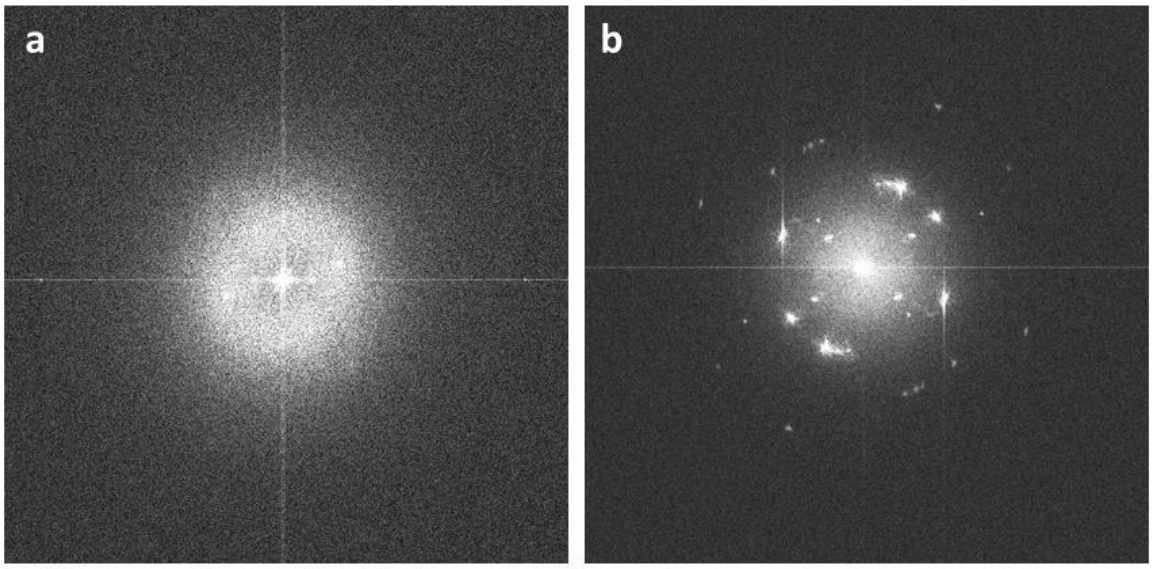

Fig. 2.13 FFT of a) amorphous and b) crystalline samples.

2.3.6 Atomic Force Microscopy

Atomic force micrographs (AFM) are obtained using the NT-MDT, NTEGRA Spectra, in the contact mode. The measurements were made under ambient conditions. The results were analyzed using IAP and Gwyddion softwares. The basic concept in this characterization technique is the interaction between the tip and the sample.

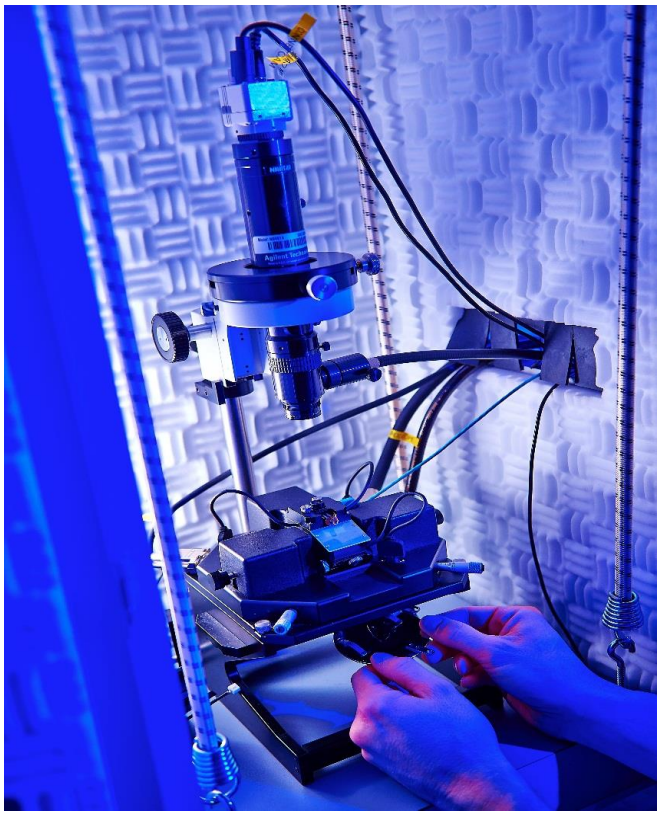

Fig. 2.14 AFM- T-MDT, NTEGRA

These interactions can be electrostatic, magnetic, or even interatomic interactions. The central part of the instrument is a cantilever with a fine tip that interacts with the sample, and it acts as a spring with a spring constant from 0.01 to 100 $N.m^{-1}$ [9]. A piezoelectric mechanism controls the sample in relation to the tip, and the display system converts the data into graphical representations. The sensor with sub-angstrom sensitivity detects the cantilever deflections [10]. There are different modes of interaction between the tip and the film.

- Tapping mode: In this case, the cantilever oscillates at a resonance frequency with an absolute amplitude. The tip-surface interaction force changes the oscillations. Changes in the amplitude and phase will be recorded as a function of the tip-sample position
- Contact mode: The tip comes to the close proximity of the sample surface with constant interaction
- Non- contact mode: In this mode, the force sensor oscillates (the oscillation amplitude kept constant to a small value nearly $1A^{o}$ to few nanometers) initially at its resonance frequency before reaching the proximity of the surface

2.3.7 Profilometer

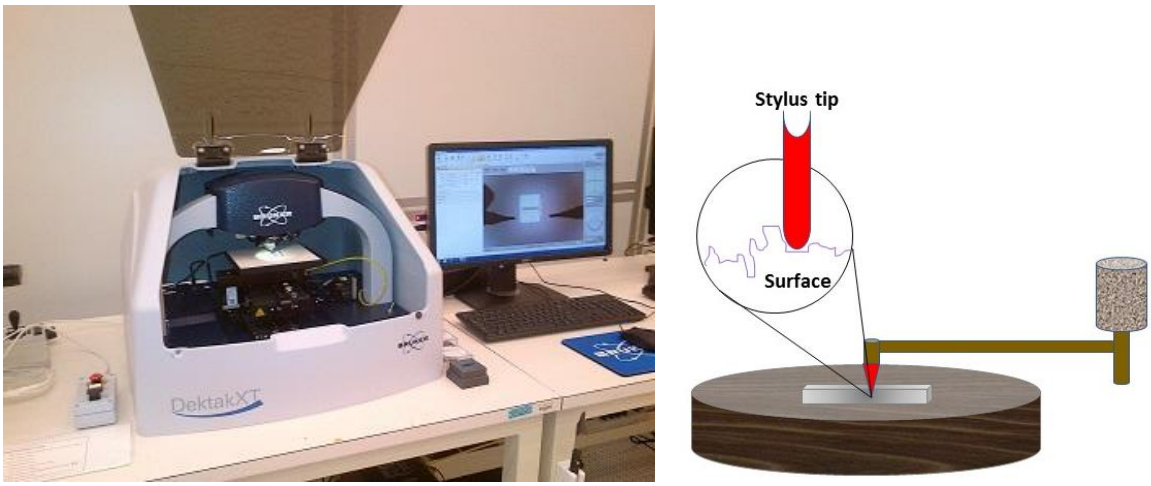

Fig. 2.15 Dektat XT profilometer- with schematic diagram

Profilometry is a contact technique used for the measurement of the surface profile h(x,y) of the films [11] with h being the height at (x,y) point of the surface plane. The stylus as a tip is in close contact with the surface, which physically moves along the surface and detects the surface depending on the height variation. The vertical displacement of the stylus is measured within the range of 10nm to 1mm.

2.3.8 Brunauer Emmet Teller- Surface area measurement

The BET surface area analysis has been performed using a Quantachrome Absorber 1 equipment. This technique can measure the surface area, pore-volume, and pore size distribution. The main information provided is the available surface area of the material for the adsorption of the gas molecules. The reduced particle size can give rise to a higher surface area. The gas adsorption can occur via physisorption or chemisorption. Chemisorption is considered as a more vital interaction than the physisorption process since it needs higher energy for desorption [12]. The most common adsorbate used for BET measurements is nitrogen gas.

Depending on these interactions, there can have different adsorption isotherms (Type- I, II, III, IV, and V) depending on which materials can be microporous (>2nm), mesoporous (<2-50nm), macroporous (>50nm), isoporous or even can be a network of pores (1-100nm) [13].

The main relation exploited in the BT measurements is as follows (6):

$$\frac{x}{v(1-x)} = \frac{1}{v_m \cdot C_{BET}} + \frac{x \cdot (C_{BET}-1)}{v_m \cdot C_{BET}} \qquad (6)$$

$$v = Volume\ of\ the\ adsorbed\ molecules$$

$$v_m = Monolayer\ volume$$

$$C_{BET} = BET\ Constant, which\ is\ related\ to\ the\ adsorbent,$$

$$adsorbate\ interaction\ strength$$

$$x = \frac{P}{P0} \qquad (7)$$

The classical BET equation is given by;

$$\frac{1}{V}\frac{x}{(1-x)} = \frac{(c-1)}{cV_n}x + \frac{1}{cV_m} \qquad (8)$$

Fig. 2.16 Quantachrome Absorber 1

It is worth noting that the measurement requires careful sample preparation. It is essential to degas all the existing adsorbed gasses before starting the measurement, since it can cause the molecules to cover the surface, and in turn, it could modify the adsorption rates less in the wrong way by blocking the space for the desired adsorbate.

2.3.9 Photoelectrochemical characterization

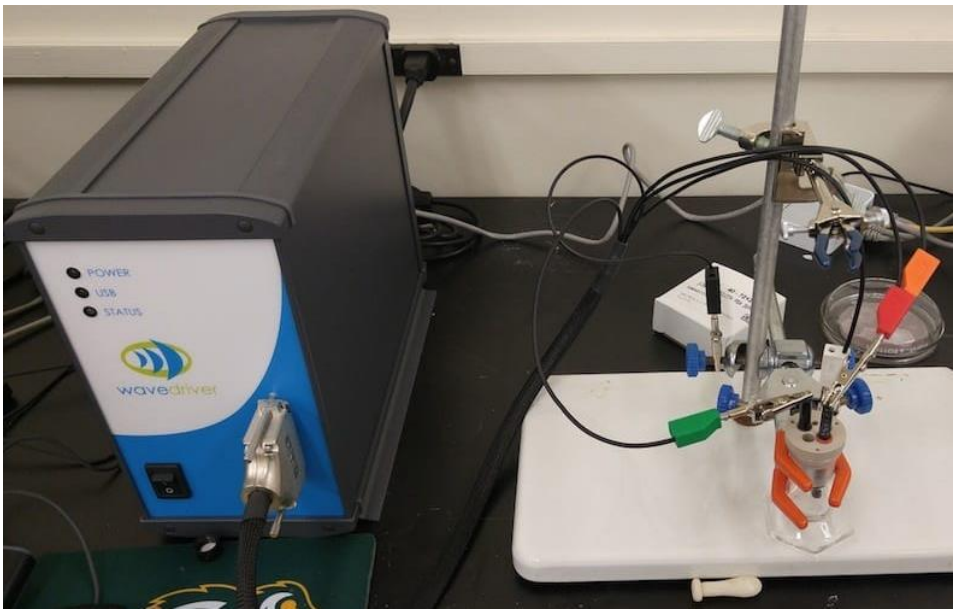

Fig. 2.17 Autolab PGSTAT 302N Potentiostat

The materials were deposited as films through a suspension of the powder samples in Nafion-ethanol solution. An aliquot of each investigated sample was dispersed over 0.24 cm^2 ITO substrate, previously cleaned in acetone and then with water. All films were dried at room temperature for 24 hours. Electrochemical determinations were performed in a conventional three-electrode cell. Ag/AgCl/3 M KCl electrode was used as the reference electrode [EAg/AgCl/3M KCl = 0.210 V/SHE]. The counter electrode was a graphite rod (99.9995% pure, Alfa Aesar), and the prepared films on ITO substrates were used as a working electrode. $NaClO_4$ (0.05 M) solution was used as the supporting electrolyte. The illumination was performed using a Newport Q Housing (Model 60025) equipped with a visible light lamp. The semiconducting properties of the films were estimated from the Mott-Schottky plots. The space charge capacitance of the film was potential-dynamically measured in the dark (v = 20 mV. s^{-1} at a frequency of 100 Hz). EIS measurements were performed at open circuit potential in the dark and under illumination in a frequency window between 100 kHz and 100 MHz with an AC voltage of ±10 mV (peak to peak). For the (photo)electrochemical measurements, an Autolab PGSTAT 302N potentiostat was used.

2.4 Photocatalytic dye degradation- Quantification methodology

The pc activity of the pure TO, BVO, and TO/BVO nanocomposite was studied with the help of a full reflective solar simulator equipped with a 1.6 kW Xenon Arc Ozone free lamp (Sciencetech VHE-NL-200).

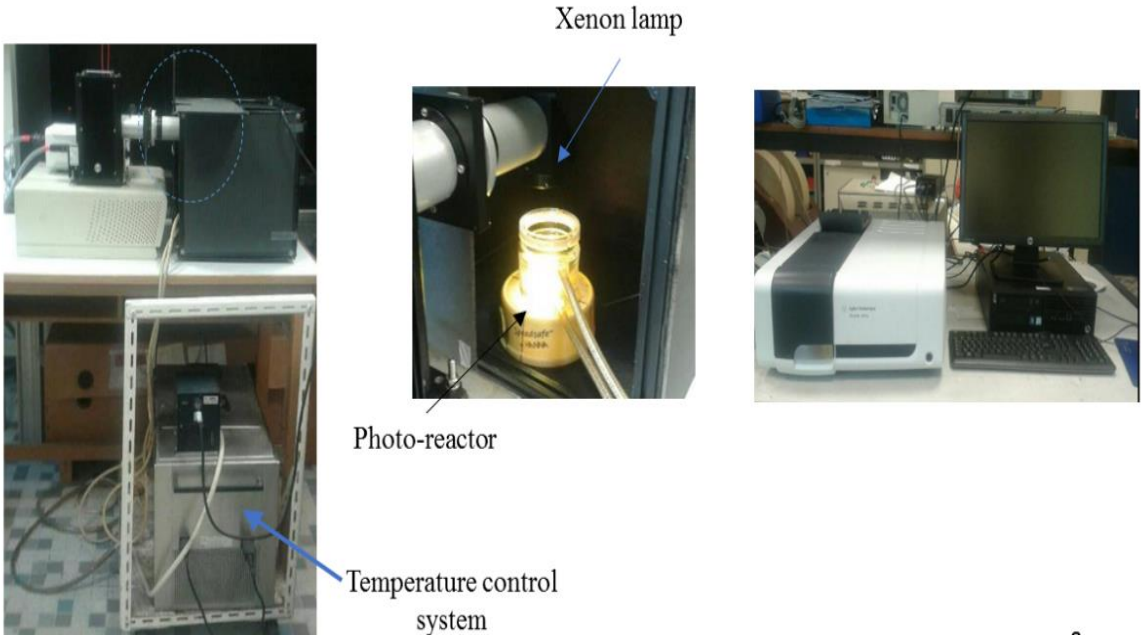

Fig. 2.18 Pc experimental set-up

The main aim is to choose the sample with the highest pc activity was selected. Pyrex® glass vessels was used as reactor. The glass vessels containing 100 ml of the AB113 solution with an initial concentration of 40 mg/l and the amount of the nanocomposite used for the primary tests was of the dosage of 1 g/l. Before irradiation, the sample was stirred in order to reach an adsorption-desorption equilibrium. Afterward, the suspension was stirred continuously for two hours until the reaction lasted. About 3 ml aliquot of the dye solution was withdrawn after a specific time interval. The samples were filtered, and their absorbance was recorded at λ_{max} =568 nm (AB113) using a UV-visible spectrophotometer (Jasco V-670). The initial pH of the dissolution was 6, and no adjustment was made during experiment. Once the selection of the material with the highest pc activity was made, the effect of the initial dose of the photocatalyst (1, 2, 3, 4, and 5 g/l) and the initial concentration of the dye (20, 40, and 80 mg/l) in the removal process was studied. The percentage of removal was calculated by using the following equation:

$$\boldsymbol{Dye\ removal}(\%) = \mathbf{100}[C_0\text{-}C(t)]_0 \qquad \textbf{(9)}$$

C_0 and C(t) represent the initial dye concentration and that at time t of the irradiation.

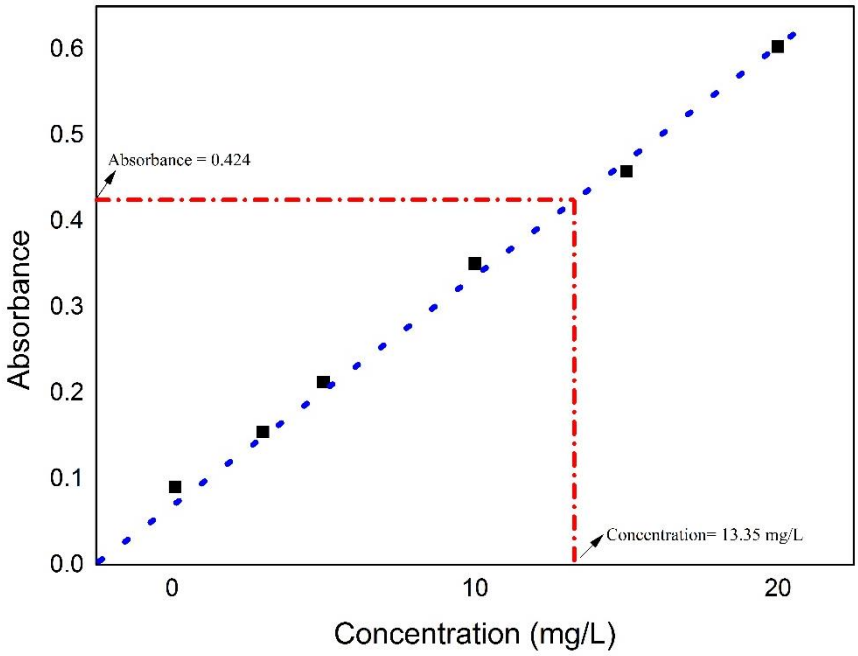

Fig. 2.19 Calibration curve- Absorbance Vs. Concentration

The calibration curve is required for the quantification of the contaminant based on the spectrophotometric analysis. The curve is drawn based on the concentration (in the X-axis) vs. its response (absorbance (in the Y-axis)). The Beer Lambert's law is used for the calculation of the concentration (**Eq. 5**). A linear adjustment was drawn between the two parameters (fig.2.18), such as **Abs= mc** with Abs is the absorbance, c the concentration (mg/l), and m is the fitted slope corresponding to the molar extinction coefficient from the Beer Lambert's law.

2.4.1 Kinetics of Photocatalytic reactions

Consider a chemical reaction schematically accounted by the following expression:

$$\textbf{Reactants (A)} = \textbf{Product (B)} \qquad (10)$$

The reaction rate constant (**k**) can be defined by considering the change in the concentration with time as follow:

$$d[A] = -k\,dt \qquad (11)$$

If we consider that initially at time, t=0, the concentration is $[A]=[A_0]$, it changes to [A](t) at time t. In the case of a first-order process for the time dependence of the reactant concentration is represented by;

$$[A](t) = [A_0].\exp(-kt) \qquad (12)$$

Also, by plotting the ln[A] versus the time, we may deduce the reaction rate constant (k) from the slope of the curve, as shown in fig.2.19.

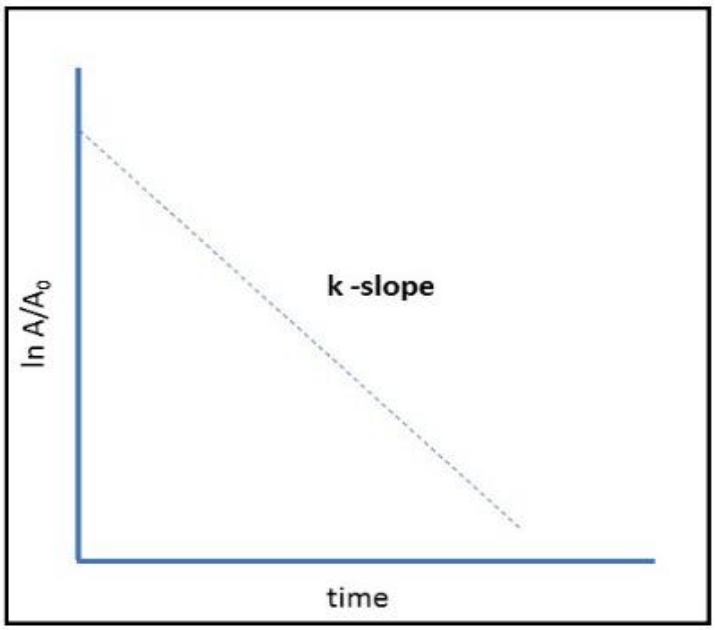

Fig.2.20 Plot of the reactant concentration versus time for a first-order process

In the case of the pc degradation of organic dyes in solution, the reaction rate constant can be calculated from the measurement of the absorption curve versus time, as discussed above. The same procedure is applicable for all the solutions have the absorbance response.

2.4.2 Photocatalytic arsenic removal- Quantification methodology

The pc As removal experiments were carried out similarly that of the organic dye-degradation experiments as mentioned in the section 2.4.1. However, in this case, the residual contaminant quantification was different; that is, the ammonium molybdate – colorimetric method was used for the complex formation in the aliquot samples to produce corresponding color and hence the spectral absorbance response.

During the pc process, the catalyst was mixed with the sample contaminant solution. And the aliquot sample was taken during certain intervals. The filtered aliquot solution has been taken into two sets (5ml each). One set is tested for As(III) and the other for the As total.

Into the 5ml sample solution, 100 µL of $KMnO_4$ was added (to find the presence of As(III)). Moreover, it was kept for 5 minutes. Furthermore, the other set was kept without $KMnO_4$. Then added 100 µL of ascorbic acid followed by 200 µL of ammonium molybdate solution. Then added 600 µL of water into it. The solution was kept under dark for 2 hours to allow

the complex formation. Depending on the As concentration in the sample, the solution took different intensities of the blue color. Finally, the sample solutions with complex formation have undergone the absorbance analysis. Moreover, the intensity of the absorption peak corresponding to the 871nm was measured. Since the formed complex has a chromophore group present with the absorbance around 871nm.

Furthermore, the residual As concentration during each interval is calculated using the absorbance value and making use of a calibration curve. And the quantification of the residual contaminant was done similar as that of the dyes, as mentioned in section 2.4.

References

[1] S. Sakka, "Sol–Gel Process and Applications," in *Handbook of Advanced Ceramics*, Elsevier, pp. 883–910,2013.

[2] C. Jeffrey Brinker, George W. Scherer. (2013 October 23). "Sol-Gel Science_ The Physics and Chemistry of Sol-Gel Processing," (1st ed.). Available: https://www.elsevier.com/books/sol-gel-science/brinker/978-0-08-057103-4

[3] V. I. Merupo et al., "High Energy Ball-Milling Synthesis of Nanostructured Ag-Doped and BiVO 4 -Based Photocatalysts," ChemistrySelect, vol. 1, no. 6, pp. 1278–1286, 2016.

[4] K. T. Drisya et al., "Electronic and optical competence of TiO2/BiVO4 nanocomposites in the photocatalytic processes," Sci. Rep., vol. 10, no. 1, p. 13507, 2020.

[5] G. Gouadec and P. Colomban, "Raman Spectroscopy of nanomaterials: How spectra relate to disorder, particle size and mechanical properties," *Prog. Cryst. Growth Charact. Mater.*, vol. 53, no. 1, pp. 1–56, Mar. 2007.

[6] K. Nakamoto and C. W. Brown, *Introductory Raman Spectroscopy*. Elsevier, 1994.

[7] T. G. Mayerhöfer, S. Pahlow, and J. Popp, "The Bouguer-Beer-Lambert Law: Shining Light on the Obscure," *ChemPhysChem*, vol. 21, no. 18, pp. 2029–2046, 2020.

[8] L. Reimer, H.Kohl, "Scanning Electron Microscopy, Physics of Image Formation," https://www.springer.com/gp/book/9783540639763

[9] M. Z. Baykara and U. D. Schwarz, Author ' s personal copy Atomic Force Microscopy : Methods and Applications, 3rd ed., vol. 1. Elsevier Ltd., 2017.

[10] D. Rugar and P. Hansma, "Atomic force microscopy," no. October, 1990.

[11] S. Y. Mendiola-Alvarez, M. A. Hernández-Ramírez, J. L. Guzmán-Mar, L. L. GarzTOvar, and L. Hinojosa-Reyes, "Phosphorous-doped TiO2 nanoparticles: synthesis, characterization, and visible photocatalytic evaluation on sulfamethazine degradation," Environ. Sci. Pollut. Res., vol. 26, no. 5, pp. 4180–4191, 2019.

[12] M. Naderi, "Surface Area," in *Progress in Filtration and Separation*, Elsevier, 2015, pp. 585–608.

[13] V. M. Bhandari and V. V Ranade, "Advanced Physico-chemical Methods of Treatment for Industrial Wastewaters," in *Industrial Wastewater Treatment, Recycling and Reuse*, Elsevier, pp. 81–140, 2014

CHAPTER. 3

Sol- gel synthesis and characterizations of TiO_2/ $BiVO_4$ nanocomposite powder

3.1 Optimization of synthesis method for TO/BVO nanocomposites

The BVO was synthesized by the sol- gel methodology as mentioned in the Chapter.2. For the incorporation of TO, many methods have been tried before optimizing the currently adapted synthesis method for obtaining the desired TO/BVO nanocomposites.

Different methods are discussed below;

Method.1 In the first trial, the sol-gel synthesized BVO was directly added during the gelation step while the synthesis of TO.

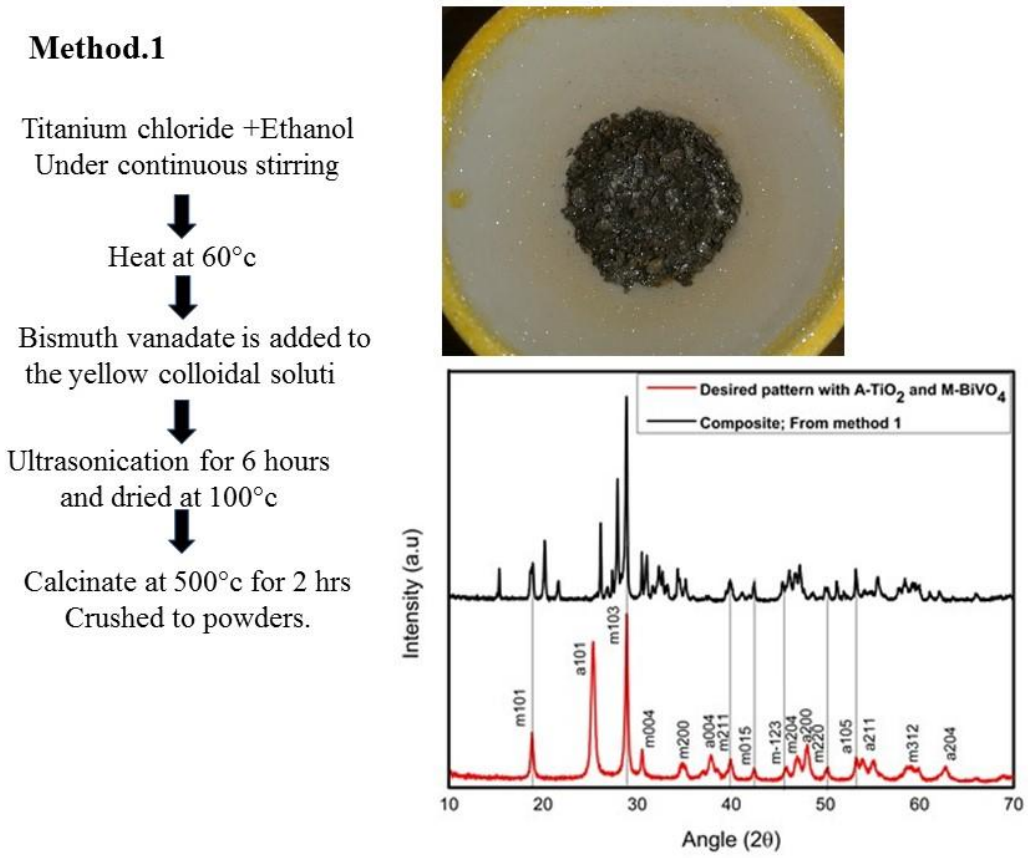

Fig. 3.1 Scheme of method.1tried for the synthesis of the nanocomposites with desired crystalline phases

The structural analysis of the final product obtained from method.1 as in fig. 3.1 was resulted in the presence of some un identified peaks that doesn't belong to the desired BVO and TO phases. And hence tried a second methodology for obtaining the desired phases.

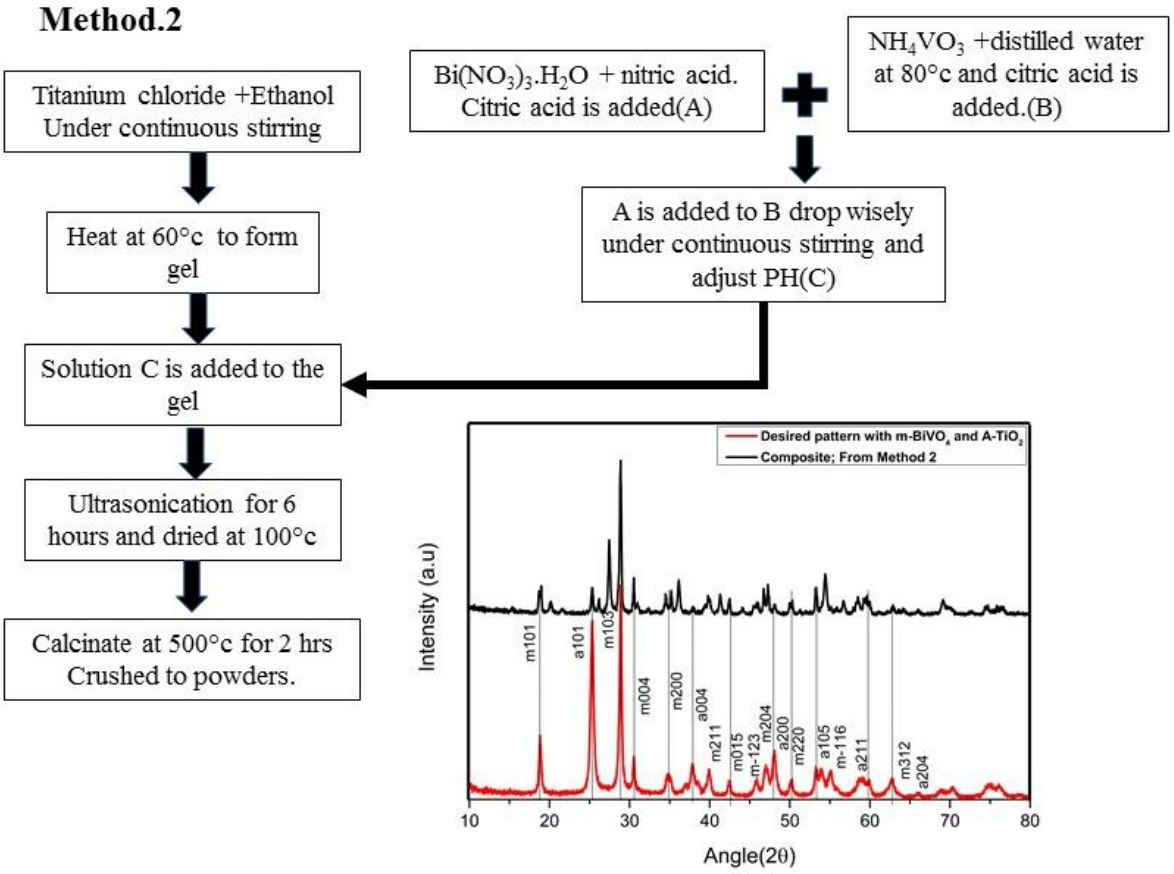

Fig. 3.2 Scheme of method.2 tried for the synthesis of the nanocomposites with desired crystalline phases

The Method.2, as in fig. 3.2 there started the sol gel synthesis of both BVO and TO separately. During the gelation steps of both materials mixed with each other. But this method also failed in obtaining the desired crystalline phases. Hence, we tried a third method as mentioned in the chapter.2, where we obtained the band gap engineered nanocomposites with desired phases and high crystallinity, in which we added the TO that purchased from sigma Aldrich directly to the BVO sol just before the gelation process.

3.2 X-Ray Diffraction analysis

Xrd patterns of the TO/ BVO nanocomposites before and after calcination are illustrated in fig. 3.3. The xrd patterns shows that, before calcination, an orthorhombic BVO phase was formed (fig. 3.3a). The xrd patterns in fig. 3.3b belong to the nanocomposites after calcination, compared with those of pure TO and sol-gel synthesized BVO. The xrd results

show that, after calcination of the samples, the orthorhombic phase of BVO was completely transformed into monoclinic BVO (JCPDS00-075-1866). Also, there exist TO (JCPDS 00-021-1272) along with BVO. The results matched with those already reported ones [1,2]. The diffraction peaks of nanocomposites (Set A) (0.2:0.8, 0.5:0.5, and 0.8:0.2) indicate the reflections related to the anatase structure, with the planes (101), (004), (200), (211), and (204) corresponding to the 2Θ values: 25.28, 37.80, 48.04, 55.06 and 62.68 º, respectively [3,4]. Concerning BVO, it is identified that, the planes (101), (103), (015) and (220) of m-BVO (JCPDS-00-075-1866), corresponding to the 2Θ values 18.67, 28.6, 42.49, and 50.33 º, respectively [5]. The different diffraction lines exhibit a high intensity and a narrow linewidth, indicative of good crystalline features.

Before and after calcination, all the samples show the characteristic peaks of TO, which is an evidence for the stability of the anatase TO structure. Before the calcination, the samples with the compositional ratios of 0.5:0.5 and 0.8:0.2 show the peaks of TO and those of an orthorhombic phase (PDF- 01- 075-1418). However, before the calcination, the 0.8:0.2 sample exhibits both an orthorhombic phase (PDF-01-086-0392) and monoclinic BVO phase, confirming the fact that at lower temperatures, there exists the formation of other phases besides the monoclinic one [6]. It can be observed that, before the calcination, the 0.2:0.8 sample shows the intense peaks that correspond to the orthorhombic phase of BVO, whereas, after calcination, as shown in fig. 3.3b there is a dramatic decrease in the signal of m- BVO. Concerning the samples that were calcinated at 500 ºC, pure m- BVO was stabilized. This could be attributed to the difference in TO present in the nanocomposite compared to that of BVO.

Before the calcination process, the estimated crystallite size values establish no correlation concerning the compositional ratios of the samples (10.83, 16.56, and 29.06 nm for the 0.8:0.2, 0.5:0.5, and 0.2:0.8, respectively); this effect suggests that the nanoparticles with the orthorhombic BVO structure, were sintered and grown during the phase transition, into a monoclinic form [7].

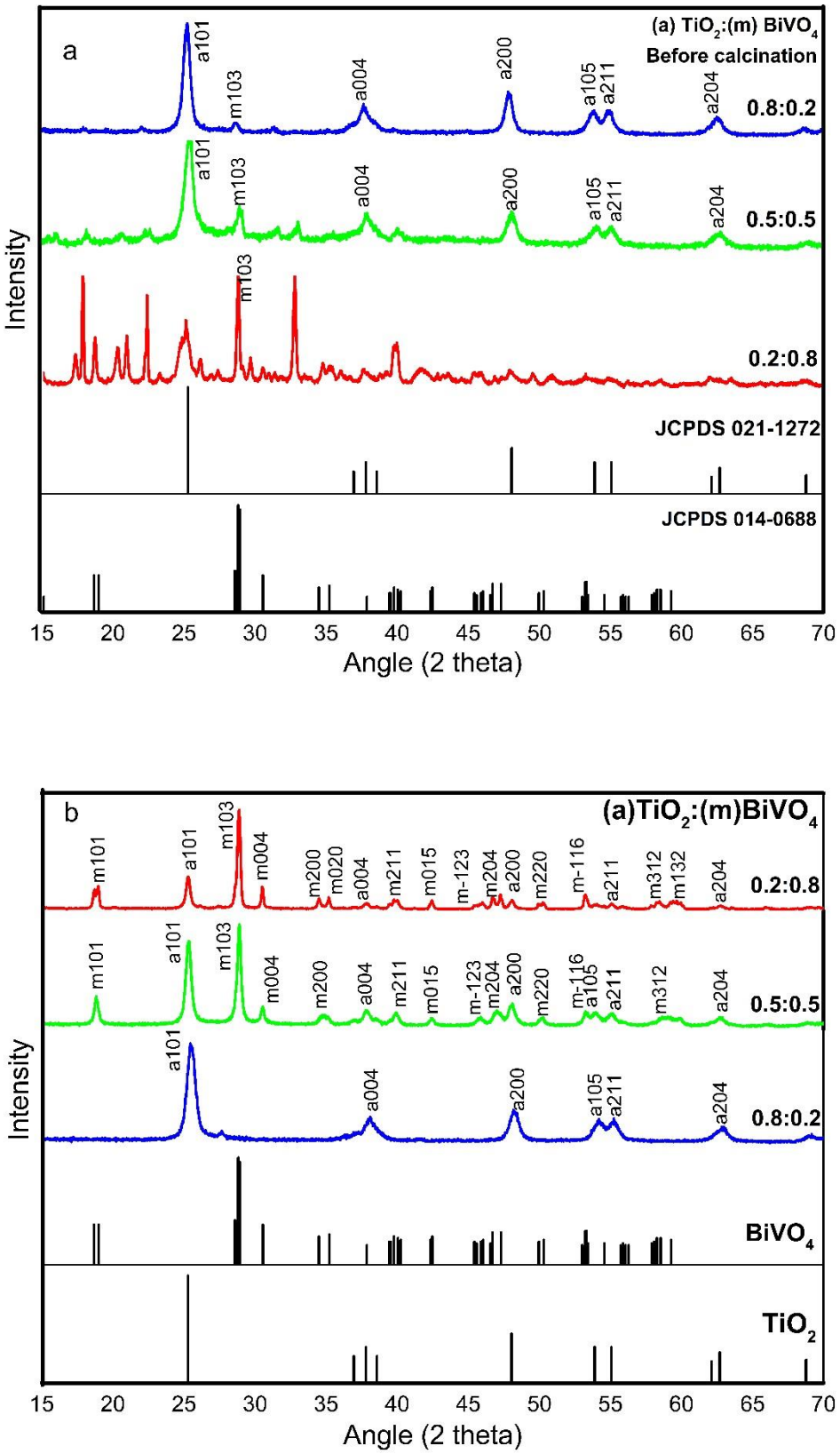

Fig. 3.3 Xrd patterns of the nanocomposites a) before and b) after calcination (500°C), compared with those of pure TO (JCPDS 00-021-1272) and sol-gel synthesized BVO (JCPDS-00-075-1866). Before the

calcination of the samples, the refinement of the patterns shows the formation of the orthorhombic phase of BVO.

Table 3.1. Calculated crystal properties of the nanocomposite after calcination

Sample T/B	**2 theta (Degrees)**	**FWHM**	**The crystallite size (nm)**	**Dislocation density*(10^{-3}) m^{-2}**
0.8:0.2	25.522	0.752	10.83	8.53
0.5:0.5	25.332	0.491	16.56	3.64
0.2:0.8	25.305	0.280	29.06	1.18

The crystallite size (D) has been calculated for each film by taking the average of all the peaks using the Debye- Scherer formula [8];

$$\boldsymbol{D = \frac{0.9\lambda}{\beta Cos\theta}} \qquad (1)$$

For the dislocation density, we used the following formula:

$$\boldsymbol{\delta = \frac{1}{D^2}} \qquad (2)$$

The crystallite size of the nanocomposites was calculated (Table. 3.1) after calcination. It is observed that there seems a decrease in the crystallite size with the decreased stoichiometry of BVO considering its higher atomic radius. Moreover, the decreased crystallite size also can lead to an increase in the number of crystallites per unit area of the material.

3.3 Raman analysis

The Raman spectra of the nanocomposite samples with different TO/ BVO ratios are shown in fig. 3.4. Among the raman active modes, the peaks at 158cm^{-1} and 523.3cm^{-1} are assigned to the Eg (147 cm^{-1}) and A1g (519cm^{-1}) modes, respectively, along with a 645.9 cm^{-1}(640cm^{-1}) signal, all from TO [3,9]. On the other hand, the bands located at 346, 375, and 846 cm^{-1} closely match with the reference by Thalluri et al. corresponding to the BVO (340,375 and 830.4 cm^{-1}) [10,11].

From the set of signals, both 325 and 367cm^{-1} correspond to the bending modes of the VO_4 groups; meanwhile, the peak at 830.4 cm^{-1} is attributed to the symmetric stretching of the V-

O bond within BVO [11,12, 5]. Finally, the raman mode at 154.8 cm^{-1} has a remarkable inconsistency; for the 0.2:0.8 sample, its small intensity can be attributed to a lower content of TO, whereas a slightly intense signal from the 0.8:0.2 ratio is due to its high TO content. The raman mode at 154.8 $cm^{-1,}$ which corresponds to the O-T-O bending vibrations [13], has an inconsistent change, for the 0.2:0.8 ratio, the smaller peak can be attributed to the lower content of TO, and that of 0.8:0.2 is a little more intense where there is high TO content. However, in the case of 0.5:0.5, the raman band shows a high intensity, which could be due to the effect from the BVO.

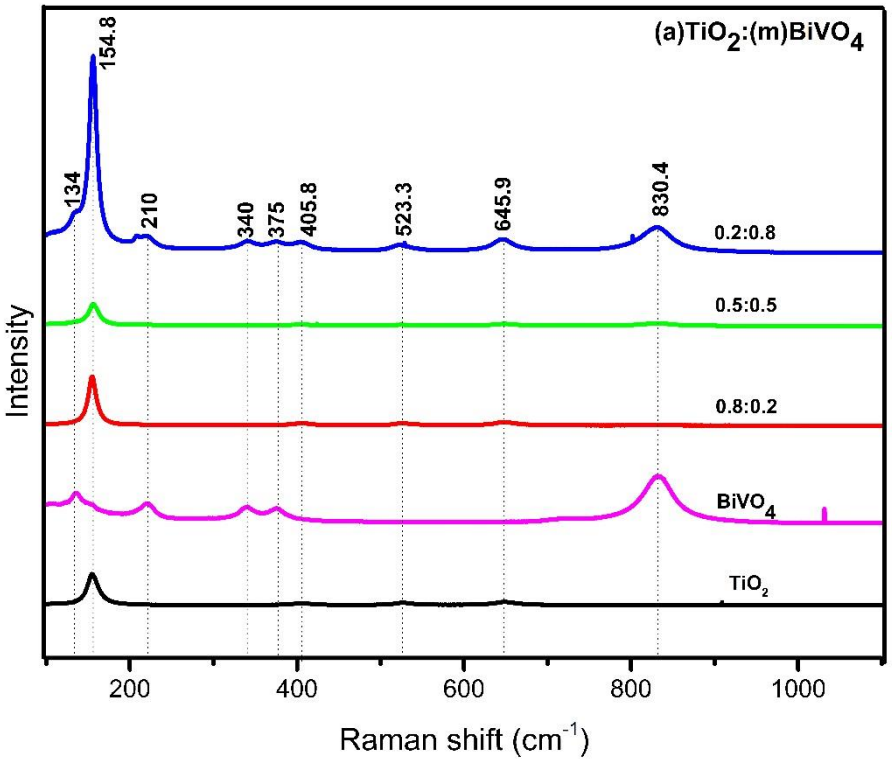

Fig. 3.4 Raman spectra for nanocomposite samples (The raman measurements show noticeable changes as a function of the composition proportion of TO/BVO.)

3.4 Scanning Electron Microscope (SEM) analysis

Surface morphological analysis (fig. 3.5) was carried out for TO/ BVO nanocomposites samples before and after calcination, which illustrates the morphology of the particles. Non calcinated samples show agglomerations with barely recognizable boundaries among particles, an image that changes with well-defined boundaries after the calcination process (fig. 3.5), in agreement with a similar phenomenon observed for titanate nanotubes at T>400[14], associated with the coalescence of the particles during the calcination process

[15]. Similar morphology was reported by Rahimi et al. for a BVO:TO nanocomposite sample calcinated at 450℃ [16]. The average particle size for the nanocomposite samples after calcination, ratios 0.8:0.2, 0.5:0.5, 0.2:0.8 were having the particle sizes 44, 36 and 43 nm, respectively. Before calcination, the obtained particle size was 39, 37, and 63nm respectively. There observed no significant difference in the particle size with the change of stoichiometry from (TO: BVO) = 0.8:0.2 to 0.5:0.5. But there is a large difference in the particle size of the composite with 0.2:0.8.

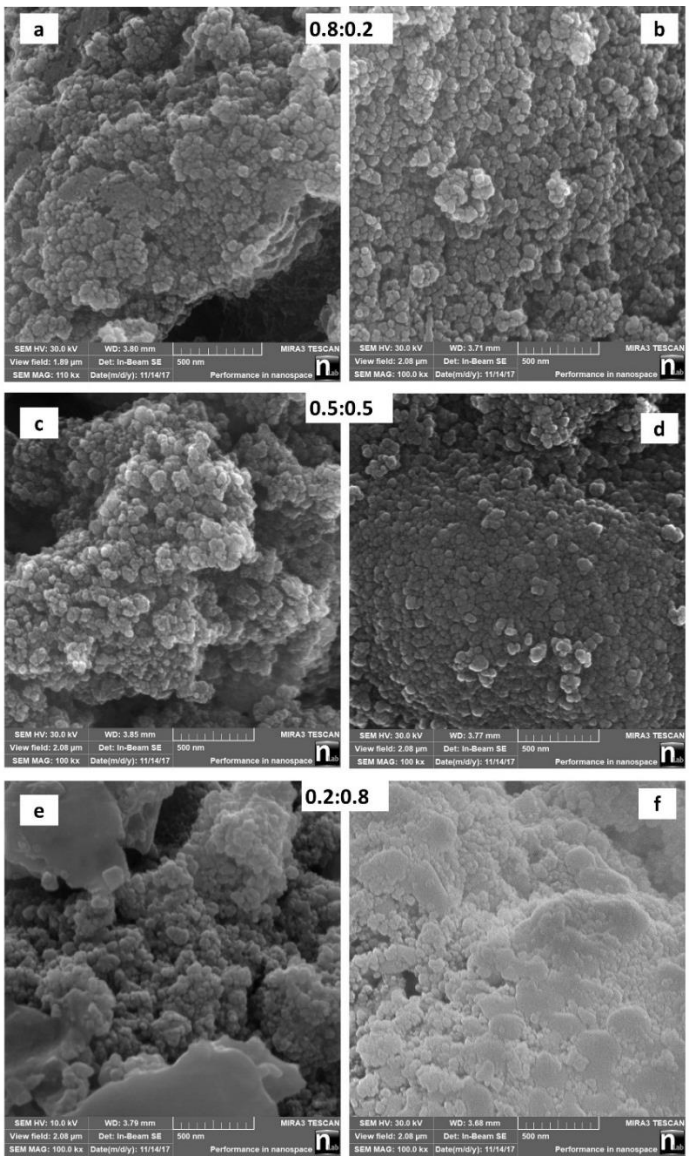

Fig. 3.5 SEM images of the samples before and after calcination 0.8:0.2, 0.5:0.5 and 0.2:0.8 - a,c,e) before calcination b,d,f) after calcination respectively.

3.5 UV- Visible Bandgap analysis

Fig. 3.6 illustrates the calculated bandgap of various nanocomposites and pure BVO and TO. The optical band gap values were calculated using the following equation [17] and the Tauc Plot is in the inset of the Fig.3.6:

$$E_g = {1240}/{\lambda_g} \qquad (3)$$

The observed bandgap value for BVO was 2.34 eV, and that of pure TO was 3.2 eV, in agreement with previous studies [18,19]. The absorption range of the nanocomposites lies in between the values of pure TO and that of BVO [20]. For all the nanocomposites with different ratios (0.2:0.8, 0.5:0.5, 0.8:0.2), we observed the shift in the bandgap values for the nanocomposites [21]. In the nanocomposite with high TO content, the nanocomposite bandgap was shifting towards the value of pure anatase. Contrarily, there observed redshift towards the visible light range when the fraction of BVO was higher. This redshift is normally required for the efficient pc reactions. The observed band gaps for the synthesized ratios are summarized in table.3.2. In the case of nanocomposites, each energy level may have 'n' different energy levels, which is equal to the number of atoms interacting with each other. So, in the case of nanocomposites, these bands may overlap and hence reduces the overall bandgap [22,23,24]

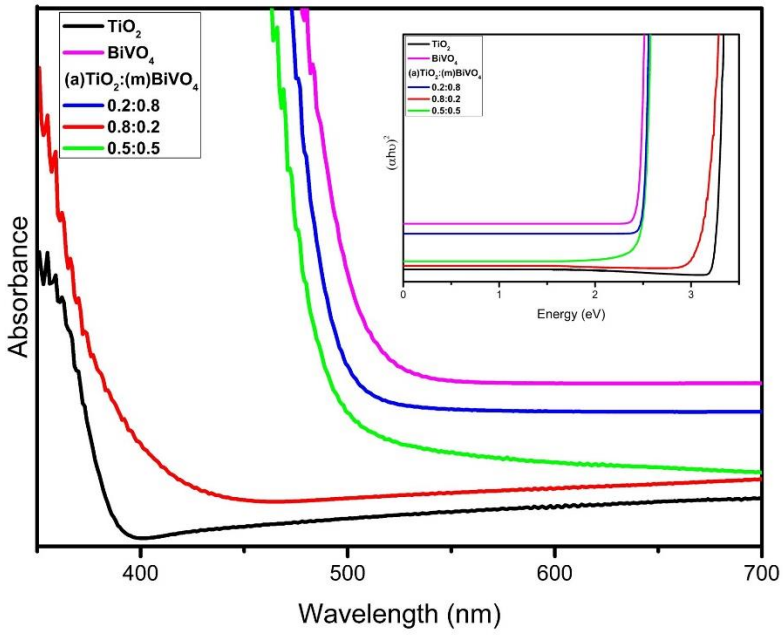

Fig. 3.6 Comparison of the bandgap energy of the synthesized nanocomposite samples with TO and synthesized m- BVO nanoparticles with the tauc plot in the inset.

Table 3.2 Calculated band gaps of BVO, TO, and its various nanocomposites

Material	Bandgap(eV)
BVO	2.34
TO	3.20
0.8:0.2	2.96
0.5:0.5	2.43
0.2:0.8	2.42

3.6 Transmission electron microscope (TEM) analysis

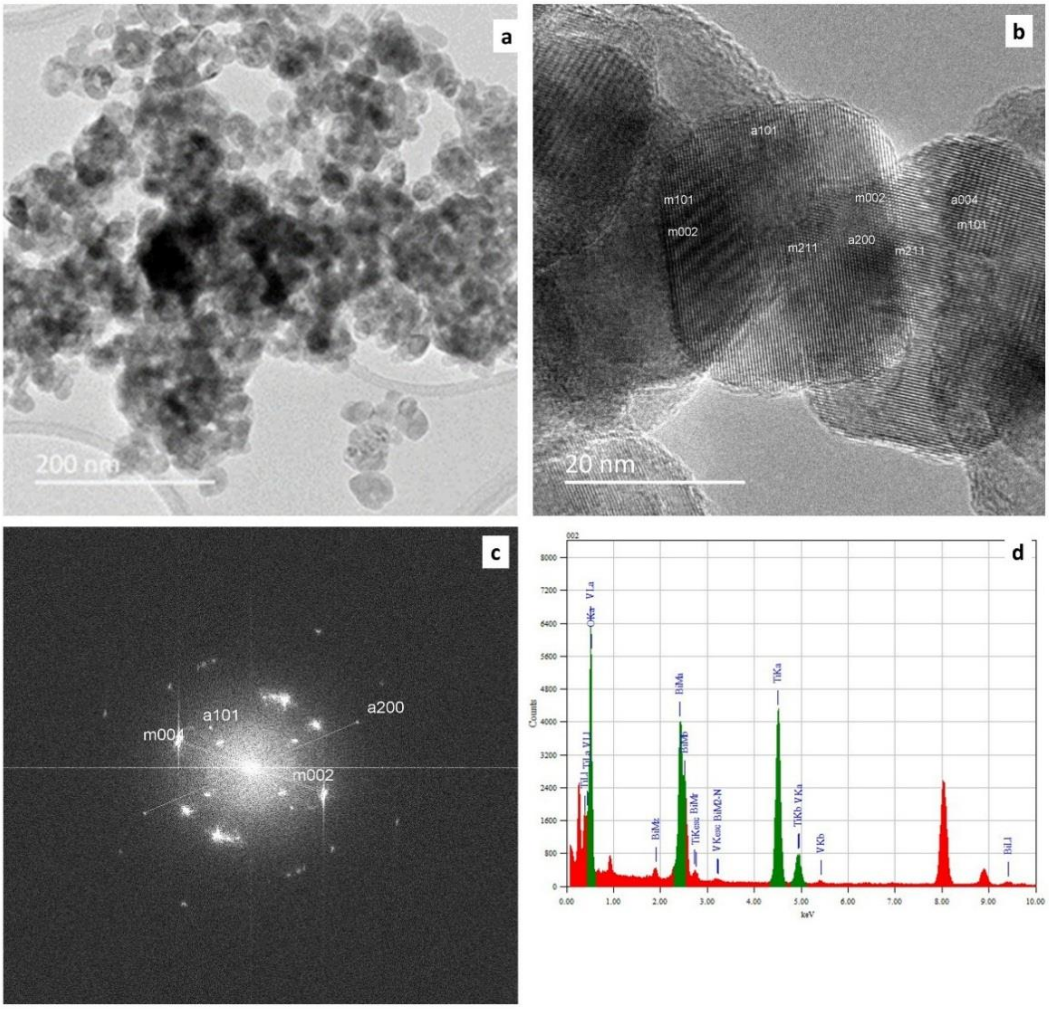

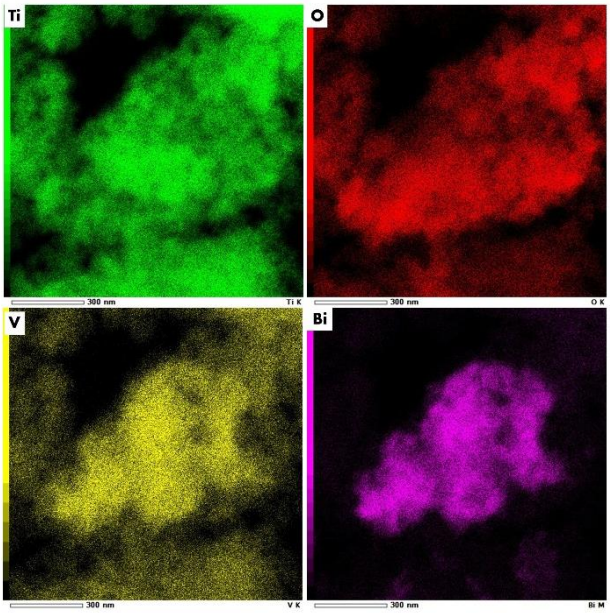

e

Fig. 3.7A Micrographs of the 0.8:0.2 nanocomposite a) TEM micrograph of the whole area b) Selected area from the sample c) FFT diffraction pattern d) EDS chemical analysis e) Mapping of the samples.

The transmission electron micrographs of the nanocomposites are illustrated in fig. 3.7(A, B, and C). The morphology of the particles is similar to the spherical nature obtained from scanning electron microscopy (fig. 3.7). The grains of the composite material indicate the formation of heterojunctions associating with TO and BVO planes. All the reported micrographs show superimposed structures from TO and BVO compounds, as clearly seen in EDS analysis performed on the different samples to identify the presence and amount of the component elements [25] (fig. 3.7A-e and fig. 3.7B-c). In the dark and bright-field images, it is possible to see the different atomic mass contrasts (or Z contrast) involved in composites grains, and even though, in some instances, the contrast difference can result from the difference in the grain thickness. FFT helps in plane indexing [26]. From fig. 3.7A -a, the presence of the planes with different orientations can be seen. Fig. 3.7A -b, the EDS analysis confirms the presence of all the elements in the composite. In fig. 3.7A -c, FFT diffractions patterns, the planes (101), and (200) corresponding to the anatase phase of TO and (002) [27] corresponding to the diffractions from the m- BVO system can be seen. Fig. 3.7B -a shows a high-resolution image of sample 0.5:0.5 where the crystallographic planes are identified, and agree with the desired monoclinic and anatase phases (Fig. 3.7B -d). Fig. 3.7B -d is the FFT for the sample 0.5:0.5, and there observed diffraction from the planes (103) from the monoclinic and the (101) corresponding to the anatase phase. fig. 3.7B -b and fig. 3.7B -c is the bright and dark

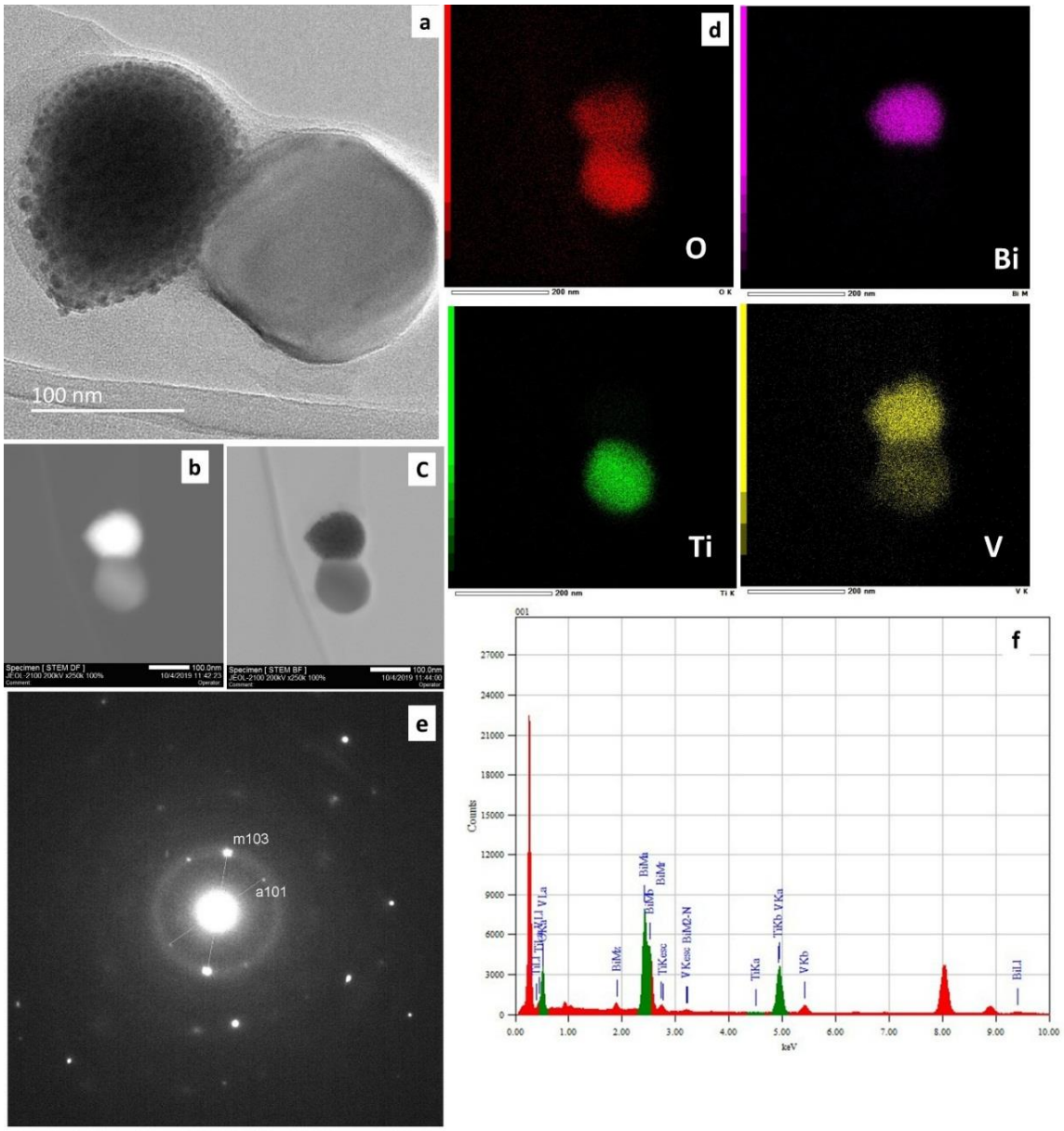

Fig. 3.7B Micrographs of the 0.5:0.5 nanocomposite a) TEM micrograph of isolated particles b,c) bright and dark field analysis d) Mapping analysis of sample e) FFT diffraction pattern f) elemental mapping and f)EDS analysis, respectively

field micrographs where the atomic mass contrast is visible, and fig. 3.7B -e is the mapping analysis of the sample where the presence of each element is identified by the EDS (fig. 3.7B -f). Fig. 3.7C -a is the TEM micrograph of samples 0.2:0.8, and fig. 3.7C -b is the EDS chemical analysis of the samples in which all Bi, Ti, O, and V elements can be identified. Fig. 3.7C -d and fig. 3.7C -e are the bright and dark field images with the Z contrast, and corresponding chemical composition can be identified from the mapping analysis fig. 3.7C -c, provides the evidence of the mixed composition from BVO and TO with a wide area of

heterojunctions. This organization is expected to favor the photo-induced charge transfer process between the coexisting structures. All the planes observed in the TEM FFT pattern are in good agreement with peaks observed in the X-ray diffractogram (fig. 3.3).

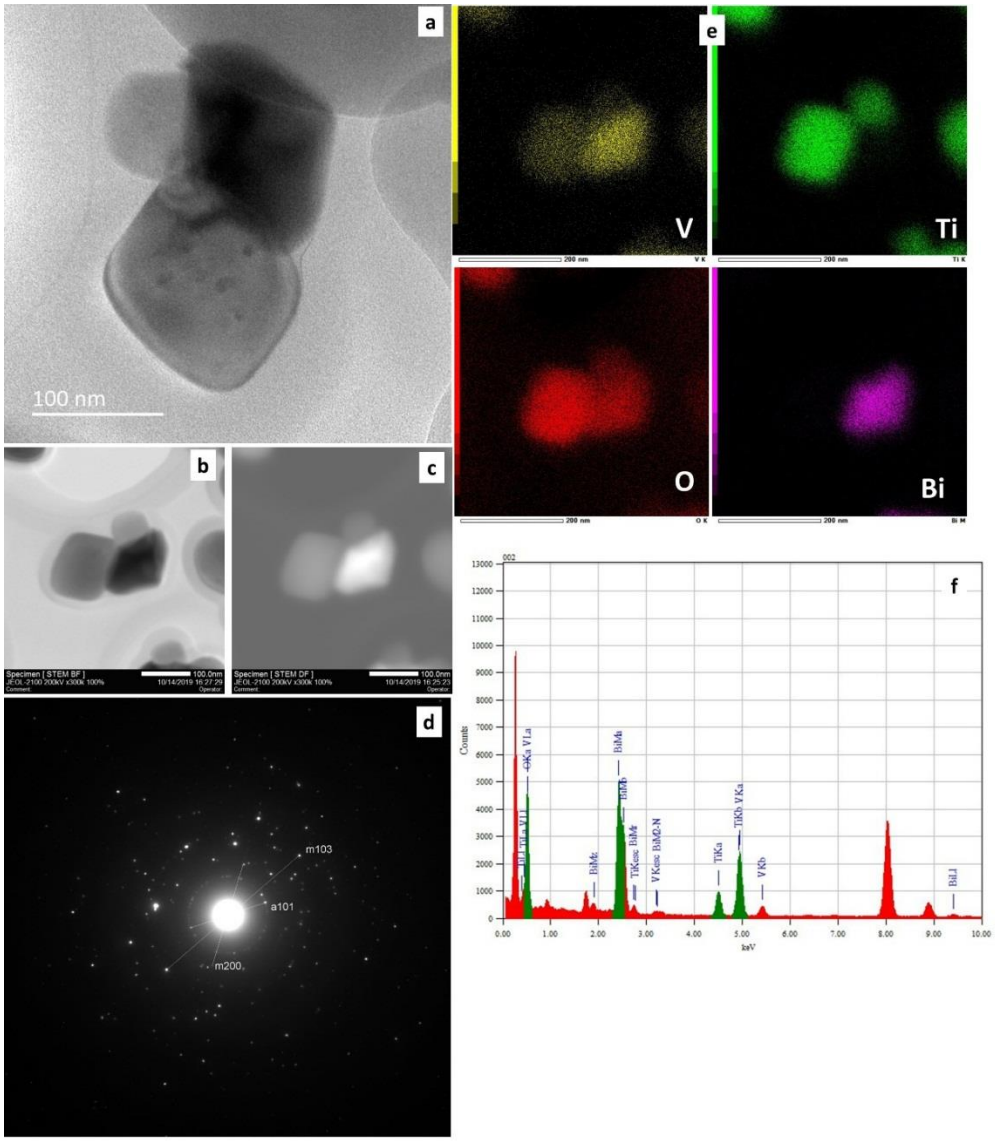

Fig. 3.7C Micrograph of the nanocomposite 0.2:0.8 a) isolated particles b) bright-field image c) dark field image d) FFT diffraction pattern e) elemental mapping of the nanocomposite f) EDS analysis of the nanocomposite.

Similarly, in the diffraction images for the sample 0.2:0.8 (fig. 3.7C -f), we observed significant diffractions from the monoclinic (103) and anatase (101). The plane (101) from the anatase corresponding to the angle 25.28º is observed in all the samples, which are the significant planes. Moreover, the significant one for the monoclinic phase is the (103) at an angle of 28.6 º. In the stoichiometry 0.8:0.2, the significant (103) plane is not visible in the

diffraction image of the sample, and the same character is observed from the xrd of the sample, which is attributed to the low composition of the BVO. The planes were identified using the standard JCPDS files used for the xrd analysis (BVO); JCPDS-00-075-1866 and TO; JCPDS-00-021-1272) [1]. In all cases, the EDS and mapping (each element are identified inside the image) confirm the presence of both phases.

Furthermore, the synthesized materials have shown good crystallinity. The grain size from the TEM micrographs are found to be 94.82, 75, and 31.77nms, corresponding to the 0.2:0.8, 0.5:0.5, and 0.8:0.2 samples, respectively. The observed large difference between the crystallite size obtained from the Scherrer calculations can be due to the incorporation of BVO. It can be seen that as BVO content increases, the crystallite size also increased in the nanocomposites. This could be due to the higher atomic radius of BVOA similar tendency can be seen from the large particles depicted by the SEM micrographs.

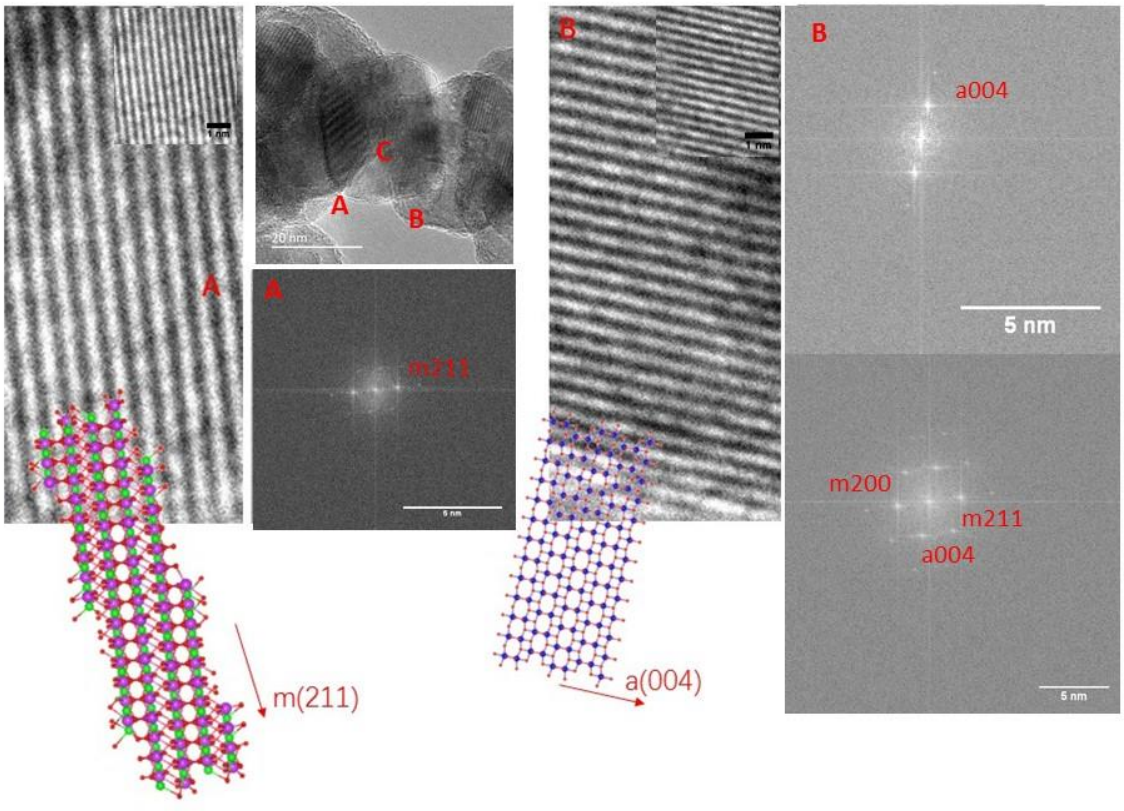

Fig. 3.8 TEM micrograph, FFT planes, and simulated crystalline models for the 0.8:0.2 composite. Regions A, B, and C correspond to pure BVO, TO, and the junction of both crystalline phases, respectively.

The clear distribution of the atomic planes, shown in the TEM image of the 0.8:0.2 composite, allows the mapping of the crystalline phases in each grain. In fig. 3.8, three highlighted spatial regions with both pristine m- BVO and TO, in regions A and B, respectively. In the former case, the simulated FFT pattern shows a single plane spacing, associated with (211) of BVO equal to 2.26 Å, reported for BVO composites [28]. Meanwhile, the associated (004) plane distance is found over the pristine TO, equal to 2.29 Å, as reported in anatase based nanocomposites [29].

The simulated crystalline structures generated by the BIOVIA Materials Studio Package show the monoclinic clinobisvanite (space group number 88; I2b) with a cleavage over the (211) plane, from the conventional unit cell containing four Bi, four V, and eight O atoms. The stacking of the (211) planes grows along a perpendicular direction to the plane defined by the vectors U [1 -2 1] and V [0 1 -1], with a unitary thickness equal to 2.261 Å, which is in excellent agreement with the graphically determined distance. On the other hand, the anatase phase of TO (space group number 141; I41amd) shows a stacking of (001) planes, parallel to the c lattice parameter of anatase, with an equivalent thickness equal to 2.372 Å, in agreement with the value determined by the FFT calculation. As a graphical aid, both slab models are superimposed to their respective pristine regions of the TEM image. The slab model of the m(211) planes show empty channels surrounded by vanadium and bismuth atoms that match the brightest signals from region A[28].

Meanwhile, the lighter areas in the TEM image from region B could be assigned to the rings of Ti atoms along [100] and [010] directions. Such agreements support the association of the atomic plane distance to the crystalline phase at the pristine regions. However, in the portion indicated as C region, the calculated plane distance in the FFT patterns evidence the junction formation since the characteristic planes from both crystalline phases appear together, as it was reported in bimetallic layered double hydroxides with MoS_2 in a stacking array [30] as well as in core-shell nanoparticles composed by PdO/ZnO [31], where the presence of the interplane distances from the constituents in TEM images reveal the formation of effective coverages and an interface.

3.7 Photocatalytic degradation tests using Acid blue 113 (AB113) as a model organic pollutant

The pc studies were conducted using the three ratios of the TO, BVO, and TO/ BVO nanocomposites (0.8:0.2, 0.5:0.5, and 0.2:0.8). Initially, we kept the dye concentration at

40mg/l and the nanocomposite concentration at 1g/l, with the pH fixed at 6 throughout the experiment. In these conditions, the 0.8:0.2 sample demonstrated the highest rate removal of AB113 (82%) after two hours of visible-irradiation. The sol-gel synthesized BVO exhibited comparatively poor activity. Similar results were reported by Longo et al. [32], who synthesized TO/ BVO nanocomposites using the hydrothermal method. They observed that the activity of the substance was directly proportional to the total amount of the used TO. This behavior can also be attributed to the low activity of BVO derived from its small specific surface area, 52, 56, and 44 m^2/g for nanocomposites ratios 0.8:0.2, 0.5:0.5, and 0.2:0.8, respectively. The particle seemed to have formation of junction like structures and this morphology influences the density of photo-generated charge carriers [32] due to the lowering of recombination process. The ratio 0.8:0.2 was selected to conduct the dye removal by pc reactions since this compound showed the best results with the lowest concentration of the nanocomposite material. According to fig. 3.9a, as the nanocomposite dosage increases, the removal rate increases as well, so when a catalyst dosage of 5 g/l has reached the concentration of AB113 is below the detection limit that is nearly a complete degradation occurred. The increase in the total amount of the catalyst increases the number of active sites on the nanocomposite surface, which, in turn, increases the generation of •OH radicals and hence the AB113 removal. This behavior was observed by other authors as well [33]. Fig. 3.10 shows the images of the contaminant solution after the pc degradation tests using each nanocomposite samples.

The observed adsorption was lesser compared to the pc degradation, and also, there is no self-degradation of the dye (fig. 3.9a). Therefore, AB113 dyes removal can be attributed exclusively due to the pc process using the nanocomposites compared to the performance of TO in the pc process. Comparing with the performance of TO in the pc process, the results show that there is a removal of 58.5 to 76.4%, which is attributed to the adsorption by TO particles.

Concerning the effects of the initial concentration of AB113, the investigations show that dye concentration from 20 to 40 mg/l was completely removed. However, when the concentration was doubled (80mg/l), we observed a decrease in the pc efficiency. The removal depends on both the dye concentration and the nanocomposite dosage. With a dye concentration of 40mg/l and a nanocomposite concentration of 5g/l, we observed the maximum percentage of dye degradation, 98.75%, after 10 minutes of visible light irradiation and within 20 minutes there observed a complete degradation as in fig. 3.9b. With

a higher dye concentration, the active sites required for the •OH production seemed to be insufficient, hence it becomes necessary to increase the photocatalyst dose.

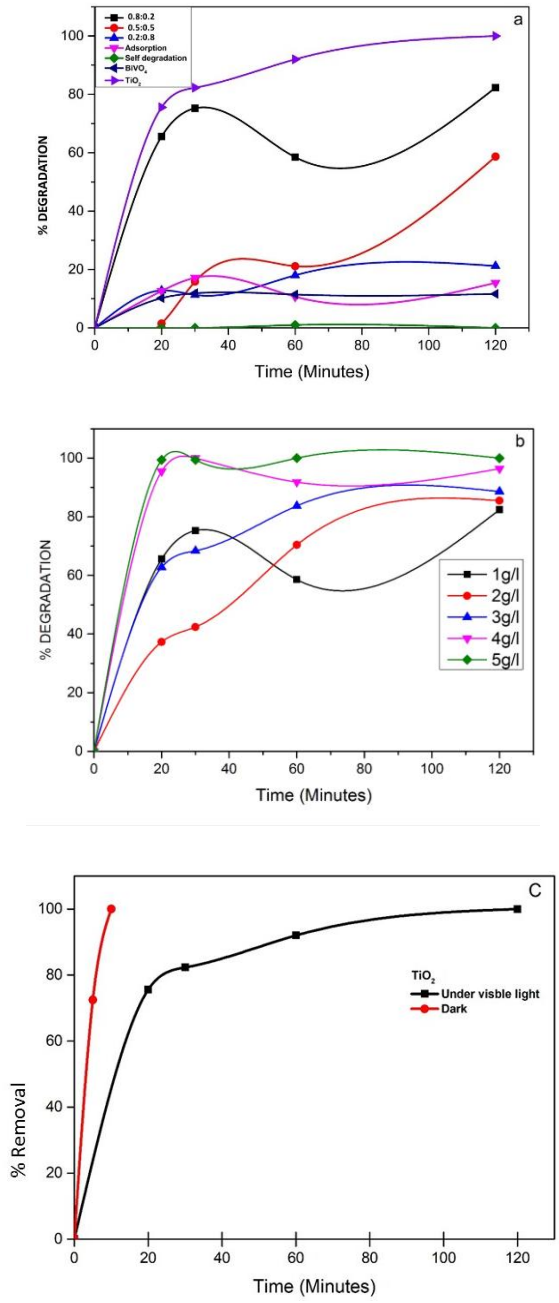

Fig. 3.9 Pc degradation of AB113 measured for wavelength of 568 nm(a) Adsorption and self-degradation plots along with the comparison of pc activity of TO, BVO and the three nanocomposite ratios $[AB113]_0$= 40 mg/l, [nanocomposite, TO, BVO] = 1g/l pH_0=6. (b) $[AB113]_0$= 40 mg/l, [nanocomposite]= 1-5g/l pH_0=6 (c) Comparison of the activity of TO (Both adsorption and photocatalysis)

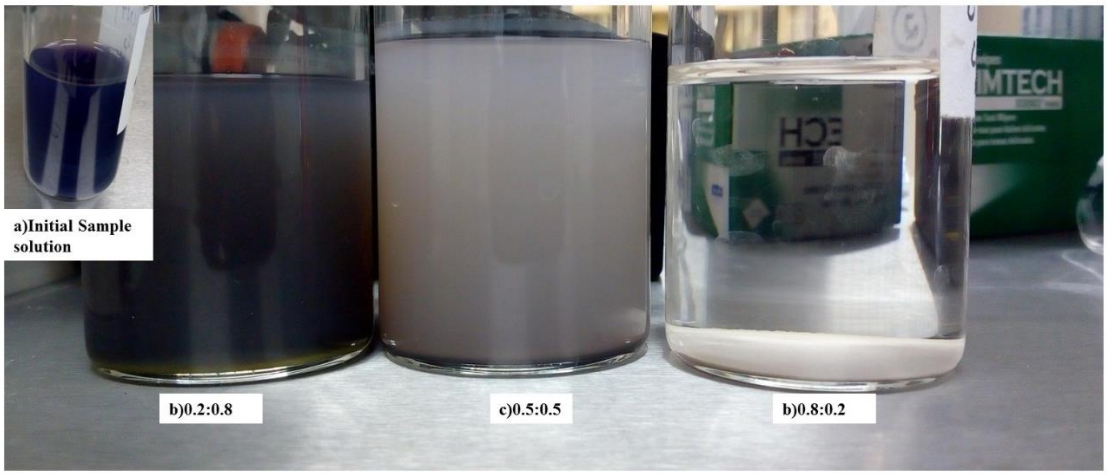

Fig. 3.10 The preliminary AB113 degradation test by each sample [Dosage] = 1g/l [C_0] = 40mg/l

The reaction constant was determined from the corresponding kinetic plot from the reaction, which follows pseudo-first-order kinetics [15].

$$\ln C_t/C_0 = k\_obs \text{ [34]}$$

C_0 and C_t are the initial and concentrations at time 't' of the AB113 dye molecules for a reaction time t. None of the sol-gel prepared nanocomposites surpasses the activity obtained with the TO under the used conditions. It can be inferred that the order for the photodegradation rate is: 0.8:0.2> 0.5:0.5≈ 0.2:0.8. The crystallite seems to play important role in the higher activity of the 0.8:0.2 composite. Lower crystallite size indicates a greater number of crystallites per unit area and hence provides a greater number of electrons per unit area that may results in higher efficiency [35]. Moreover, the degradation observed by the TO is completely due to the adsorption process (fig. 3.9c). The nanocomposite with a low relative amount of BVO appears as a more interesting candidate for pc reactions under visible light; similar results were reported by Longo et al. [32]. For BVO to act as a TO sensitizer, Longo et al. suggested that good contact between both phases is necessary to ensure a high interface is required for efficient charge transfer between both components.

The absorbance peak around 568nm represents the chromophore group present in the AB113 azo dye. Hence, the quantification of the degradation percentage can be done by measuring the intensity of this absorbance peak value. It is reported that the hydroxyl ions are identified with good effect over the organic contaminants [24]. Previous reports say that the discoloration is happening due to the formation of 1-naphthalenol and dibutyl phthalate as by-products during the dye degradation. 1-naphthalenol is produced by the direct attack of the hydroxyl radicals on the azo group. In contrast, the dibutyl phthalate is formed by the effective attack of the hydroxyl radicals over the aromatic rings of the naphthalene. Both the

aromatic by-products did not absorb along the visible spectrum, and this can back the fact that the dye molecule has degraded and decolorized during the pc reaction [36].

3.8 Electrochemical properties of the TO/ BVO nanocomposite material

The electrochemical interaction between BVO and TO can change the properties of TO/ BVO nanocomposites and their charge transfer process. Thus, to obtain more detail about the interface of the materials, electrochemical impedance spectroscopy is an excellent tool [26].

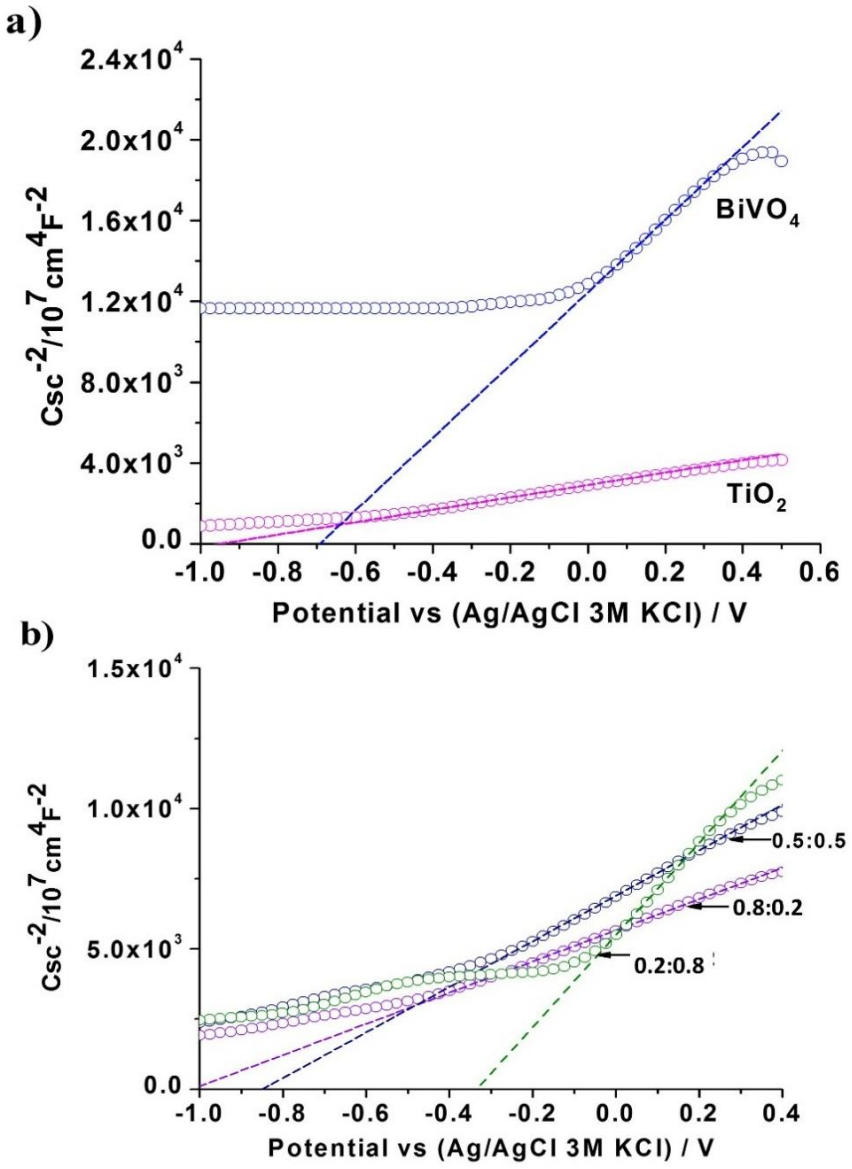

Fig. 3.11 Mott–Schottky curves of (a) BVO and TO and (b) TO/ BVO nanocomposites (0.8:0.2, 0.5:0.5, and 0.2:0.8) compositional ratio BVO: TO). The C_{sc} were obtained at 100 Hz in 0.05 M $NaClO_4$ aqueous solution.

Table 3.3. Flat band potential of synthesized nanocomposite powder materials.

Materials	E_{fb} vs (Ag/AgCl/3 M KCl) (V)
TO	-0.95
0.8:0.2	-1.01
0.5:0.5	-0.84
0.2:0.8	-0.33
BVO	-0.69

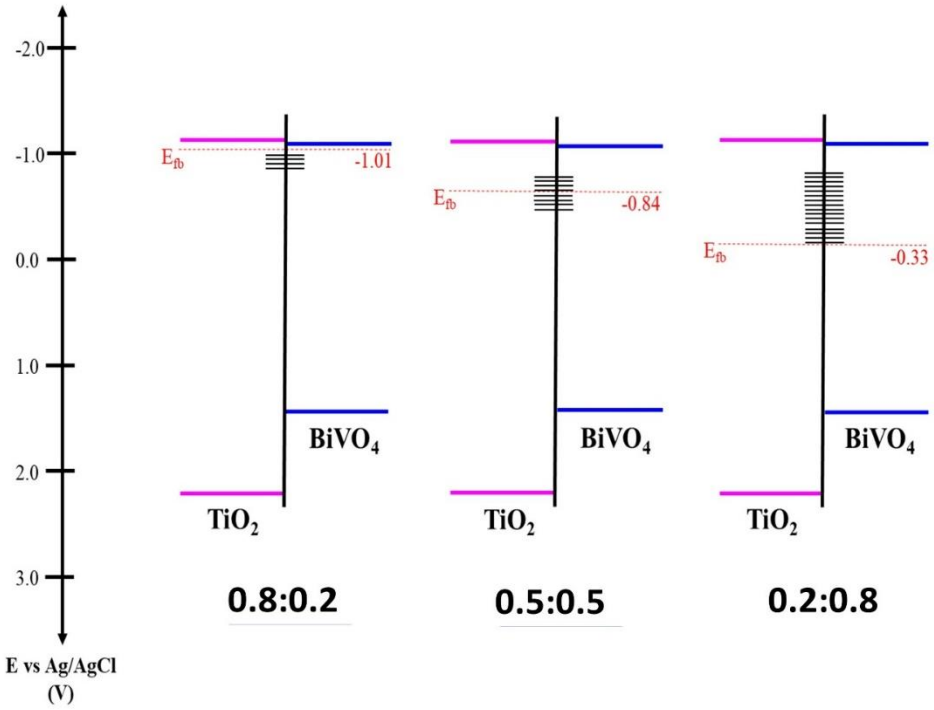

Fig. 3.12 Energy diagram proposed for TO/ BVO nanocomposites (0.8:0.2, 0.5:0.5 and 0.2:0.8 compositional ratio)

The semiconducting properties of the materials were based on electrochemical impedance spectroscopy and the flat band potential appearing as the x-intercept of the linear portion of a Mott−Schottky curve (table 3.3), the response of the materials correspond to n-type semiconductors (fig. 3.11). The interorbital overlap or the electronic connection between the two systems is defined and explained with Mott- Schottky curves. The light irradiation can generate the electron-hole pairs. Depending on the density of charge carriers, a positive and

negative charged region is created, forming an interface that is supposed to be due to the Schottky effect [37]. The Mott-Schottky curve is plotted (fig. 3.12) with capacitance vs applied potential [38]. Intercepts of these curves provide the flat band potential. Moreover, the slope of the curves gives the donor or acceptor intensity depending on the type of the semiconductor (p or n-type) since the slope will be positive for the n-type semiconductors and negative for the p-type semiconductors [22]. A decrease in the slope indicates an increase in the donor density. The shift of the intercept towards a positive value (fig. 3.11) indicates an increase in the flat band potential [23]. The flat band potential is the applied voltage when there is no band bending or depletion of the charge [24].

Flat band potentials and optical bandgap energies, fig. 3.13 shows the energy diagram proposed by coupling the BVO and TO. The value of E_{fb} for TO was -0.95 V; this value is more negative than the one reported in other works [39]. However, it can be associated with the defects in the material influenced by the synthesis techniques. On the other hand, the E_{fb} for BVO was -0.69 V. This value is close to a previous report [40]. For the TO/ BVO nanocomposite, two different trends have been observed. First, in the nanocomposite with the lowest BVO content (0.8:0.2), E_{fb} was displaced toward a more negative value than the pristine materials (-1.01 V). This behavior is related to the formation of surface states at the TO-BVO heterojunction interface as it was also reported in other composite materials as ZrO_2/TO, SnO_2/TO, and WO_3/BVO [41, 42, 43]. It has been observed that there is an increase in the photocurrent, along with the increase in the applied potential. Hong. et al. [39] reported that this behavior is unique for n-type semiconductors. An increase in the photocurrent increases the charge separation efficiency of the material [44]. In TO/ BVO nanocomposites (0.5:0.5 and 0.2:0.8), a displacement of E_{fb} toward the lowest negative values was associated with the high BVO content and the flat band alignment between BVO and TO (E_{fb} can provide information on the band positions of the semiconductor) [44]. Based on the values, to evaluate the stability of the photo-generated carriers, open circuit potential (OCP) measurements under the illumination of the synthesized materials were performed using visible light irradiation through 5 consecutive on-off cycles, previously bubbled with argon (fig. 3.13). When the materials were irradiated, the OCP change toward more negative values confirming that the materials are n-type semiconductors, and supporting the observations from the Mott-Schottky plots, that is an increased photocurrent with applied potential and also a further negative shift of the slopes. The results show that TO has the highest negative value of OCP. This is associated with a significant potential to reduce the

photo-generated electrons that favors the formation of the superoxide and hydroxyl radicals required for the oxidation process.

On the other hand, BVO exhibits a lower negative value than TO, indicating that the electrons are accumulated in lower energy levels. These results agree with the Mott Schottky measurements. The results of TO/ BVO nanocomposites show that the electrons are localized in lower energy levels than in the case of the pristine materials. Such levels are associated with the formation of surface states at the interface of TO/ BVO with high BVO content. Besides, when the illumination is interrupted, the OCP for BVO and TO/ BVO nanocomposites recovers more slowly than TO, indicating that electrons are sluggishly transferred to species in the solution [45].

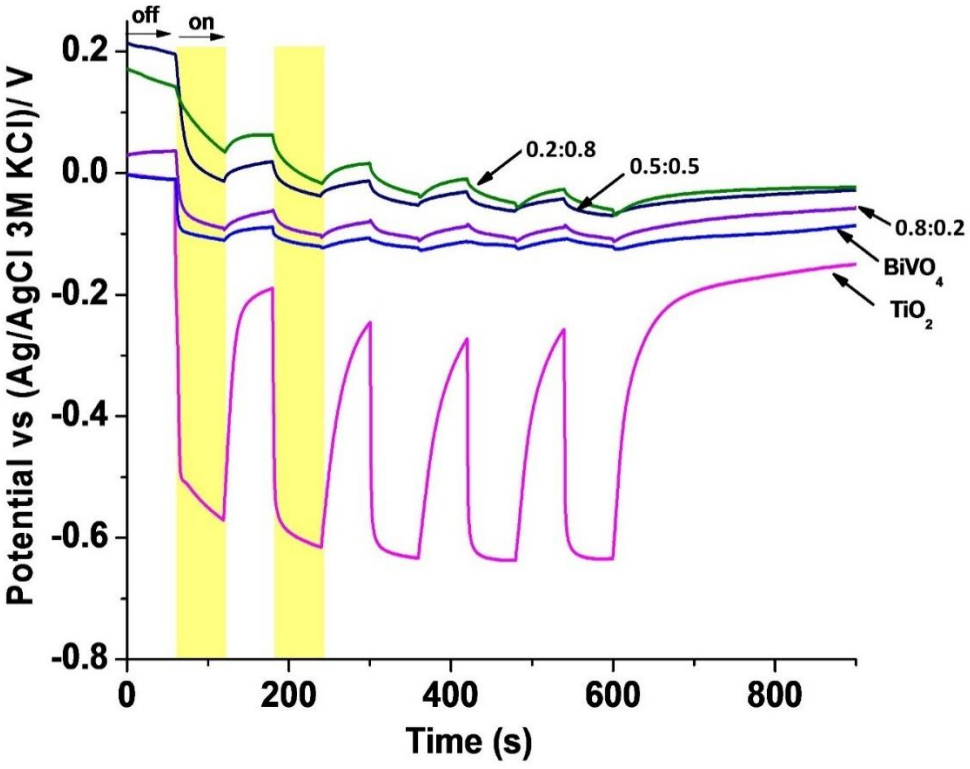

Fig. 3.13 Time evolution of the open circuit potential (OCP) in the dark (off) and under UV illumination (on) for the synthesized nanocomposites.

According to the above results, the photo-generated electrons are transferred from TO toward BVO and the reverse for the photo-generated holes [46]. The photo-generated electrons in TO have a significant reduction potential that can reduce surface chemisorbed O_2 to yield strong oxidizing radicals [47]. However, it is essential to mention that the material with low BVO content exhibits the best behavior among the composites. This

results from the flat band potential of the material and the potential reduction of its photo-generated electrons. Also, there observed an increase in the crystallite size of the nanocomposites with an increase in the concentration of the BVO due to its comparatively higher atomic radius. Hence the composite with a low concentration of BVO (0.8:0.2) has shown a reduced crystallite size; resulting in more number of available crystallites per unit area and, in addition to that, a negative shift in the flat band potential, which further provided more electrons for the reactions and improved the charge transfer properties of the material which also contributed towards the excellent activity of the nanocomposites. The 0.8:0.2 ratio has shown a higher negative value for the flat band potential than the other samples and the pristine materials; this causes a significant difference in its pc efficiency. When the photons of sufficient energy incidents upon the catalyst surface, the electron-hole pairs are created. Since the negative flat band potential provided a lower conduction band minimum and hence the barrier is less for the charge separation, and that favors more charge carriers over the surface of the material, which will be available for the further redox reactions.

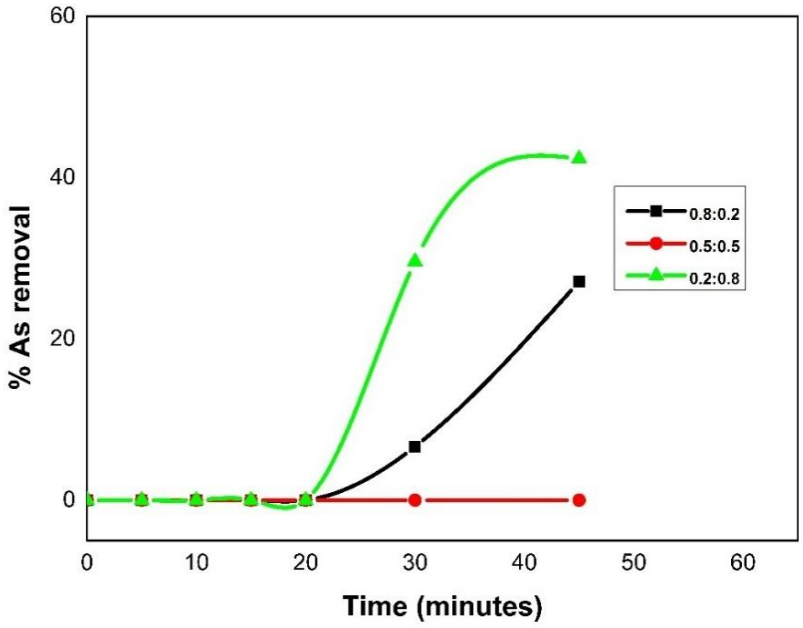

Fig. 3.14 Illustration of the circumstance that backs the synthesis of new set (Set B) of nanocomposites for the As(III) oxidation/removal

The As(III) oxidation/removal tests have been performed with the set A of the nanocomposites (0.8:0.2, 0.5:0.5, 0.2:0.8) and there observed a very low percentage of removal. And hence synthesized another set of nanocomposites with very low mass percentage of the BVO. And the preliminary test result has shown in the fig. 3.14. It can be observed that the Set A composites have shown less percentage removal. Hence new set B

with low percentage of BVO has synthesized. Five different sets of nanocomposites where synthesized with the aim to choose the best composite under optimum conditions for the pc oxidation/removal of the As(III). For the As removal, the optimization of the parameters were carried out using the Response surface methodology (RSM). Optimization and characterization of the new Set B materials have discussed in the chapter.4.

References

[1] U. I. Gaya and A. H. Abdullah, "Heterogeneous photocatalytic degradation of organic contaminants over titanium dioxide: A review of fundamentals, progress and problems," *J. Photochem. Photobiol. C Photochem. Rev.*, vol. 9, no. 1, pp. 1–12, 2008.

[2] L. Zhang, G. Tan, S. Wei, H. Ren, A. Xia, and Y. Luo, "Microwave hydrothermal synthesis and photocatalytic properties of TiO2/BiVO4 composite photocatalysts," *Ceram. Int.*, vol. 39, no. 8, pp. 8597–8604, 2013.

[3] M. M. Khan *et al.*, "Band gap engineered TiO 2 nanoparticles for visible light induced photoelectrochemical and photocatalytic studies," *J. Mater. Chem. A*, vol. 2, no. 3, pp. 637–644, 2014.

[4] S. Mansour, R. Akkari, S. Ben Chaabene, and M. Saïd Zina, "Effect of Surface Site Defects on Photocatalytic Properties of BiVO4/TiO2 Heterojunction for Enhanced Methylene Blue Degradation," *Adv. Mater. Sci. Eng.*, vol. 2020, pp. 1–16, 2020.

[5] Z. Jian, S. Huang, Y. Cao, and Y. Zhang, "Hydrothermal Preparation and Characterization of TiO 2 /BiVO 4 Composite Catalyst and its Photolysis of Water to Produce Hydrogen," *Photochem. Photobiol.*, vol. 92, no. 3, pp. 363–370, 2016.

[6] W. F. Zhang, Y. L. He, M. S. Zhang, Z. Yin, and Q. Chen, "Raman scattering study on anatase TiO 2 nanocrystals," *J. Phys. D. Appl. Phys.*, vol. 33, no. 8, pp. 912–916, 2000.

[7] A. Kudo, K. Omori, and H. Kato, "A Novel Aqueous Process for Preparation of Crystal Form-Controlled and Highly Crystalline BiVO 4 Powder from Layered Vanadates at Room Temperature and Its Photocatalytic and Photophysical Properties," *J. Am. Chem. Soc.*, vol. 121, no. 49, pp. 11459–11467, 1999.

[8] J. Matos, A. García, L. Zhao, and M. M. Titirici, "Solvothermal carbon-doped TiO2 photocatalyst for the enhanced methylene blue degradation under visible light," *Appl. Catal. A Gen.*, vol. 390, no. 1–2, pp. 175–182, 2010.

[9] S. N. Jain and P. R. Gogate, "Acid Blue 113 removal from aqueous solution using novel biosorbent based on NaOH treated and surfactant modified fallen leaves of Prunus Dulcis," *J. Environ. Chem. Eng.*, vol. 5, no. 4, pp. 3384–3394,2017.

[10] S. M. Thalluri, S. Hernández, S. Bensaid, G. Saracco, and N. Russo, "Green-synthesized W- and Mo-doped BiVO4 oriented along the {0 4 0} facet with enhanced activity for the sun-driven water oxidation," *Appl. Catal. B Environ.*, vol. 180, pp. 630–636, 2016.

[11] R. Venkatesan, S. Velumani, and A. Kassiba, "Mechanochemical synthesis of nanostructured BiVO4 and investigations of related features," *Mater. Chem. Phys.*, vol. 135, no. 2–3, pp. 842–848, 2012.

[12] R. Venkatesan, S. Velumani, K. Ordon, M. Makowska-Janusik, G. Corbel, and A. Kassiba, "Nanostructured bismuth vanadate (BiVO4) thin films for efficient visible light photocatalysis," *Mater. Chem. Phys.*, vol. 205, pp. 325–333, 2018.

[13] J. Li, C. Zhong, J. Huang, Y. Chen, Z. Wang, and Z. Liu, “Carbon dots decorated three-dimensionally ordered macroporous bismuth-doped titanium dioxide with efficient charge separation for high performance photocatalysis,” *J. Colloid Interface Sci.*, vol. 553, pp. 758–767, 2019.

[14] J. G. Yu, Y. R. Su, and B. Cheng, “Template-Free Fabrication and Enhanced Photocatalytic Activity of Hierarchical Macro-/Mesoporous Titania,” *Adv. Funct. Mater.*, vol. 17, no. 12, pp. 1984–1990, 2007.

[15] O. Frank, M. Zukalova, B. Laskova, J. Kürti, J. Koltai, and L. Kavan, “Raman spectra of titanium dioxide (anatase, rutile) with identified oxygen isotopes (16, 17, 18),” *Phys. Chem. Chem. Phys.*, vol. 14, no. 42, p. 14567, 2012.

[16] N. Li *et al.*, “High quality sulfur-doped titanium dioxide nanocatalysts with visible light photocatalytic activity from non-hydrolytic thermolysis synthesis,” *Inorg. Chem. Front.*, vol. 1, no. 7, pp. 521–525, 2014.

[17] S. Rehman, R. Ullah, A. M. Butt, and N. D. Gohar, “Strategies of making TiO2 and ZnO visible light active,” *J. Hazard. Mater.*, vol. 170, no. 2–3, pp. 560–569, 2009.

[18] V. Merupo, S. Velumani, K. Ordon, N. Errien, J. Szade, and A. Kassiba, “Structural and optical characterization of ball-milled copper-doped bismuth vanadium oxide (BiVO 4),” *CrystEngComm*, vol. 17, no. 17, pp. 3366–3375, 2015.

[19] X. Li, Z. Zhang, F.-J. Zhang, J. Liu, J. Ye, and W.-C. Oh, “Synthesis and Photocatalytic Activity of TiO2/BiVO4 Layered Films under Visible Light Irradiation,” *J. Korean Ceram. Soc.*, vol. 53, no. 6, pp. 665–669, 2016.

[20] W. Wang, Q. Han, Z. Zhu, L. Zhang, S. Zhong, and B. Liu, “Enhanced photocatalytic degradation performance of organic contaminants by heterojunction photocatalyst BiVO4/TiO2/RGO and its compatibility on four different tetracycline antibiotics,” *Adv. Powder Technol.*, vol. 30, no. 9, pp. 1882–1896, 2019.

[21] A. Lasia, *Electrochemical Impedance Spectroscopy and its Applications*, vol. 9781461489. New York, NY: Springer New York, 2014.

[22] A. S. Bondarenko and G. A. Ragoisha, “Variable Mott-Schottky plots acquisition by potentiodynamic electrochemical impedance spectroscopy,” *J. Solid State Electrochem.*, vol. 9, no. 12, pp. 845–849, 2005.

[23] K. Gelderman, L. Lee, and S. W. Donne, “Flat-Band Potential of a Semiconductor: Using the Mott–Schottky Equation,” *J. Chem. Educ.*, vol. 84, no. 4, p. 685, 2007.

[24] D. C. De Moura, M. A. Quiroz, D. R. Da Silva, R. Salazar, and C. A. Martínez-Huitle, “Electrochemical degradation of Acid Blue 113 dye using TiO 2 -nanotubes decorated with PbO 2 as anode,” *Environ. Nanotechnology, Monit. Manag.*, vol. 5, pp. 13–20, 2016.

[25] L. Tian, Y. Guo, J. Li, F. Xia, M. Liang, and Y. Bai, “Effects of solidification cooling rate on the microstructure and mechanical properties of a cast Al-Si-Cu-Mg-Ni piston alloy,” *Materials (Basel).*, vol. 11, no. 7, pp. 3–11, 2018.

[26] J. Tu, “TEM Nano-Moiré Pattern Analysis of a Copper/Single Walled Carbon

Nanotube Nanocomposite Synthesized by Laser Surface Implanting," *C*, vol. 4, no. 1, p. 19, 2018.

[27] S. Selvarajan, A. Suganthi, M. Rajarajan, and K. Arunprasath, "Highly efficient BiVO4/WO3 nanocomposite towards superior photocatalytic performance," *Powder Technol.*, vol. 307, pp. 203–212, 2017.

[28] G. R. Surikanti, A. K. Bandarapu, and M. V. Sunkara, "A Facile One Pot Synthesis of Cu 2 O@TiO 2 : A Nanocomposite Catalyst for Enhanced Visible Light Driven Photocatalysis #," *ChemistrySelect*, vol. 4, no. 8, pp. 2249–2257, 2019.

[29] S. Nayak, G. Swain, and K. Parida, "Enhanced Photocatalytic Activities of RhB Degradation and H 2 Evolution from in Situ Formation of the Electrostatic Heterostructure MoS 2 /NiFe LDH Nanocomposite through the Z-Scheme Mechanism via p–n Heterojunctions," *ACS Appl. Mater. Interfaces*, vol. 11, no. 23, pp. 20923–20942, 2019.

[30] S. M. Majhi *et al.*, "Construction of novel hybrid PdO–ZnO p–n heterojunction nanostructures as a high-response sensor for acetaldehyde gas," *CrystEngComm*, vol. 21, no. 34, pp. 5084–5094, 2019.

[31] G. Longo, F. Fresno, S. Gross, and U. L. Štangar, "Synthesis of BiVO4/TiO2 composites and evaluation of their photocatalytic activity under indoor illumination," *Environ. Sci. Pollut. Res.*, vol. 21, no. 19, pp. 11189–11197, 2014.

[32] R. Rahimi, S. Zargari, and M. M. Moghaddas, "BiVO4-TiO2 nanocomposite: Synthesis and photocatalytic investigation," *Adv. Mater. Res.*, vol. 702, pp. 172–175, 2013.

[33] S. Talebi, N. Chaibakhsh, and Z. Moradi-Shoeili, "Application of nanoscale ZnS/TiO 2 composite for optimized photocatalytic decolorization of a textile dye," *J. Appl. Res. Technol.*, vol. 15, no. 4, pp. 378–385, 2017.

[34] L. Mohapatra and K. M. Parida, "Zn-Cr layered double hydroxide: Visible light responsive photocatalyst for photocatalytic degradation of organic pollutants," *Sep. Purif. Technol.*, vol. 91, pp. 73–80, 2012.

[35] N. Yan, Z. Zhu, J. Zhang, Z. Zhao, and Q. Liu, "Preparation and properties of ce-doped TiO2 photocatalyst," *Mater. Res. Bull.*, vol. 47, no. 8, pp. 1869–1873, 2012.

[36] Y. Wang *et al.*, "Synthesizing Co3O4-BiVO4/g-C3N4 heterojunction composites for superior photocatalytic redox activity," *Sep. Purif. Technol.*, vol. 239, p. 116562, 2020.

[37] X. H. Li and M. Antonietti, "Metal nanoparticles at mesoporous N-doped carbons and carbon nitrides: Functional mott–schottky heterojunctions for catalysis," *Chem. Soc. Rev.*, vol. 42, no. 16, pp. 6593–6604, 2013.

[38] W. Zhang,, Z. Chen, S.Li, Dye-sensitized solar cells based on Bi4Ti3O 12. *Int. J. Photoenergy*, vol. 2011, pp. 1–6, 2011

[39] S. J. Hong, S. Lee, J. S. Jang, and J. S. Lee, "Heterojunction BiVO4/WO3 electrodes for enhanced photoactivity of water oxidation," *Energy Environ. Sci.*, vol. 4, no. 5, p.

1781, 2011.

[40] H. Wang, J. He, G. Boschloo, H. Lindström, A. Hagfeldt, and S.-E. Lindquist, "Electrochemical Investigation of Traps in a Nanostructured TiO 2 Film," *J. Phys. Chem. B*, vol. 105, no. 13, pp. 2529–2533, 2001.

[41] D. Ramírez-Ortega, P. Acevedo-Peña, F. Tzompantzi, R. Arroyo, F. González, and I. González, "Energetic states in SnO2–TiO2 structures and their impact on interfacial charge transfer process," *J. Mater. Sci.*, vol. 52, no. 1, pp. 260–275, 2017.

[42] D. Guerrero-Araque, P. Acevedo-Peña, D. Ramírez-Ortega, and R. Gómez, "Improving photocatalytic reduction of 4-nitrophenol over ZrO 2 –TiO 2 by synergistic interaction between methanol and sulfite ions," *New J. Chem.*, vol. 41, no. 21, pp. 12655–12663, 2017.

[43] C. Liu, J. Su, and L. Guo, "Comparison of sandwich and fingers-crossing type WO 3 /BiVO 4 multilayer heterojunctions for photoelectrochemical water oxidation," *RSC Adv.*, vol. 6, no. 33, pp. 27557–27565, 2016.

[44] Y. Wang *et al.*, "Fabrication of BiVO4/BiPO4/GO composite photocatalytic material for the visible light-driven degradation," *J. Clean. Prod.*, vol. 247, no. xxxx, p. 119108, 2020.

[45] J. Resasco *et al.*, "TiO 2 /BiVO 4 Nanowire Heterostructure Photoanodes Based on Type II Band Alignment," *ACS Cent. Sci.*, vol. 2, no. 2, pp. 80–88, 2016.

[46] S. Obregón and G. Colón, "A ternary Er3+-BiVO4/TiO2 complex heterostructure with excellent photocatalytic performance," *RSC Adv.*, vol. 4, no. 14, p. 6920, 2014.

[47] W. Su, J. Chen, L. Wu, X. Wang, X. Wang, and X. Fu, "Visible light photocatalysis on praseodymium(III)-nitrate-modified TiO2 prepared by an ultrasound method," *Appl. Catal. B Environ.*, vol. 77, no. 3–4, pp. 264–271, 2008.

CHAPTER. 4

PC Oxidation of As(III) and optimization using CCD and RSM

As the previous nanocomposites were comparatively less efficient for the As removal, a new set of nanocomposites with a low mass percentage of BVO was synthesized (% BVO= 0.5, 1, 1.5, 2, 2.5%). The synthesized nanocomposite was used for the As(III) oxidation. The optimization of the processing parameters for pc oxidation has been carried out using a response surface method (RSM). An experimental design with 20 sets of experiments has been generated and certain statistical analysis has performed with the help of Stratgraphics software to make the optimization process easier.

4.1 Analysis of Variance (ANOVA) for the optimization of the processing parameters; Experimental design based on statistical Analysis

Analysis of variance (ANOVA) is a statistical analysis tool used to analyze the variation within a specific data group. In the present scenario we analyzed the As(III) oxidation under the influence of certain parameters. A set of parameters was defined with five levels for each. And a set of 20 experiments were designed from the mentioned levels with the help of ANOVA. We used RSM to optimize the parameters to carry out the optimization with minimum sets of experiments [1,2]. ANOVA measures the variation of the parameters from the statistically calculated response. Moreover, all the statistical and graphical analysis of the experimental data are performed using the Software 'Stratgraphics'.

First of all, the parameters for the process have to be considered. In our case, [dosage], pH and % BVO in the composite are considered as three parameters and also termed as factors. To find the optimal response within the specified range of the parameters (factors), we have used a central composite design (CCD) [3] with five levels. Each factor/parameter assigned with five arbitrary values, and each real value was assigned with certain level values (-2, -1, 0, 1, 2) with a central factor/parameter corresponding to the level value of zero [4]. The CCD contributes to ANOVA to analyze the effect of individual parameters/factors or their cumulative effect on the final response/ results of the process (pc process) [5].

Table. 4.1 Levels of the parameters studied in the central composite design (CCD).

Parameter		**Levels and Values**				
		-2	**-1**	**0**	**1**	**2**
pH	A	3	5	7	9	11
Dose(g/l)	B	0.1	0.575	1.05	1.575	2
% BVO	C	0.5	1	1.5	2	2.5

The experiment should consist of more than two levels for each variable parameter, i.e., more than two real values for each parameter; for example, consider the case of pH. The five values are; 3,5,7,9 and 11 corresponding to its level values; -2, -1,0,1,2 respectively [6]. The higher value as +2 and lowest value as -2 [7]. We estimate the optimum values of the parameters obtained using the 3-dimensional response surface analysis [8]. A response surface will be generated based on the final results from each set, depending on the interaction of the parameters. This response surface qualifies the relation between the variable input parameters and the received response surfaces with minimum number of experimental runs [1,9]. All the processes will be explained in the coming sessions.

From table. 4.1 it can be seen that factors/ parameters chosen for the experiment as mentioned above with corresponding values. The level values make the notations in the experimental design easier. The objective of the process is to choose an optimum value for each parameter and also to identify the parameter with significant influence on the process.

4.1.1 The steps involved in the process;

- Identify the parameters influencing the process.
- Assign different level values corresponding to real values of the parameters /factors
- Formulation of the set of experiments to be carried out and their execution with variable parameters (factors with different levels)
- Develop the mathematical model to have the best fit and deduce the optimal set of factors from the obtained response surfaces

- Representing the direct and interactive effects of process parameters through the surface plots
- Find the parameter which has a better influence on the process.

There are two types of analysis designs.

- Central composite design (CCD)
- Box- Behnken method

These two procedures require a different number of runs. The CCD is preferable since it gives almost all the information on the multi-level factorial with fewer experimental runs with required combinations of parameters. This process describes the majority of the steady-state process response [1]. The set of operating parameters have been designed (pH, %BVO, dosage of the nanocomposite), and each variable is assigned to different levels. The set of twenty experiments derived using the defined levels (table 4.2). And with combinations of parameters/factors corresponding to each set of experiments. The parameters/factors are marked with their corresponding level values as in table. 4.2.

Table. 4.2 20 sets of experiments with different levels of Parameters (LE) (Input)

Set	**LE(pH)**	**LE(Dosage)**	**LE (%BVO)**
1	0	0	0
2	0	0	0
3	1	-1	1
4	1	1	-1
5	0	0	0
6	1	1	1
7	-1	1	1
8	0	0	0
9	-1	-1	1
10	-2	0	0
11	0	2	0
12	0	0	-2
13	0	0	0

14	-1	1	-1
15	1	-1	-1
16	2	0	0
17	0	-2	0
18	-1	-1	-1
19	0	0	2
20	0	0	0

The data from table.4.2 were fitted onto a polynomial equation with the help of ANOVA [5]. A second-order equation is generated to define the dependency between the response and the factors (parameters) as follows:

$$\mathbf{Y= A_0 + A_1X_1 + A_2X_2 + A_3X_3 + A_{11}X_1^2 + A_{22}X_2^2 + A_{33}X_3^2 + A_{12}X_1X_2 + A_{13}X_1X_3 + A_{23}X_2X_3} \quad \mathbf{(1)}$$

With Y being the predicted response, A_0 a constant, A_1, A_2 & A_3 represent linear coefficients, A_{11}, A_{22} &A_{33} are quadratic coefficients, and A_{12}, A_{13} &A_{23} the cross-product coefficients. A regression analysis was used to fit this polynomial equation with the experimental data and the significance of each coefficients was determined with the help of ANOVA [10,11]. ANOVA (table. 4.3) provides the idea on interaction between the variables and their response [12].

Consequently, a second-order equation is derived considering the effect of the variables (based on table 4.2) on the pc oxidation efficiency of the nanocomposite. The X_1,X_2,X_3 combinations are corresponding to the coupled effect of the variables on the response.

Y is the response that is the percentage removal of As(III). The percentage of removal is predicted by analyzing this second-order equation, where the equation implies the empirical relationship between the response and the variables (factors). The equation is generated so that the Y, the percentage As(III) removal as a function of the parameters/factors (pH, dosage, and & %BVO).

$$\mathbf{Y = 35.72 - 32.45*pH + 6.915*dose + 6.09*\%BVO + 6.68*pH\wedge 2 + 3.64*pH*dose + 1.40*pH*\%BVO - 1.09*dose\wedge 2 - 0.078*dose*\%BVO + 5.77*\%BVO\wedge 2} \quad \mathbf{(2)}$$

In this case, X_1, X_2, X_3 correspond to the pH, dosage, and percentage of BVO present in the nanocomposite, respectively that are the levels corresponding to each parameter as shown in the table. 4.1. The positive sign in the equation in front of the parameters represents a synergetic effect, and the negative sign is identified as an opposite impact [8].

The quality of statistical goodness of data in table 4.3 implies how well the model fits the data set [13]. Table. 4.4 shows the output of the input data mentioned in table.4.3. Both the fitted and observed results are given in table 4.4, which are in fair agreement.

Table 4.3 Statistical analysis of variance (ANOVA) the input parameters

Source	Sum of Squares	Df	Mean Square	F-Ratio	P-Value
A: pH	16845.4	1	16845.4	45.77	0.0000
B: Dose	765.076	1	765.076	2.08	0.1800
C: %BVO	594.628	1	594.628	1.62	0.2325
AA	1120.41	1	1120.41	3.04	0.1116
AB	105.997	1	105.997	0.29	0.6033
AC	15.736	1	15.736	0.04	0.8403
BB	29.7105	1	29.7105	0.08	0.7821
BC	0.04805	1	0.04805	0.00	0.9911
CC	836.485	1	836.485	2.27	0.1626
Total error	3680.78	10	368.078		
0 Total (corr.)	23917.1	19			

R^2 = 0.8416

The R^2 value defines the relevance of the model and the effects of the considered parameters on the responses, and it can be explained by the experimental factors and their interactions. In our model, there observed the R^2= 0.8416 means that the independent variables explain the 84.16 % of variations for the oxidation efficiency of As(III) or the percentage of removal by the consequent adsorption. It is worth noting that the model could not explain the remaining 15.84% of the variation. The quality and relevance of the model can be evaluated from the difference between the predicted and observed experimental values of the responses. The table. 4.3 gives the significance of the quadratic surface response. R^2-adj value also contributes to the strength of the model. It is supposed that the difference between the R^2 and R^2-adj should be negligible [14]. The F (value of fischer) [15] value is the ratio

of the mean square of the experimental model to the residual error [1]. The F value means that the parameter with a higher F is the one that has a stronger influence on the process [16,17]. Thus, pH seemed to have a stronger impact on the pc removal of As(III), with pH having an F- value of 45.77 and a low P-value[18]. It reported that the P-value of the parameters of most substantial influence will always be less than 0.5[19] and the one with lowest P-value is of highest influence on the process.

Table 4.4 Results of the 20sets of experiments (output)

Set	Experimental	Fitted
1	38.78	35.7209
2	33.2	35.7209
3	9.43	11.651
4	26.05	17.7635
5	22.3	35.7209
6	23.68	32.606
7	100.0	87.416
8	39.37	35.7209
9	92.33	81.021
10	100.0	127.318
11	38.12	45.2027
12	23.58	46.6002
13	24.0	35.7209
14	100.0	78.1835
15	3.51	-3.50148
16	5.25	-2.47227
17	5.03	17.5427
18	100.0	71.4785
19	74.41	70.9852
20	37.08	35.7209

Fig. 4.1 is the representation of the output of Table. 4.4. Outcomes of the 20 sets of the experiments are represented as a bar diagram. ANOVA calculates the parameter with higher

influence. Itis found based on the parameters used in the each set of experiments. The extend of influence pf paremetersis represented as a Pareto chart (fig. 4.1).

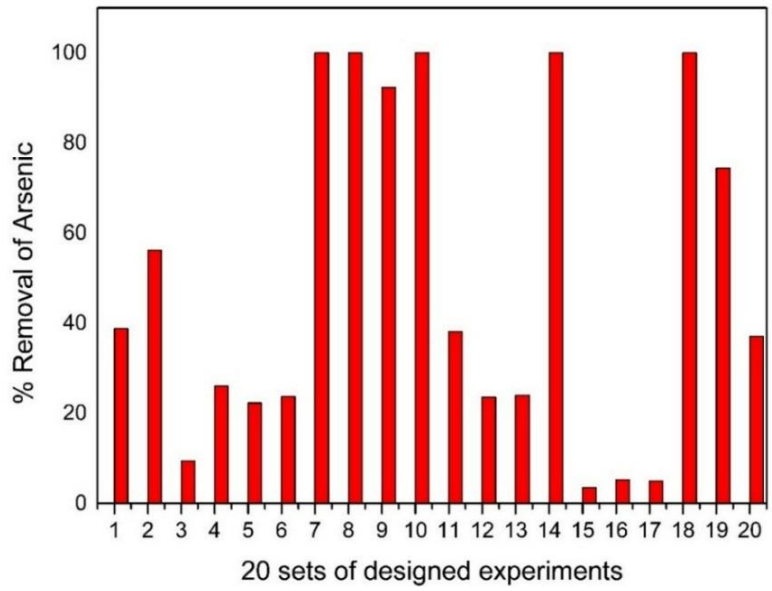

Fig. 4.1 Representation of the output from the 20 sets of experiments

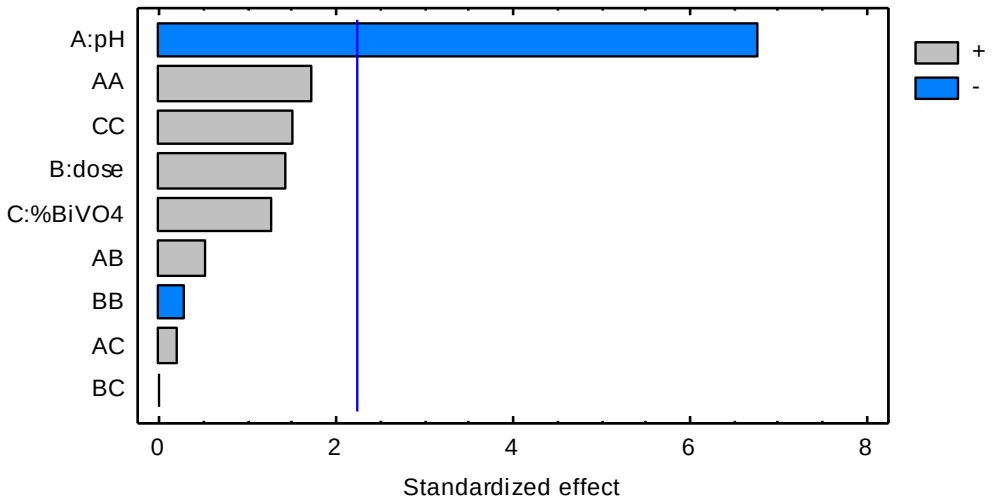

Fig. 4.2 Standard pareto chat on the effect of the parameters on the process

Table 4.5. Real value of the factors corresponding to the optimized level value

Factor	Low	High	Optimum	Real values
pH	-2	2	-1.4567	4
Dose	-2	2	0.8297	1.5 g/l
%BVO	-2	2	0.3690	Between (1.5- 2)%

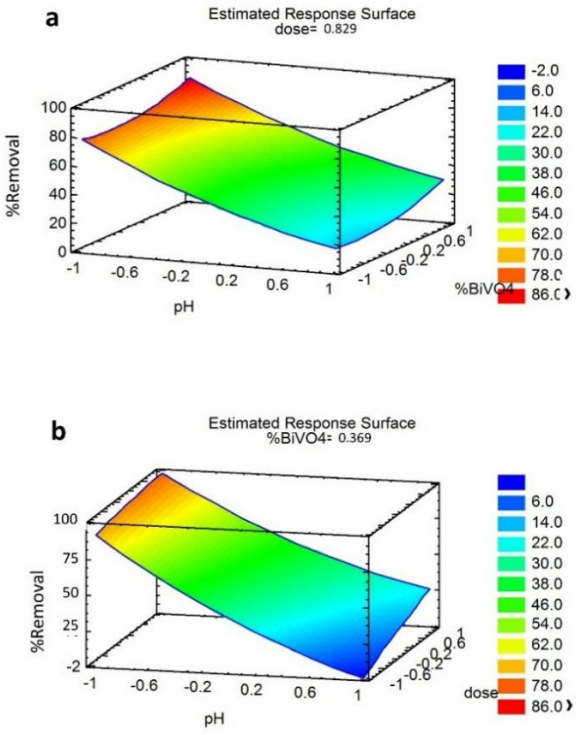

Fig. 4.3 Response surface for different parameters

The standardized Pareto chart provides essential information for interpreting the ANOVA results, which is the graphic representation of the magnitude of the effect of each parameter [1, 20] on the pc process. From the chart, fig. 4.2, it is clear that the factor with the most influence on the reaction is the pH of the media. The real values obtained corresponding to each parameter are; pH= 4, dose= 1.5g/l and % BVO= 1.5-2%. The experiments carried out using these real values and their results are discussed in the forthcoming sections. The surface response curves as a function of pH, % BVO, and the dosage are given in fig. 4.3, which explains the interaction between the parameters [21]. The tendency is similar to that observed from the Pareto chart in fig. 4.2.

From the Pareto chart, it is identified that the pH and dosage are the factors with a comparatively stronger influence on the process. Hence, the response surface has been generated based on this. The response surface is the graphical representation of the polynomial equation derived from the ANOVA analysis. These surfaces represent the interaction between the variable within their range [22]. From fig. 4.3a, the response % increases as the pH approaches -1.45 and dosage to 0.829. Further discussions on the results are explained in the forthcoming sections.

4.2 Characterization of the synthesized Nanocomposites

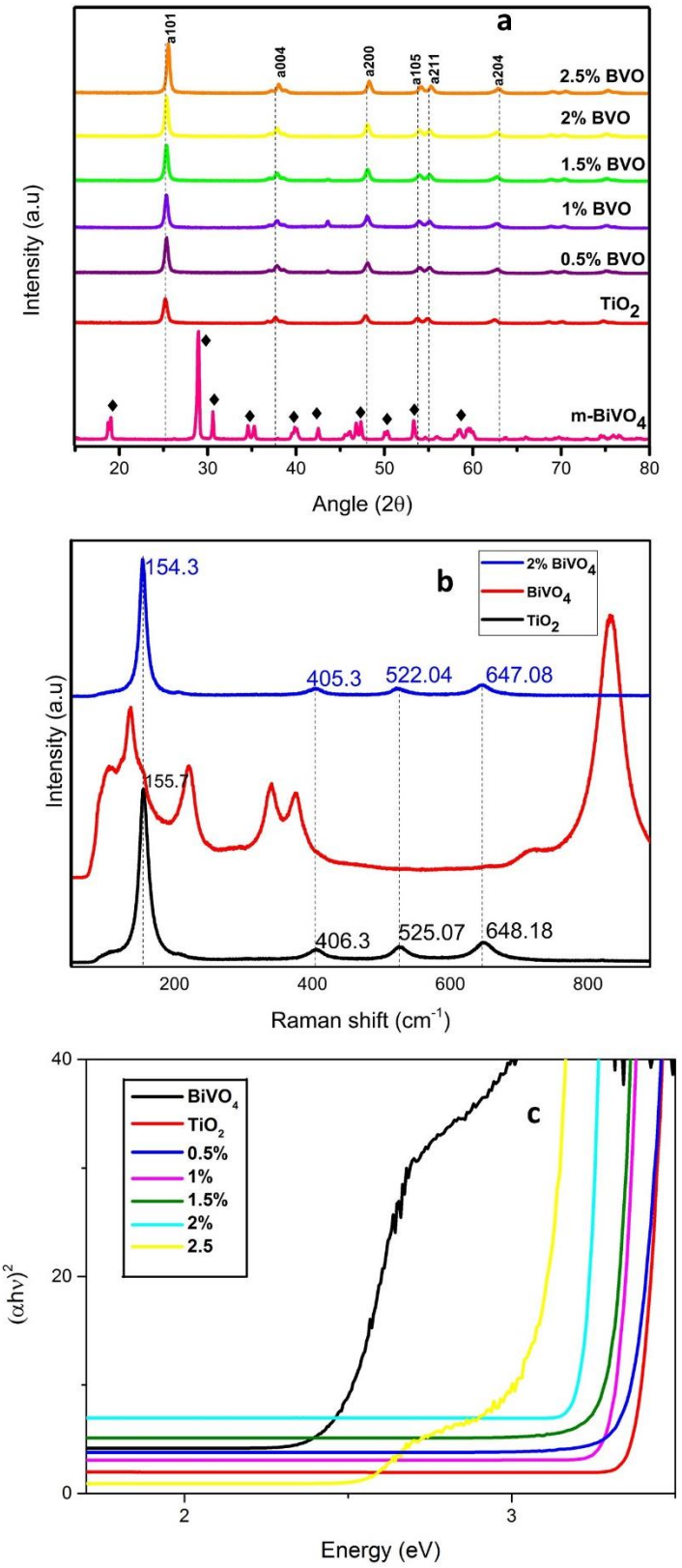

Fig. 4.4 a) X-ray diffractograms of the nanocomposites with the pristine materials

b) Raman spectra of the samples c) Band gap analysis of the samples

The structural and optical characterizations resemble that of the previous set of nanocomposites (chapter.3) and are explained below.

4.2.1 X-ray Diffraction analysis

The X-ray diagram of the sol-gel synthesized nanocomposites with low weight % of BVO has been illustrated in fig. 4.4a. The diagram of the nanocomposites is shown in comparison with that of the BVO and TO and is matched with the standard Pdfs (JCPDS-00-75-1866 for BVO and JCPDS-00-0121-1272 for TO, respectively) [23]. It is observed that there are no diffractions observed from the BVO due to its very low percentage in the nanocomposite. Furthermore, the significant peaks from the TO phase are present all along, keeping a good crystallinity of the material. The crystallite sizes of the nanocomposites have calculated using the Scherrer equation [24](see Table 4.6). The lattice strain and dislocation density has also calculated using the Scherrer calculation as in chapter.3, section 3.1 [25-27]. It is observed a slight variation in the crystallite size. The nanocomposite with 1.5 -2% BVO showed up with crystallite size of around 28 nm. And that of the 2.5 % with 26.8nm and of the pure TO was 28.36nm. Also, there observed a slight increase in the dislocation density of the samples. The composite materials except the one with 0.5% BVO shown a dislocation of around 1.8 $*10^{-3}$ nm^{-2}, which was higher compared to that of the pure TO. This may be due to the introduction of BVO into the TO matrix. The Lattice strain was calculated using the equation;

$$\boldsymbol{Lattice\ strain} = \frac{\beta}{\boldsymbol{tan\theta}} \qquad \textbf{(1)}$$

β is the FWHM and Θ is the angle of diffraction.

Table 4.6 FWHM and Crystalline size calculation

Sample	The crystallite size (nm)	Dislocation density ($*10^{-3}$ nm^{-2})	Lattice strain
0.5	30	1.5	0.305
1	32	1.85	0.305
1.5	29	1.80	0.348
2	28	1.80	0.336
2.5	27	1.81	0.342
TO	28	1.57	0.33

There observed a decrease in the FWHM of the composite peaks compared to that of the pure TO; for pure TO, the value of FWHM was nearly 0.37 where as in the case of composites, there observed, 0.27, 0.12, 0.31, 0.28, and 0.25 for 0.5, 1, 1.5, 2, 2.5%BVO samples respectively. This may be due to the dislocations caused by the introduction of BVO into the TO lattice since FWHM is sensitive to microstructural variations [28].

4.2.2 Raman Analysis

Raman analysis in fig. 4.4b of the nanocomposite has been done in comparison with the TO for the identification of the vibrational modes of the molecules and, hence, for the structural identification of the sample. The peak around 154cm^{-1} corresponds to the E_g vibrational mode of the TO phase. 406.3, 526.4, and 648.8cm^{-1} correspond to the A_{1g}, B_{2g}, and E_g vibrations of the same phase

Furthermore, the raman analysis agrees with the xrd analysis since it confirmed the presence of well-crystallized TO. There seems a slight shift in the peaks of the composite material, and it is reported that the slight shift along with the reduced intensity of the peaks in the composite can be due to the phonon confinement and oxygen deficiency due to the introduction of the BVO, which is a minor phase into the system. Moreover, from the X-ray diagrams, we have calculated the crystallite size and there is an increase in the crystallite size which can explain the slight broadening and reduced intensity of the nanocomposite peak [29].

4.2.3 Bandgap Analysis

The bandgap measurement has been illustrated in the plot (fig. 4.4c). therefrom the band gap values, thee found a slight difference in the bandgap of each sample materials. The band gap is found from the Tauc plot. There observed a small difference in the bandgap of the composite materials. From 0.5 to 2%, there followed a slight decrease in the bandgap (Table 4.4c), and this could be due to the introduction of BVO into TO lattice.

Table 4.7. Bandgap values of the nanocomposites and their components

Material	Band gap(eV)
TO	3.28
BVO	2.36
0.5%	3.17
1%	3.11
1.5%	3.06

2%	3.03
2.5%	3.00

4.2.4 Scanning Electron Microscope (SEM) analysis

The SEM analysis of the material has been done, and the morphology seems to be of agglomerated spherical granules of the nanoparticles. The EDS analysis and the mapping have been done to confirm the presence of the elements Bi, V, O and Ti since the xrd and raman analysis was limited with the detection. The mapping analysis was illustrated in fig. 4.5, and from that, the distribution of each constituent seemed to be homogeneously distributed over the sample.

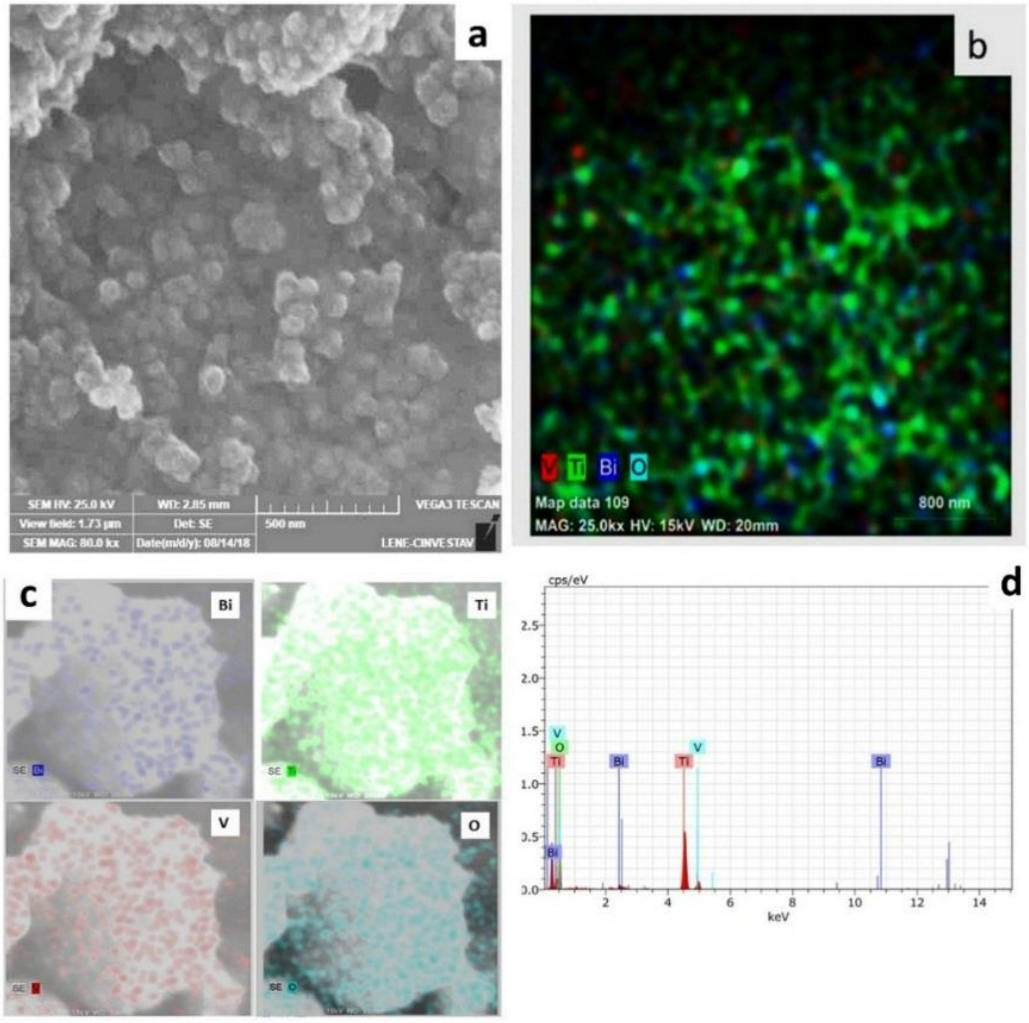

Fig. 4.5 a) SEM micrograph of the nanocomposite b) Mapping analysis c) Mapping analysis of the nanocomposite with 2%BVO d) EDS Chemical analysis

Fig. 4.5b is the mapping of the whole selected area showing the distribution of all the elements. And fig. 4.5c is the mapping image of the sample with the mapping that has done

for each element separately. The EDS mapping analysis confirms the presence of all the elements; Bi, V, Ti and O from BVO and TO.

4.2.5 Brunauer Emmet Teller- Surface area analysis

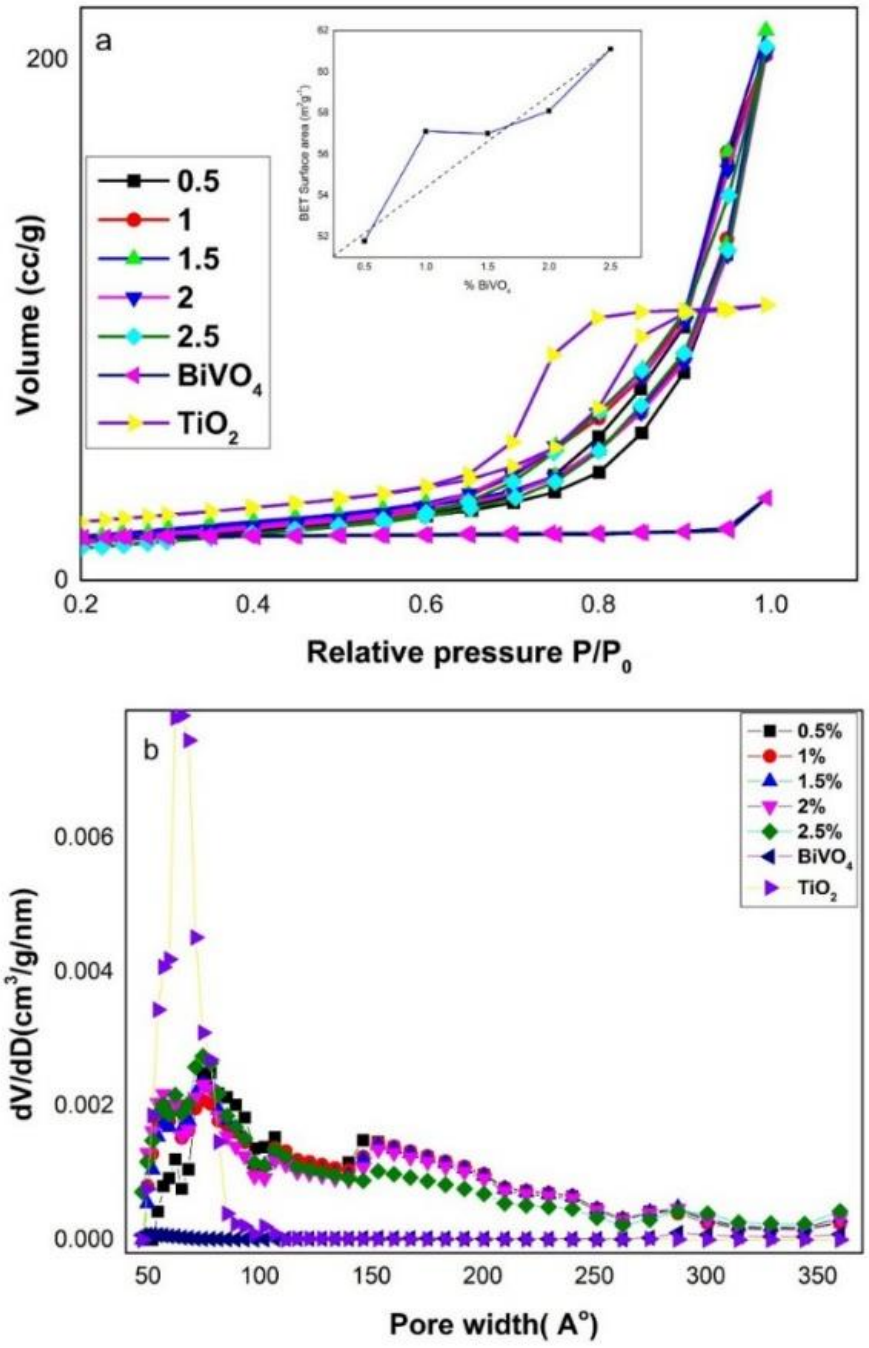

Fig. 4.6 a) BET-Surface area analysis of the modified samples (in the inset Surface area vs. %BVO plot) b) Pore volume analysis of the samples

The BET surface area and pore volume analysis have been performed on the TO/BVO samples and illustrated in fig. 4.6 a and b, respectively. A multi-point BJH analysis has been performed. The nitrogen adsorption-desorption isotherm and pore size distribution have been shown. The measurement was done by nitrogen adsorption on the surface of the materials as a function of relative pressure (P/P_0). As in fig. 4.6a, type-2 isotherm as per the Brunauer classification [30, 31] within the P/P_0 ranging from 0.05 to 1. The measured values are indicated within each plot.

The specific surface area of BVO and TO alone was found to be 29.6m^2/g and 56.5 m^2/g, respectively. The pore diameter is found to be below 20 nm, as observed from fig. 4.6a. Fig.4.6a inset is just an illustration of the effect of the % BVO on the specific surface area, and it was observed that, a tendency of a slight increase in the surface area with the increased %BVO which may be due to the influence of BVO on the grain growth during the calcination process [32]. The nanocomposite material is mesoporous since the pore diameter is below 20 nm, which is in the range of the standard 2-50nm for the mesoporous materials.

4.3 Photocatalytic degradation tests

As a primary step, the calibration curve was generated for As(III) and (V) as in fig. 4.7. This may help in analyzing the concentration of the solution at each interval [27]. The peak intensity at 871nm was used as the reference leading to a linear curve of calibration [33]. The pc experiments have been carried out under the optimized conditions of pH, dosage, and the optimal percentage of the BVO in the nanocomposite material. The experimental conditions were set at a pH of nearly 4 and a dosage of 1.5g/l as obtained from the optimization methods (RSM/ CCD). The tests were carried out for 150 minutes, and the aliquots were extracted each 5,10,15,20,30, 60 and 150 minutes. Each sample was treated with the prepared ammonium molybdate- antimony (SbA) solution, as mentioned in chapter.2. The initial concentration of the As(III) was 2ppm. The SbA solution can form a blue color complex with As and in the case of As total, the aliquot sample is treated with KMnO4 and SbA. To identify the presence of As(V) SbA solution was used as mentioned in Chapter.2. Once the complexing agent is added, the solution turns blue color depending upon the concentration of the As present. At this stage, the concentration is measured using the absorbance and further the percentage removal with the equation [34];

$$\%\,\boldsymbol{Degradation} = \frac{\boldsymbol{C0-C}}{\boldsymbol{C0}} * \mathbf{100} \qquad \textbf{(2)}$$

The concentration of the existing As(III) is measured by;

$$\boldsymbol{As(III) = As(Total) - As(V)} \qquad \textbf{(3)}$$

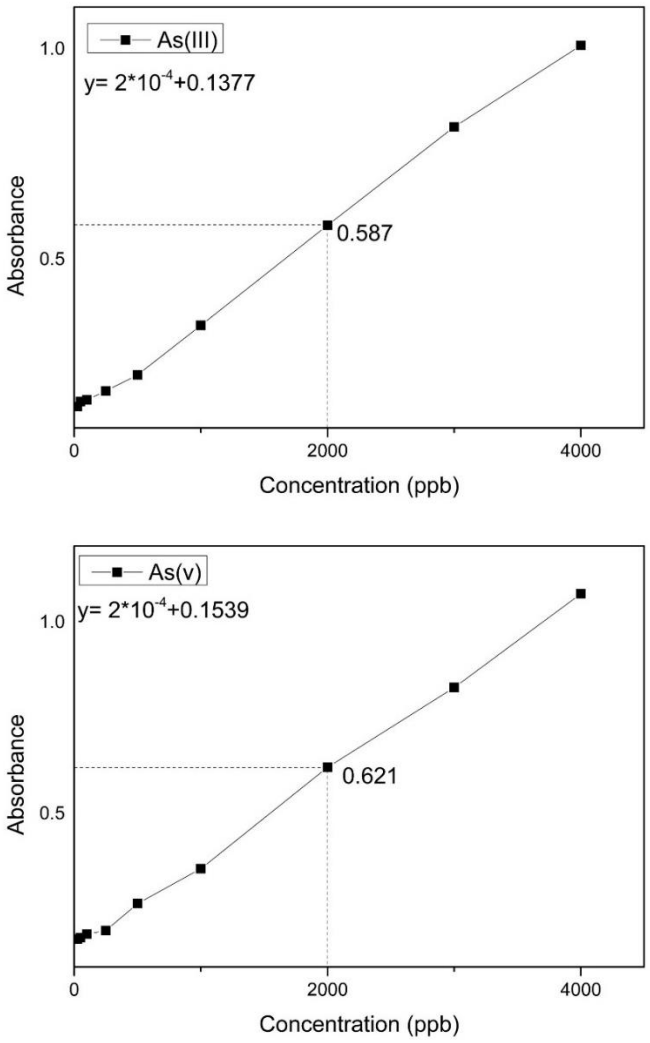

Fig. 4.7 Calibration curves for As(III) and As(V)

Thus, a total oxidation of As(III) and subsequent removal of the As(V) by the photocatalysts, are caused by the adsorption process defines the whole process. Hence the complete removal of As is due to the synergetic effect from both photocatalysis and further adsorption. The plots show the oxidation rate and the subsequent removal by adsorption of the As(total). 100 percent of the As removal was under the optimized pH, dosage, and percentage BVO.

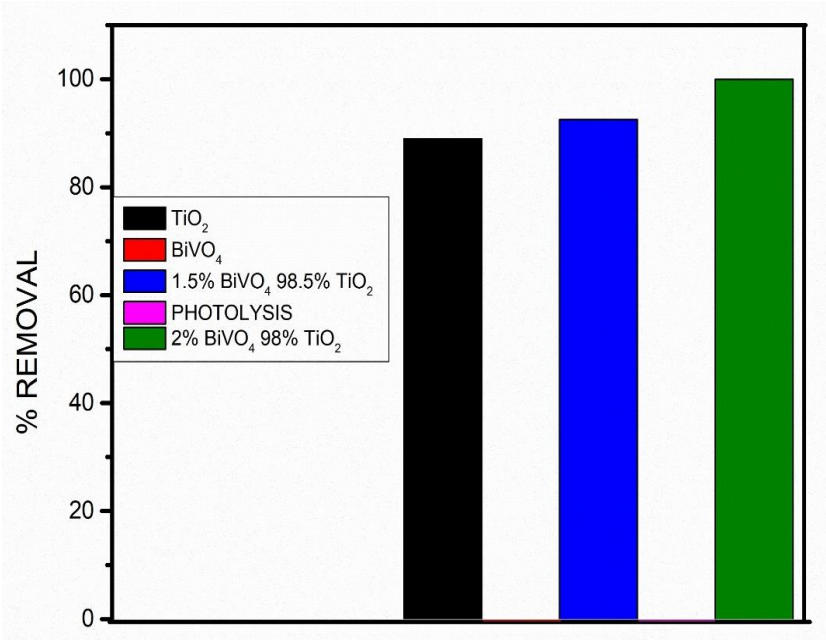

Fig. 4.8 Comparison of the removal efficiency of nanocomposites with BVO= 1.5 & 2%, BVO and TO

Fig. 4.8 is the bar- diagram of the % removal of the As total by the photocatalyst materials compared with their parent compounds. It is observed that the nanocomposite achieved the complete removal of As(total) with 2% of BVO. The TO alone has shown lesser activity of nearly 90 percent. The BVO alone has shown a negligible effect on the removal process, and hence it is not visible in the plot.

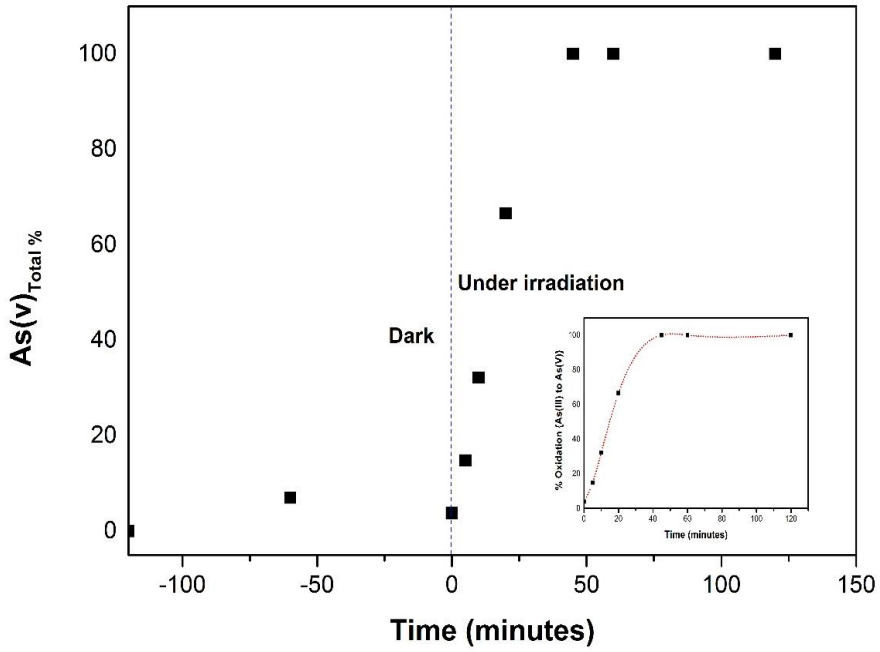

Fig. 4.9 Percentage removal of As total using optimized nanocomposite with BVO=2% . In the inset: percentage oxidation of As(III) to As(V)

Within the 50 minutes of irradiation, there was a complete oxidation of As(III) into As(V) (Fig.4.9). There followed a negligible effect from the adsorption that removed nearly 6 %. The proposed reaction involved in the As removal process is given below. The photogenerated charge carriers from each constituent compound contribute to the pc process. The lifetime of the charge carriers is increased considering the band structure alignment as mentioned in the Chapter.3. As(III) oxidation has a strong dependence on the solution pH. During the pc reactions, there form many species such as hydroxyl radicals, photogenerated charge carriers, superoxide radicals, hydrogen peroxides, etc., as mentioned. It has been reported that the As(III) has a high tendency to change into As(IV) before forming As(V) under photocatalysis with the presence of the mentioned species.

Furthermore, As(IV) species get oxidized again during the reactions to form As(V) [29]. It is reported that the oxygen scavenges the photogenerated electrons and hence create Superoxide radicals. Thus these species can oxidize As(III) into As(IV), and subsequent reactions with oxygen can result in the formation of As(V).

$BVO + TO \longrightarrow e^-_{CB} + h^+_{VB}$ (Under irradiation)

$O_2 + e^-_{CB} \longrightarrow O_2^{\cdot -}$

$OH + h^+_{VB} \longrightarrow {}^{\cdot}OH$

$O_2^{\cdot -} + 2H^+ + e^-_{CB} \longrightarrow H_2O_2$

$H_2O_2 + e^-_{CB} \longrightarrow {}^{\cdot}OH + OH^-$

$H_2O_2 + h^+_{VB} \longrightarrow HO_2^{\cdot} + H^+$

$2O_2^{\cdot -} + 2\,H^+ \longrightarrow H_2O_2 + O_2$

Process of As(III) oxidation

$As(III) + O_2^{\cdot -}/\, HO_2^{\cdot} \longrightarrow As(IV)$

$As(IV) \xrightarrow{O_2} As(V)$

$As(III) + 2\, HO_2^{\cdot} \longrightarrow As(V) + 2\, OH^- + O_2$

$As(III) + {}^{\cdot}OH \longrightarrow As(IV) + OH^- \longrightarrow As(V)$

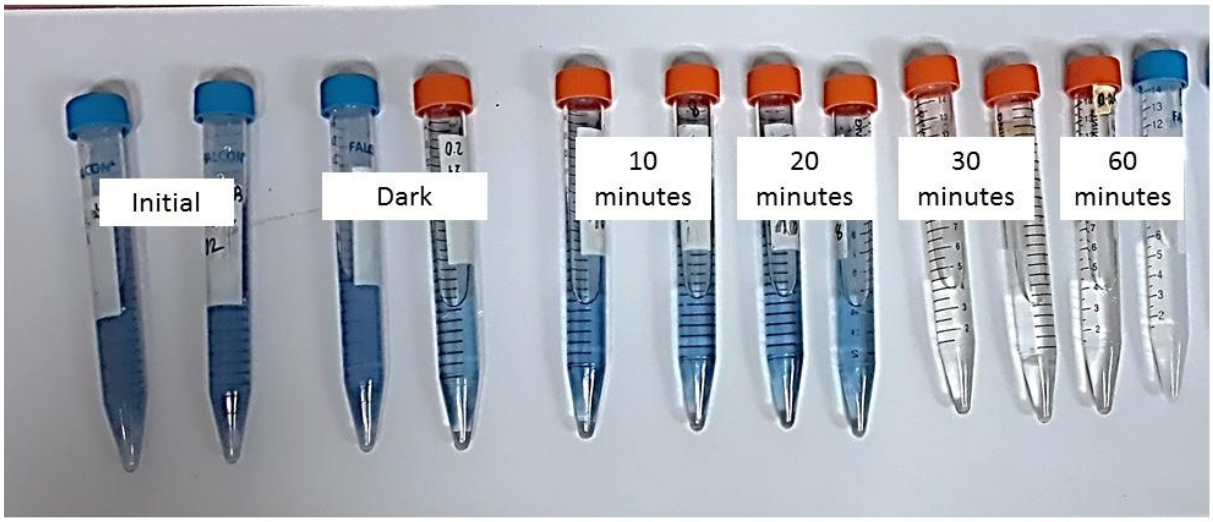

Fig. 4.10 Aliquot samples taken during different time intervals; under optimized conditions

Table. 4.8 Comparison of some existing research on As removal

Photocatalyst	**Photocatalysis- Experimental conditions**					**Final results**	**Author**
	Source	**Dosage(g/l)**	**$[As]_0$ (ppm)**	**Irradiation time (min)**	**Other conditions**		
Ag/TO/Fe_3O_4 @GO	Vis	0.4	24	30	Prepared Assolution (PA)	63% removal in 30 minutes	[36]
BVO/TO/LED	Visible	2	3	120	PA	100%	[37]
CuO/ZnO	UV	1	30	480	PA	100%	[38]
Cu-ZnO	Vis	3	5	120	PA	100%	[39]
$Ti(SO_4)_2$	UV	0.01	0.2	20	PA	100%	[40]
Fe-Titanate NT	UV	0.6	10	180	PA	99.6 %	[41]
Fe_2O_3-Mn_2O_3	UV	0.012	0.5	240	PA	>95 %	[42]
Current work-TO/BVO	Visible	1.5	2	50	PA	100%	

The current work is compared to similar research works for the removal of As from the water sample using various catalysts, as summarized in the table 4.8. From the present experiments using photocatalysts as TO/BVO composites, we achieved a complete removal of the total As with a dosage of 1.5g/l, $[As]_0$= 2ppm, pH= 4.5-5 which was the natural pH of the solution containing As. The removal was achieved within 50 minutes of visible light irradiation which underline the efficiency of the considered nanocomposites and the related interfaces area between BVO and TO.

References

[1] A. R. Khataee, M. Fathinia, S. Aber, and M. Zarei, "Optimization of photocatalytic treatment of dye solution on supported TiO 2 nanoparticles by central composite design : Intermediates identification," *J. Hazard. Mater.*, vol. 181, no. 1–3, pp. 886–897, 2010.

[2] D. Vildozo, C. Ferronato, M. Sleiman, and J. M. Chovelon, "Photocatalytic treatment of indoor air: Optimization of 2-propanol removal using a response surface methodology (RSM)," *Appl. Catal. B Environ.*, vol. 94, no. 3–4, pp. 303–310, 2010.

[3] M. R. Delsouz Khaki, M. S. Shafeeyan, A. A. A. Raman, and W. M. A. W. Daud, "Evaluating the efficiency of nano-sized Cu doped TiO2/ZnO photocatalyst under visible light irradiation," *J. Mol. Liq.*, vol. 258, pp. 354–365, 2018.

[4] M. Muthukumar, D. Sargunamani, N. Selvakumar, and J. V. Rao, "Optimisation of ozone treatment for colour and COD removal of acid dye effluent using central composite design experiment," vol. 63, pp. 127–134, 2004.

[5] E. K. Tetteh, S. Rathilal, and D. B. Naidoo, "Photocatalytic degradation of oily waste and phenol from a local South Africa oil refinery wastewater using response methodology," *Sci. Rep.*, vol. 10, no. 1, p. 8850, Dec. 2020.

[6] S. Bajpai *et al.*, "Application of Central Composite Design approach for removal of chromium (VI) from aqueous solution using weakly anionic resin : Modeling , optimization , and study of interactive variables," *J. Hazard. Mater.*, vol. 227–228, pp. 436–444, 2012.

[7] I. H. Cho and K. D. Zoh, "Photocatalytic degradation of azo dye (Reactive Red 120) in TiO2/UV system: Optimization and modeling using a response surface methodology (RSM) based on the central composite design," *Dye. Pigment.*, vol. 75, no. 3, pp. 533–543, 2007.

[8] Y.-M. Chu and Q.-V. Bach, "Application of TiO2 nanoparticle for solar photocatalytic oxidation system," *Appl. Nanosci.*, no. 0123456789, Nov. 2020.

[9] N. Babajani and S. Jamshidi, "Investigation of photocatalytic malachite green degradation by iridium doped zinc oxide nanoparticles: Application of response surface methodology," *J. Alloys Compd.*, vol. 782, pp. 533–544, 2019.

[10] Z. Ghasemi, H. Younesi, and A. A. Zinatizadeh, "Preparation, characterization and photocatalytic application of TiO2/Fe-ZSM-5 nanocomposite for the treatment of petroleum refinery wastewater: Optimization of process parameters by response surface methodology," *Chemosphere*, vol. 159, pp. 552–564, 2016.

[11] S. Senobari and A. Nezamzadeh-Ejhieh, "A p-n junction NiO-CdS nanoparticles with enhanced photocatalytic activity: A response surface methodology study," *J. Mol. Liq.*, vol. 257, pp. 173–183, 2018.

[12] S. M. Ghoreishian, K. Badii, M. Norouzi, and K. Malek, "Effect of cold plasma pre-treatment on photocatalytic activity of 3D fabric loaded with nano-photocatalysts: Response surface methodology," *Appl. Surf. Sci.*, vol. 365, pp. 252–262, 2016.

[13] Y. AlSalka, A. Hakki, J. Schneider, and D. W. Bahnemann, "Co-catalyst-free photocatalytic hydrogen evolution on TiO2: Synthesis of optimized photocatalyst through statistical material science," *Appl. Catal. B Environ.*, vol. 238, no. June, pp. 422–433, Dec. 2018.

[14] P. S. Thind, D. Kumari, and S. John, "TiO2/H2O2 mediated UV photocatalysis of Chlorpyrifos: Optimization of process parameters using response surface methodology," *J. Environ. Chem. Eng.*, vol. 6, no. 3, pp. 3602–3609, 2018.

[15] S. Merabet, D. Robert, J. V. Weber, M. Bouhelassa, and S. Benkhanouche, "Photocatalytic degradation of indole in UV/TiO2: Optimization and modelling using the response surface methodology (RSM)," *Environ. Chem. Lett.*, vol. 7, no. 1, pp. 45–49, 2009.

[16] M. Moztahida and D. S. Lee, "Photocatalytic degradation of methylene blue with P25/graphene/polyacrylamide hydrogels: Optimization using response surface methodology," *J. Hazard. Mater.*, vol. 400, p. 123314, 2020.

[17] C. Betianu, F. A. Caliman, M. Gavrilescu, I. Cretescu, C. Cojocaru, and I. Poulios, "Response surface methodology applied for Orange II photocatalytic degradation in TiO 2 aqueous suspensions," *J. Chem. Technol. Biotechnol.*, vol. 83, no. 11, pp. 1454–1465, 2008.

[18] S. Abbasi, "Photocatalytic activity study of coated anatase-rutile titania nanoparticles with nanocrystalline tin dioxide based on the statistical analysis," *Environ. Monit. Assess.*, vol. 191, no. 4, p. 206, 2019.

[19] M. Choquette-Labbé, W. A. Shewa, J. A. Lalman, and S. R. Shanmugam, "Photocatalytic degradation of phenol and phenol derivatives using a Nano-TiO2 catalyst: Integrating quantitative and qualitative factors using response surface methodology," *Water (Switzerland)*, vol. 6, no. 6, pp. 1785–1806, 2014.

[20] H. Derikvandi and A. Nezamzadeh-Ejhieh, "A comprehensive study on enhancement and optimization of photocatalytic activity of ZnS and SnS2: Response Surface Methodology (RSM), n-n heterojunction, supporting and nanoparticles study," *J. Photochem. Photobiol. A Chem.*, vol. 348, pp. 68–78, 2017.

[21] J. Zhang, D. Fu, Y. Xu, and C. Liu, "Optimization of parameters on photocatalytic degradation of chloramphenicol using TiO_2 as photocatalyist by response surface methodology," *J. Environ. Sci.*, vol. 22, no. 8, pp. 1281–1289, 2010.

[22] M. Vaez, A. Zarringhalam Moghaddam, and S. Alijani, "Optimization and modeling of photocatalytic degradation of azo dye using a response surface methodology (RSM) based on the central composite design with immobilized Titania nanoparticles," *Ind. Eng. Chem. Res.*, vol. 51, no. 11, pp. 4199–4207, 2012.

[23] S. Mosleh, M. R. Rahimi, M. Ghaedi, K. Dashtian, and S. Hajati, "Sonochemical-assisted synthesis of $CuO/Cu_2O/Cu$ nanoparticles as efficient photocatalyst for simultaneous degradation of pollutant dyes in rotating packed bed reactor: LED illumination and central composite design optimization," *Ultrason. Sonochem.*, vol. 40, no. July 2017, pp. 601–610, 2018.

[24] A. A. Salarian *et al.*, "N-doped TiO2 nanosheets for photocatalytic degradation and mineralization of diazinon under simulated solar irradiation: Optimization and modeling using a response surface methodology," *J. Mol. Liq.*, vol. 220, pp. 183–191, 2016.

[25] P. Bindu and S. Thomas, "Estimation of lattice strain in ZnO nanoparticles: X-ray peak profile analysis," *J. Theor. Appl. Phys.*, vol. 8, no. 4, pp. 123–134, 2014.

[26] V. Mote, Y. Purushotham, and B. Dole, "Williamson-Hall analysis in estimation of lattice strain in nanometer-sized ZnO particles," *J. Theor. Appl. Phys.*, vol. 6, no. 1, p. 6, 2012.

[27] I. W. Sutapa, A. Wahid Wahab, P. Taba, and N. L. Nafie, "Dislocation, crystallite size distribution and lattice strain of magnesium oxide nanoparticles," *J. Phys. Conf. Ser.*, vol. 979, no. 1, p. 012021, 2018.

[28] M. Vashista and S. Paul, "Correlation between full width at half maximum (FWHM) of XRD peak with residual stress on ground surfaces," *Philos. Mag.*, vol. 92, no. 33, pp. 4194–4204, 2012.

[29] K. T. Drisya, M. S. López, J. J. R. Ramírez, J. C. D. Álvarez, and A. Rousseau, "Electronic and optical competence in the photocatalytic processes," pp. 1–16, 2020.

[30] S. Bagwasi, Y. Niu, M. Nasir, B. Tian, and J. Zhang, "The study of visible light active bismuth modified nitrogen doped titanium dioxide photocatlysts: Role of bismuth," *Appl. Surf. Sci.*, vol. 264, pp. 139–147, 2013.

[31] A. A. Badawy and S. M. Ibrahim, "The influence of La2O3-doping on structural, surface and catalytic properties of nano-sized cobalt–manganese mixed oxides," *Int. J. Ind. Chem.*, vol. 7, no. 3, pp. 287–296, 2016.

[32] Y. S. Tamgadge, P. P. Gedam, R. P. Ganorkar, M. A. Mahure, V. G. Pahurkar, and G. G. Muley, "Synthesis and characterization of Ni doped ZnO nanoparticles," in *AIP Conference Proceedings*, 2018, vol. 1953, p. 030003,2015.

[33] A. M. Bashi, M. Z. Hussein, Z. Zainal, M. Rahmani, and D. Tichit, "Simultaneous intercalation and release of 2,4-dichloro- and 4-chloro-phenoxy acetates into Zn/Al layered double hydroxide," *Arab. J. Chem.*, vol. 9, no. March, pp. S1457–S1463, 2016.

[34] N. Jafari, A. Ebrahimi, K. Ebrahimpour, and A. Abdolahnejad, "Optimization and Modeling of Microcystin-LR Degradation by TiO2 Photocatalyst Using Response Surface Methodology," *J. Environ. Heal. Sustain. Dev.*, vol. 5, no. 3, pp. 1063–1076, 2020.

[35] H. Baniamerian, P. Tsapekos, M. Alvarado-Morales, S. Shokrollahzadeh, M. Safavi, and I. Angelidaki, "Anti-algal activity of Fe2O3–TiO2 photocatalyst on Chlorella vulgaris species under visible light irradiation," *Chemosphere*, vol. 242, p. 125119, 2020.

[36] A. Wold, "Photocatalytic Properties of TiO2," *Chem. Mater.*, vol. 5, no. 3, pp. 280–283, 1993.

M. Miranzadeh, F. Afshari, B. Khataei, and M. Z. Kassaee, “Adsorption and Photocatalytic Removal of Arsenic from Water by a Porous and Magnetic Nanocomposite: Ag/TiO2/Fe3O4@GO,” *Adv. J. Chem. A*, vol. 3, no. 4, pp. 408–421, 2020.

[37] B. Rahimi and A. Ebrahimi, “Photocatalytic process for total arsenic removal using an innovative BiVO4/TiO2/LED system from aqueous solution: Optimization by response surface methodology (RSM),” *J. Taiwan Inst. Chem. Eng.*, vol. 101, no. xxxx, pp. 64–79, 2019.

[38] A. Samad, M. Furukawa, H. Katsumata, T. Suzuki, and S. Kaneco, “Photocatalytic oxidation and simultaneous removal of arsenite with CuO/ZnO photocatalyst,” *J. Photochem. Photobiol. A Chem.*, vol. 325, pp. 97–103, 2016.

[39] V. Vaiano, G. Iervolino, and L. Rizzo, “Cu-doped ZnO as efficient photocatalyst for the oxidation of arsenite to arsenate under visible light,” *Appl. Catal. B Environ.*, vol. 238, no. July, pp. 471–479, 2018.

[40] Y. Wang, J. Duan, W. Li, S. Beecham, and D. Mulcahy, “Aqueous arsenite removal by simultaneous ultraviolet photocatalytic oxidation-coagulation of titanium sulfate,” *J. Hazard. Mater.*, vol. 303, pp. 162–170, 2016.

[41] W. Liu, X. Zhao, A. G. L. Borthwick, Y. Wang, and J. Ni, “Dual-Enhanced Photocatalytic Activity of Fe-Deposited Titanate Nanotubes Used for Simultaneous Removal of As(III) and As(V),” *ACS Appl. Mater. Interfaces*, vol. 7, no. 35, pp. 19726–19735, 2015.

[42] H. Eslami *et al.*, “Efficient photocatalytic oxidation of arsenite from contaminated water by Fe2O3-Mn2O3 nanocomposite under UVA radiation and process optimization with experimental design,” *Chemosphere*, vol. 207, pp. 303–312, 2018.

CHAPTER. 5

Deposition, characterization and PC application of RF-sputter deposited TO/BVO films

The pristine compounds and their nanocomposites synthesized by the sol-gel methodology were processed as targets for the deposition of composite and layered films. The RF-sputtering deposition of TO/BVO heterostructures was carried out under variable parameters such as the RF-power, partial pressure, substrate nature and temperature. The deposition technique does not require temperature, but mainly make use of the Ar+ high energy bombardment of the target atoms and their further transfer onto a substrate surface [1]. The main goal of our experimental work is to deal with the optimization of the deposition conditions to ensure films with good crystalline quality and optical absorbance required for highly efficient photocatalyst. Moreover, the nature of the substrate plays a crucial role in the crystalline quality, stability and adhesion of the deposited films. Thus, two different substrates were selected consist of, boroflat glass (BK7) and alumino- phosphate (AlPO) ceramic substrates. BK7 remained stable up to 550°C. Since the temperature range of 550 to 600°C was necessary to have the grain growth. Two configurations of the deposited films were considered. Nanocomposites films were made by target made from sol-gel synthesized TO/BVO nanocomposites. The second type consist of layers of BVO deposited on the substrate and covered by a TO layer. This organization allows efficient visible light harvesting for the pc reactions since the TO is an optically transparent layer.

5.1 Optimization of the parameters:

The sputtering is carried out under different parameters. This includes deposition chamber atmosphere, RF-power and post-deposition annealing temperature. The rate of deposition defines the thickness and compactness of the films and the annealing required for the improvement of structural features of the films. A 20 minutes pre-sputtering of the target was performed before each deposition to avoid the surface contaminations [2]. and these process parameters were optimized and their further characterizations were carried out. The parameters include;

- RF- Power
- Chamber atmosphere and substrate temperature
- Annealing temperature of the deposited film

On the other hand, beyond the kinetic energy of the incident species [3], the adhesion of the film over the substrates is influenced by different factors including the nature of the substrate, its organisation and stability to the temperature of deposition and post-deposition annealing. The film quality and performance has very much dependence over these above-mentioned parameters [4]. The annealing was done at 5^{o}C/min rate of heating and further cooling was also carried out at the same rate [5].

Initially the target with the stoichiometry 0.5:0.5 TO/BVO was processed and deposited on BK7 and AlPO substrates. The AlPO substrate requires a careful analysis due to its intense xrd pattern as illustrated below (fig.5.1). The identification of the peaks of the AlPO substrate is carried out comparing with standard JCPDS-01-072-1161 for aluminium phosphate material(fig.5.1)

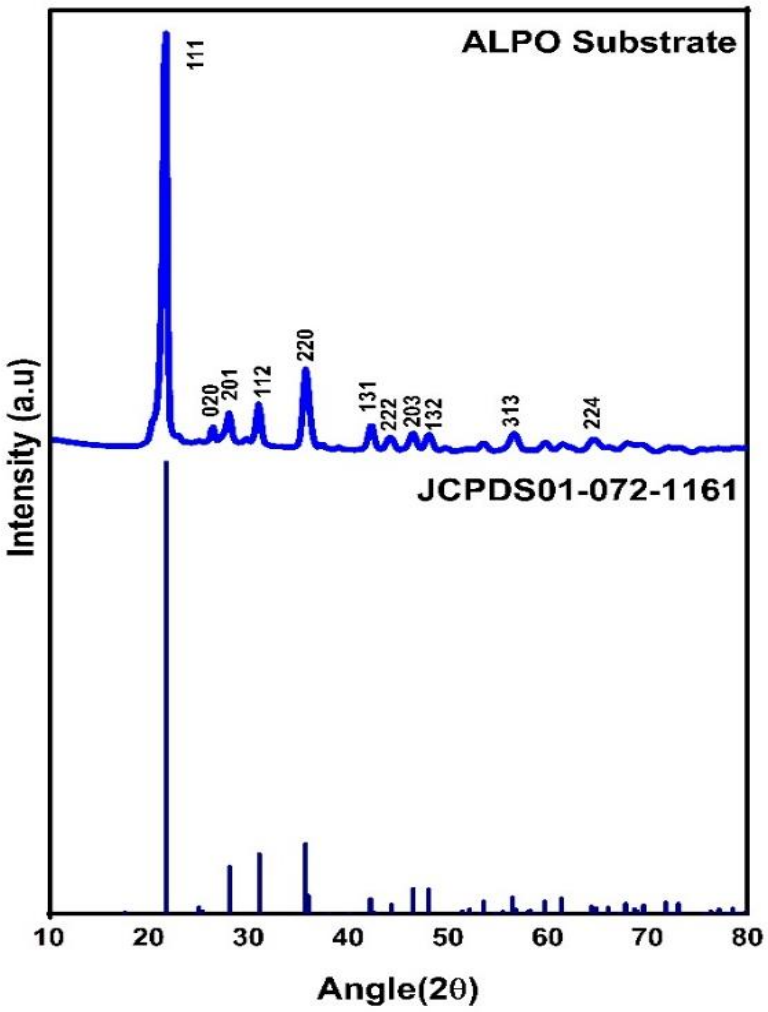

Fig. 5.1 X-ray diagram for the identification of the AlPO Ceramic substrate material

5.1.1 Effects of the chamber atmosphere and substrate temperature

The sol-gel synthesized composite films on BK7 substrate were deposited from the target with 0.5:05 ratio of TO/BVO. The deposition parameters were changed and consist of the driven gas (Argon+ Oxygen and pure Ar) and the substrate temperature. The features of the driven gas (pressure and composition) affect the sputtering rate as well as the morphology and crystallinity of the deposited films.

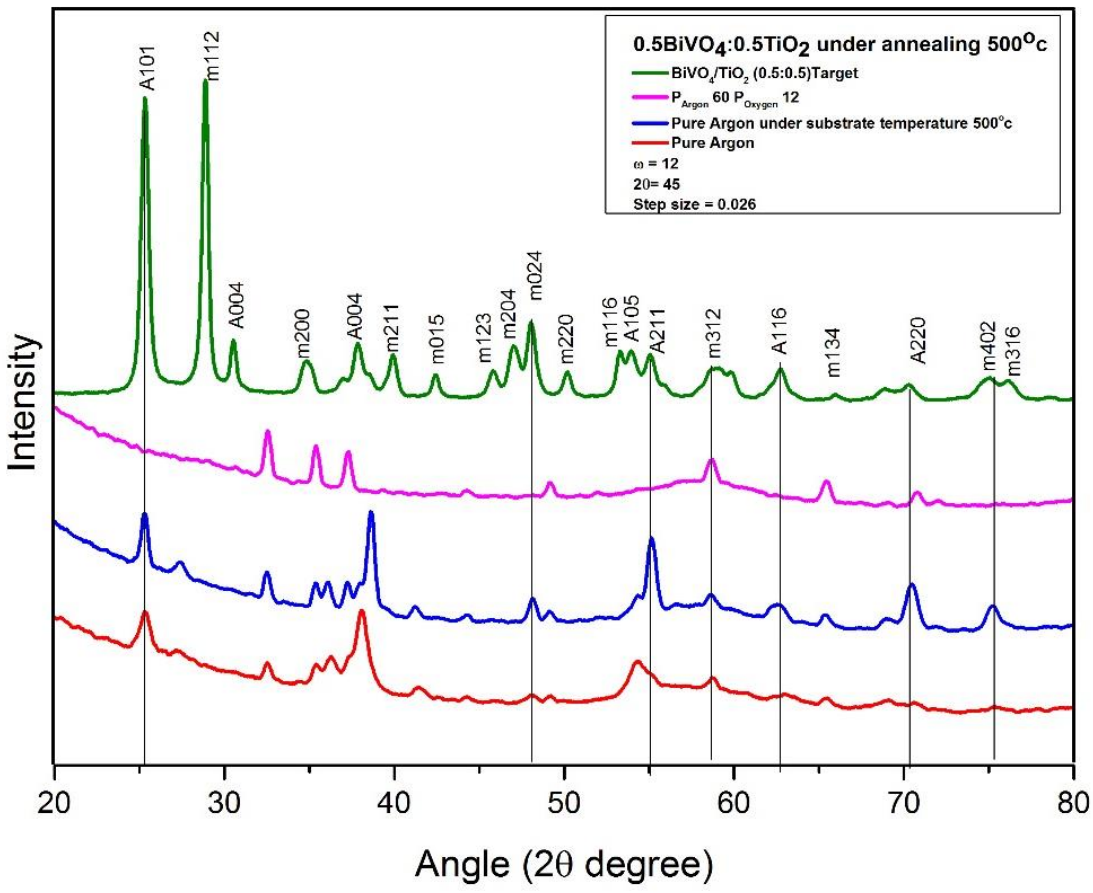

Fig. 5.2 X-ray diagrams of the composite film deposited under different chamber atmosphere

The comparative xrd patterns in the fig.5.2 show crystalline peaks from the diffractions corresponding to the planes with orientation along a(101) and m(312). Both anatase TO and monoclinic phase of BVO was present. The synthesized films were annealed after deposition of 2 hours at 500°C in order to obtain good crystalline films. As it can be seen in fig 5.2, the best deposition with good crystalline quality is obtained under pure Ar along with a substrate heating at 500°C. Post deposition annealing for 2 hours for the proper crystal growth which yield same results, for the depositions with and without the substrate heating. Hence to have

lesser energy consumption during the processes, we have chosen the Ar alone condition without substrate heating.

5.1.2 Effect of RF- power

The second sets of parameters under investigation was the effect of variable RF-sputtering powers in order to define the optimum value required for deposition of films with well-defined crystalline structures tracing both constituents BVO and TO. Targets composed by TO/BVO in the ratio 0.5:0.5 were used along with argon in the deposition chamber where the pressure is fixed at 5.10^{-2} mbar. The preliminary deposition was carried out for 2 hours to ensure a suitable thickness of the film even with the lowest RF-power. Three different power with the values 25, 50 and 75 w were used to synthesize the composite films. The interaction between the target atoms and substrate can be depended upon the energy of the atoms that further depends upon the RF-power [6]. Also, the adhesion of films on the substrate has strong dependence on the sputtering power [7].

Xrd analysis was carried out on different samples annealed at 550°C and the patterns are summarized in fig. 5.4. At 25 W. gives rise to crystalline films but the diffraction peak intensity is not well resolved for the desired diffraction peaks compared to the JCPDS cards for BVO (JCPDS14-0688) [8] and (JCPDS 21-1272) for TO [9]. By increasing the power to 50 W, there observed an enhancement in the xrd line intensities and the resolution of the pattern is well resolved with the m- BVO and TO diffractions. The higher power at 75 W the diffraction intensities of the peaks are not appreciable as that at 50W. At 25W, the power seems to be not enough to reach the atoms on to the substrate surface and at 75W, the higher power seemed to cause the loss due to higher collision. Thus, the xrd patterns point out the optimal power at 50 W to ensure the deposition of films with good crystalline features.

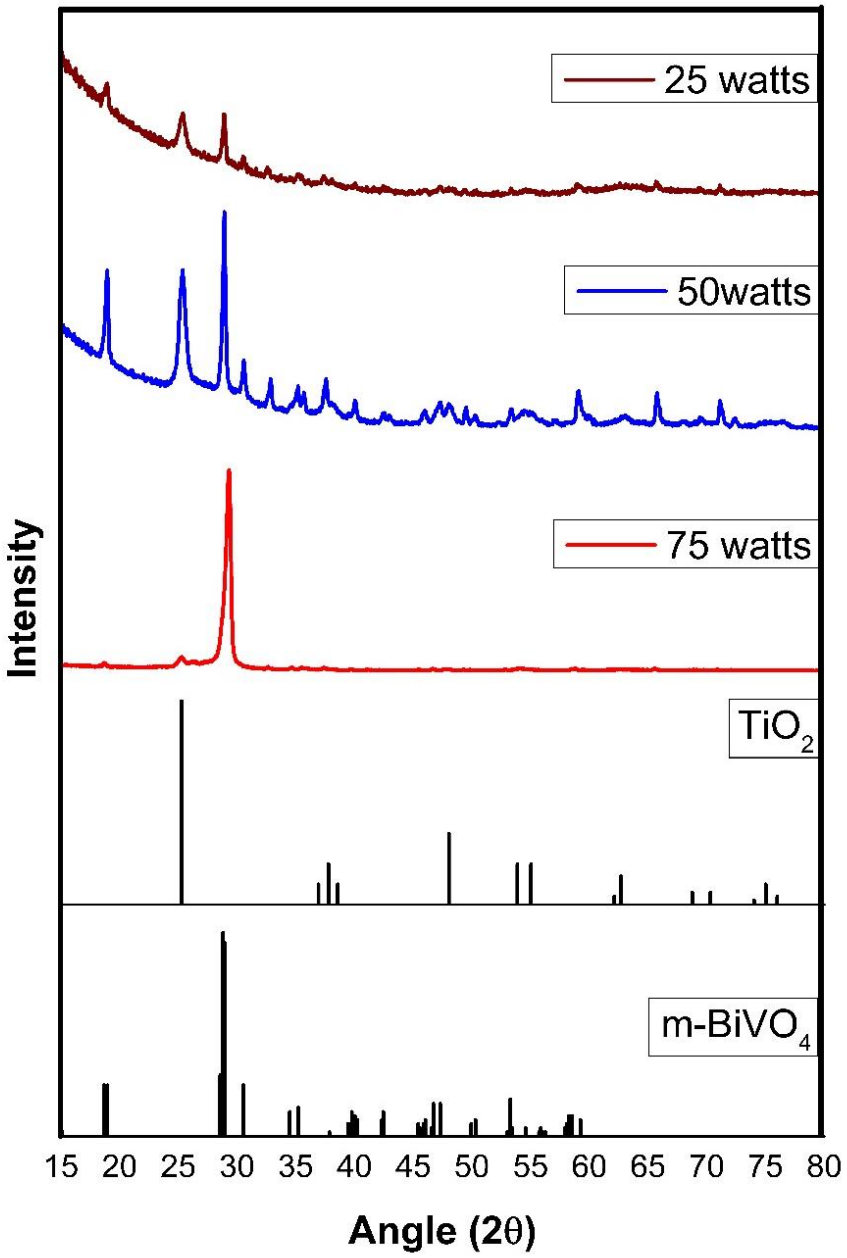

Fig. 5.3 X-ray diagram of the nanocomposite deposited at different incident power

5.1.3 Post annealing in-situ temperature treatment

The RF-sputtering method is versatile and easy for processing different configurations of single or multi-layer films. However, post-synthesis annealing is required to improve the crystalline quality of the samples. By using a cryostat mounted on xrd diffractometer, the optimal temperature of annealing under ambient atmosphere was found out from the features of the in-situ xrd patterns. The xrd patterns in fig. 5.5 show the development of the required polymorphs for BVO and TO from the temperature of 550°C. From the diffractogram it can be inferred that, the crystalline quality is improved during heating from 550 to 650°C. Thus,

550°C corresponds to the minimum value for the annealing temperature to ensure the required crystal structure. This value of the annealing temperature is suitable for further depositions as discussed below.

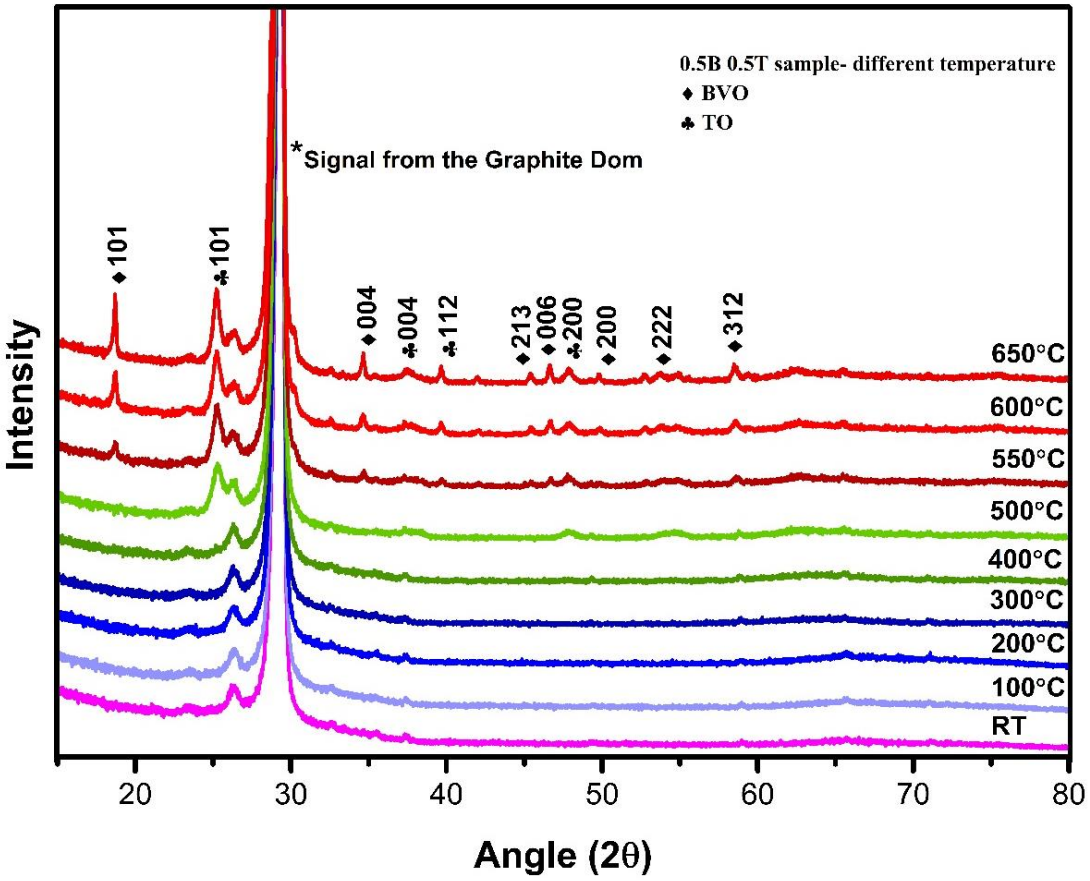

Fig. 5.4 In-situ annealing X-ray diagrams of the nanocomposite film (Optimization of the annealing temperature)

5.2 X-ray Diffraction analysis; Substrate effects on the deposited films

It is well known that in deposition of films, the substrate nature plays a crucial role in the quality and physical characteristics of the deposited films [10-13]. In this context, the present work analyses the effects of different substrates on the structural, morphological, and pc properties of heterostructures based on TO/BVO. The RF-sputtering deposition was made as composite films made from TO/BVO nanocomposite target and as layered films with TO/BVO /substrate structure. The nanocomposite films deposited for 10 hours possess a thickness of around 4.8 µm, i.e., the deposition rate of 480 nm/hour. For the layered films with a thickness of around 2 µm, the deposition rate is about 200 nm/hour. Sch thickness contains enough photoactive matter required for efficient pc process.

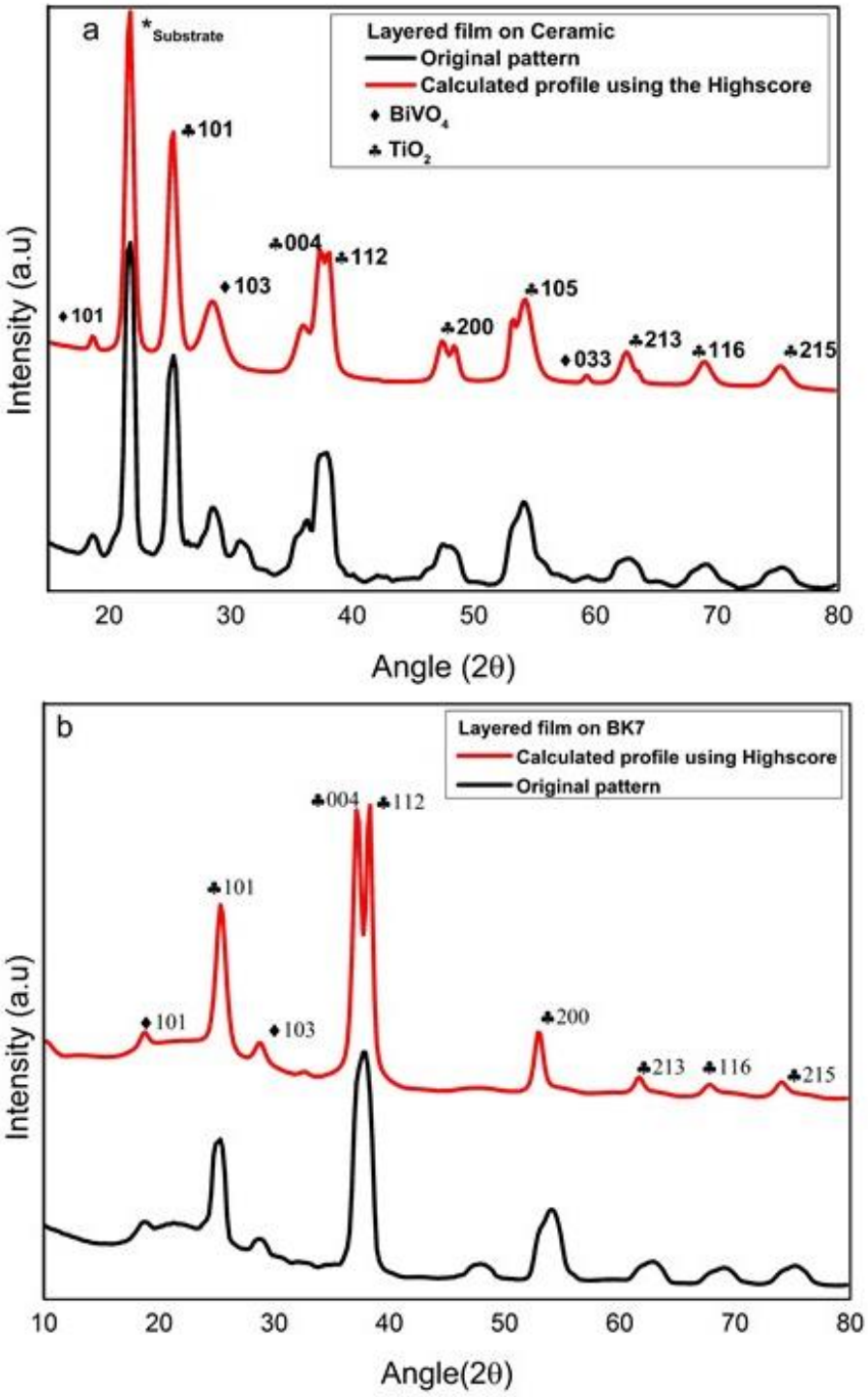

Fig. 5.5. X-ray diagram of the layered films over a) Ceramic and b) BK7 substrates compared to the fitted data from High score software.

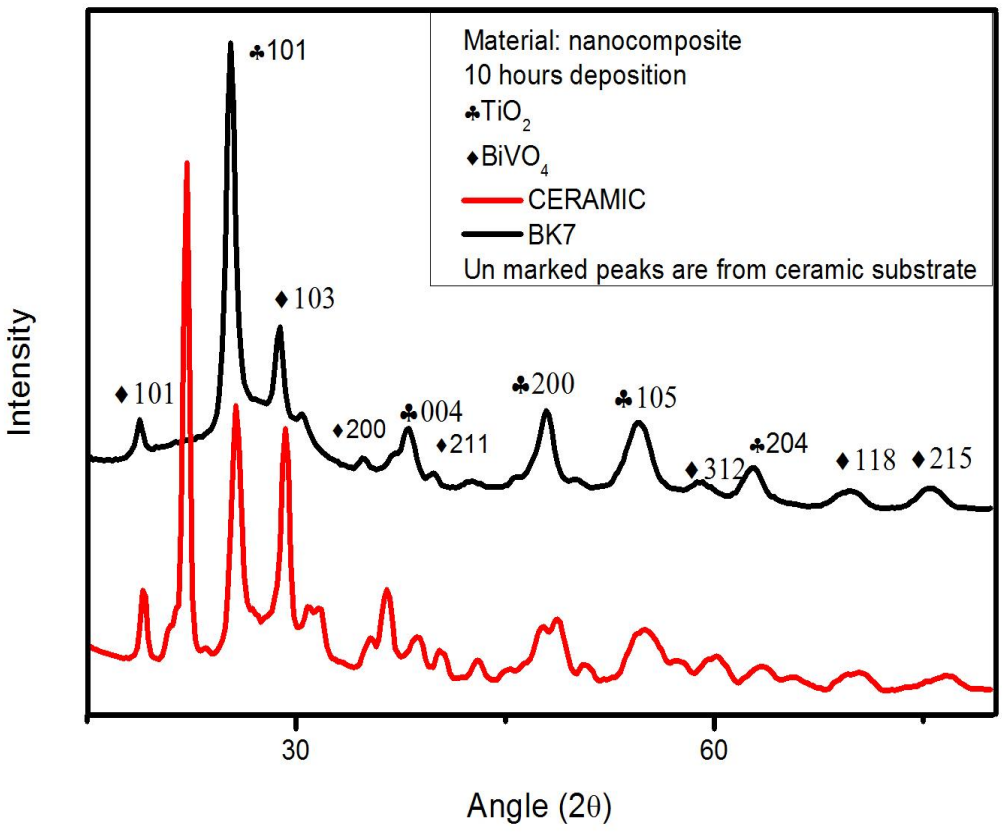

Fig. 5.6. X-ray diagrams of the Nanocomposite films deposited on Ceramic and BK7 substrates with the assignment of the xrd lines to well defined crystalline structures.

Table. 5.1 Structural parameter of the films.

Samples	**Average Crystallite Size (nm)**	**Average Lattice Strain**	**Dislocation density (*10^{-3} nm^{-2})**
Layered film- BK7	10.69	1.06	9.3
Layered film- Ceramic (AlPO)	11.44	0.9	8.2
Composite film- BK7	28.38	0.4	2.5
Composite film- Ceramic (AlPO)	12.91	0.9	6.6

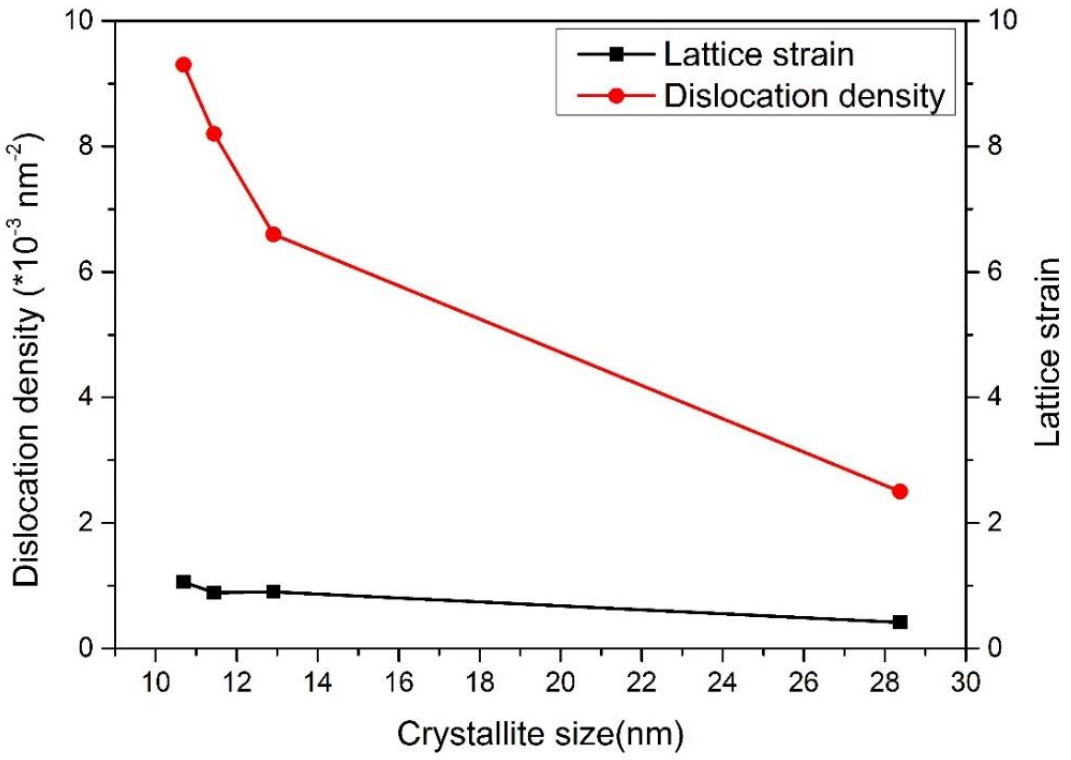

Fig. 5.7. Dislocation density and lattice strain vs. Crystallite size

Fig. 5.5 a and b reports the xrd patterns of the films deposited over the ceramic AlPO and BK7 substrates annealed at 600 and 550°C, respectively, considering the stability of the BK7 substrates at the annealing temperatures. The monoclinic BVO is involved in the films as indicated by the principal planes (101), (103) at the positions 2Θ = 18.67° and 28.6°. For TO, the anatase polymorph is also identified with (101), (004), and (200) crystallographic planes at 2Θ = 25.28°, 37.8°, and 48.04° respectively. It can be seen that the deposited films are well crystallized with the TO and m- BVO phases. The crystallite size (D) has been calculated for each film by taking the average of all the peaks. Debye- Scherer formula was used for the crystallite size calculation [14];

$$\boldsymbol{D = \frac{0.9\lambda}{\beta Cos\theta}} \qquad (1)$$

Moreover, the crystallite size was estimated to 10.69 and 28.38 nm for the layered and composite films, respectively, on the BK7 substrates. The same evaluations were obtained for the films deposited over the ceramic substrate where the nanocrystalline domain sizes (D) are about 11.44 and 12.91nm for the layered and composite films, respectively (fig. 5.8). The lattice strain and dislocation density were also calculated for the deposited films (table.5.1).

For the calculation of dislocation density, we used the following formula [15, 16]:

$$\boldsymbol{\delta = \frac{1}{D^2}} \qquad (2)$$

It seems that the films with higher lattice strain show higher dislocation densities, which correlate with the observed broadening of the diffraction peaks. It was also observed that the layered films exhibit higher dislocation densities in the order of 9.3 and 8.2 for the layered films deposited over BK7 and AlPO substrates, respectively. The dislocation density decreased with increased crystallite size (fig.5.7), leading to increased lattice strain [17,18]. The percentage fraction of each structures in the films from BVO and TO phases in both layered and composite films were calculated using the equation [10];

The intensity mentioned is the integrated intensity (I_{int}) of the peaks, which is calculated for regular (Lorentzian or Gaussian line) as:

$$\boldsymbol{I_{int} = I.D^2} \quad (3)$$

Where D is the line width of the diffraction peak with the intensity (height) I

The Fraction of BVO was estimate from the integrated intensities as follows

$$\boldsymbol{\eta_{BVO} = 100.\frac{I_{int_{BVO}}}{(I_{int_{BVO}} + I_{int_{TO}})}} \qquad (4)$$

In similar way, the fraction of TO phase is defined as:

$$\boldsymbol{\eta_{TO} = 100 - \eta_{BVO}} \qquad (5)$$

Table.5.2 Percentage Composition of BVO & TO calculated using the integrated intensity of the peaks

Film sample	**% BVO**	**% TO**
Layered film- BK7	37.13	62.87
Layered film- Ceramic (AlPO)	28.51	71.49
Composite film- BK7	33.89	66.11
Composite film- Ceramic (AlPO)	35.43	64.57

From the table, it is found that, for the layered films, the percentages of BVO and TO are similar irrespective of the substrate nature. For all the films, almost the same order of magnitude of percentage composition is is found. Indeed, the layered films exhibit an

average composition of about 27% of BVO and 73% of TO, while for the composite films, the average percentages are 34% BVO and 66% TO.

5.3 Raman Analysis

Raman investigations were carried out on TO/BVO heterostructures as illustrated by the spectra reported in fig. 5.8-5.9. The raman active modes are in agreement with the desired monoclinic BVO and anatase TO phases. The most intense raman band at 821 cm^{-1} is assigned to the A_g mode of the BVO and corresponds to the symmetric stretching of V-O bonds in VO_4^{3-} units. The raman bands of both TO and BVO are present. A_{1g} and B_{1g} vibrations at 518 and 397 cm^{-1}, respectively, and the E_g modes at 145, 195, and 638 cm^{-1} were observe corresponding to TO [19]. The well resolved raman bands indicate the good crystalline nature of the deposited films [20,21]. In the layered films, the raman band intensities are more intense for the ceramic substrates than the films grown on BK7 substrates. The possible reason lies in the optical transparency of the BK7 substrate, which limits the reflected laser radiation and then the scattered collected light. This difference in raman band intensities is more pronounced for layered films with a small thickness (~2 µm) than for composite films (~4.8 µm).

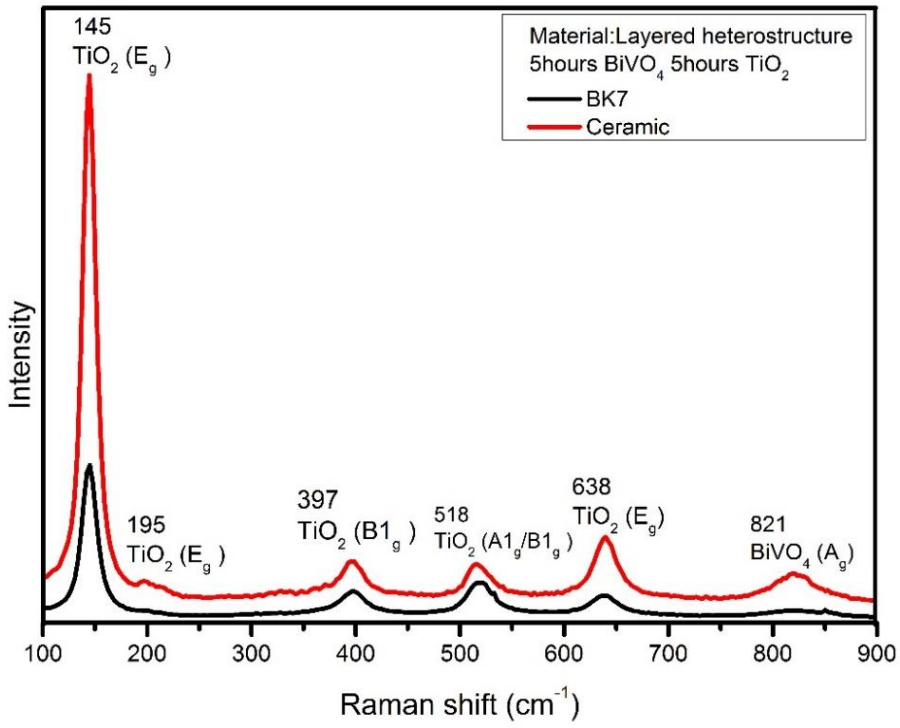

Fig. 5.8. Raman spectra of the layered films

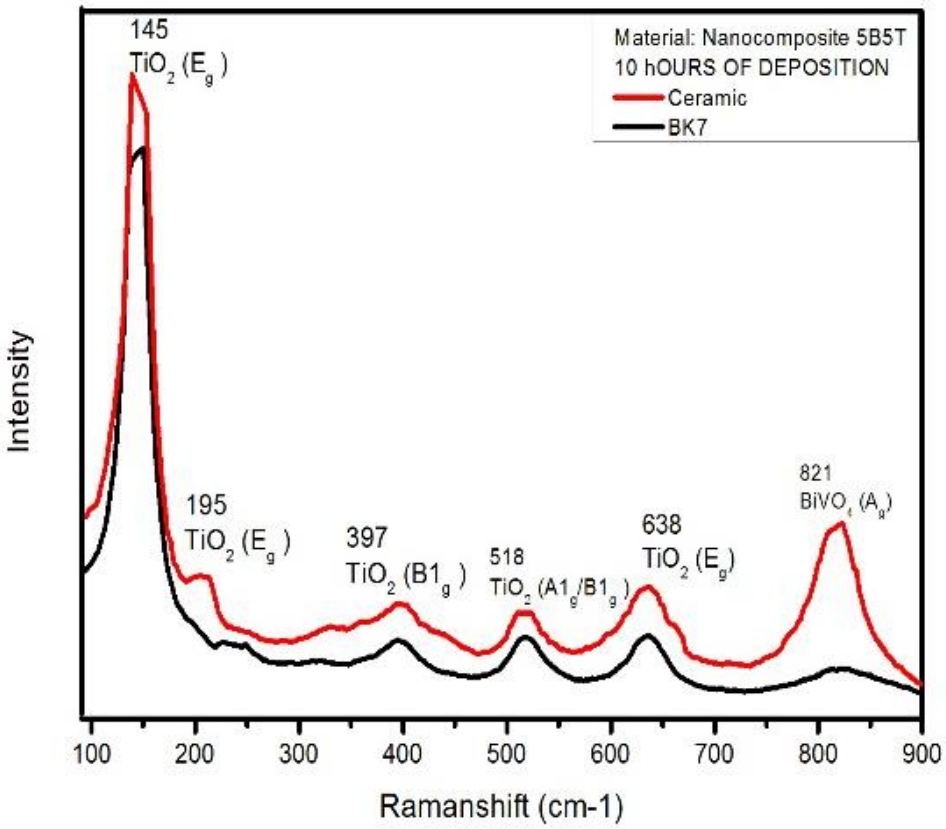

Fig. 5.9. Raman analysis of the nanocomposite films

It is worth noting the broad raman lines in the composite films compared to the narrower line shapes in the layered films. We attribute this difference to the interfaces TO/BVO area, which is higher in the composite films. In that case, the small crystalline domains of one constituent, such as BVO or TO, are surrounded by the other compound. The disorder at the interfaces and the surface reconstruction is expected to broaden the xrd patterns in composite films.

To sum up, the RF-sputtering synthesis of films in layered and composite configurations were realized. Optimal parameters were obtained for the film deposition and included the RF-power (50W), chamber atmosphere (Ar-without substrate heating) and the post-synthesis annealing (550-600^{o}C). The monoclinic polymorph for BVO and anatase for TO coexist in the different films and exhibit good crystalline attributes irrespective of the used substrates (BK7 glass, AlPO ceramic)

5.4 UV- Vis Band gap analysis

The Tauc-plot of the deposited films are reported [22, 23] in fig. 5.10 for the different compositions of the films as bare BVO, TO and the heterostructures TO/BVO realize in the layered and composite configurations.

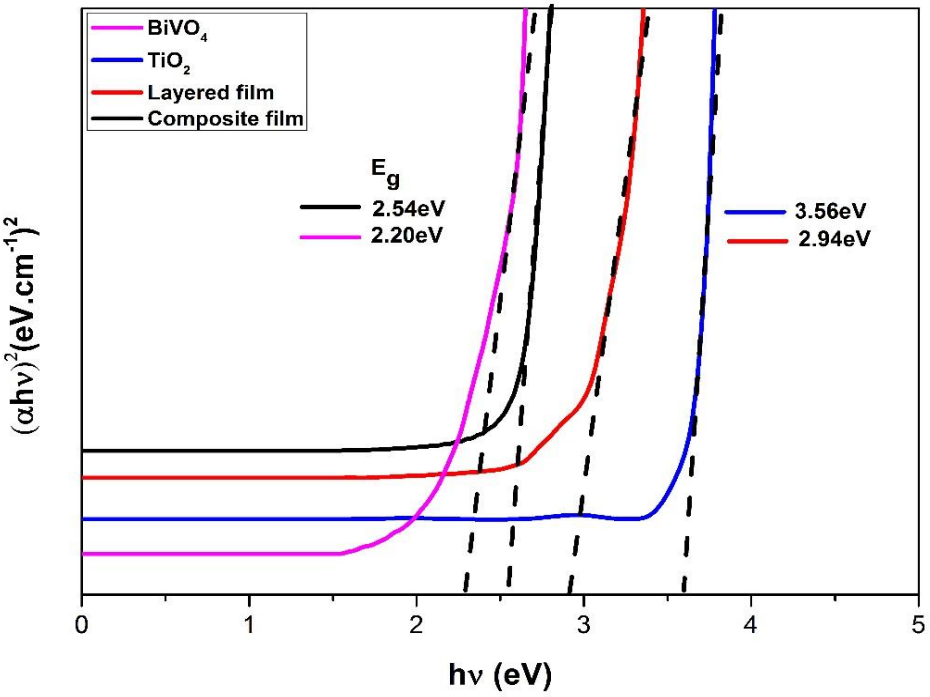

Fig. 5.10 Tauc- plot for the different RF-sputtered films with different compositions as BVO, TO, and TO/BVO heterostructures (composite and layered films) deposited over the BK7 substrate.

The band gap of TO was estimated to 3.56 eV which is higher than the generally reported, established value of 3.20 eV for anatase phase. A higher value of the band gap may be induced by quantum confinement effects [24] due to the nanosized crystalline domains. For the BVO film, the band gap was estimated to 2.20 eV in agreement with the values determined in other RF-sputtered films [25]. The optical absorption spectra of the TO/BVO heterostructures were recorded in the same conditions as for BVO and TO. The layered film shows a band gap in the order of 2.94 eV; i.e. closer to TO band gap. There are many such reports on the band gap shift towards the visible region during the association of materials of two different band gaps [26, 27]. In the case of nanocomposite film, there obtained a band gap of 2.54eV that comes in the visible region. The difference between the optical absorbance of composite and layered films can be explained by their respective microstructures. The layered film formed by separated constituents BVO and TO defines the

heterojunction TO/BVO. In contrast to this organization, the composite film is formed by segregated clusters of both BVO and TO; the heterostructure surface is then formed by multiple areas between the clusters. As the investigated heterostructures are devoted to be tested in heterogeneous photocatalysis, the efficiency of the process is dependent on the ratio of harvested light in the visible region of the solar spectrum. In this context, we may expect that the composite films are worthy of interest with respect to their low band gap (2.54 eV) compared to that of the layered film (2.94 eV). This hypothesis will be discussed in the next section related to the photocatalysis studies.

5.5 Transmission Electron Microscope (TEM) analysis

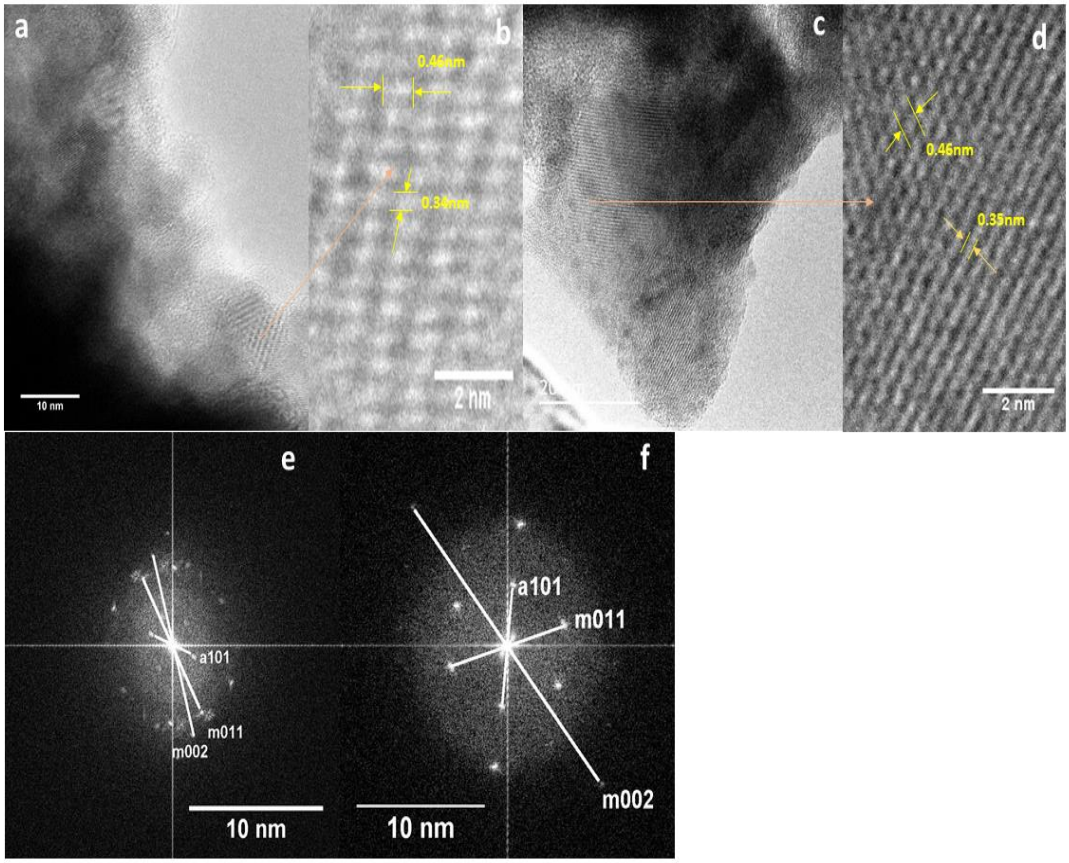

Fig. 5.11 TEM Micrograph of the films deposited over BK7 substrates a) Layered film b) Planes from the layered film c) Composite film d) Cropped planes from composite film e,f) FFT of the layered and composite films respectively

TEM micrographs for both films (layered and composite) deposited over BK7 and AlPO ceramic substrates are illustrated in fig. 5.11 and fig. 5.12 respectively. Fig. 5.11 a and b show the TEM micrographs of the layered and composite TO/BVO films deposited over the

BK7 substrate while fig. 5.11c and d illustrate their FFT images. The identified crystallographic planes are consistent with anatase TO and monoclinic BVO in agreement with standard JCPDS and further xrd analysis. Thus, FFT graphs show the plane (101) from TO phase superimposed to the planes (011) and (002) related to BVO structure. The inter reticular distance has been calculated and the 0.46nm was corresponding to the 011 plane of the BVO and the planes with an inter planar distance 0.34 and 0.35 (fig. 5.11 b and d) corresponds to the 101 planes from the TO.

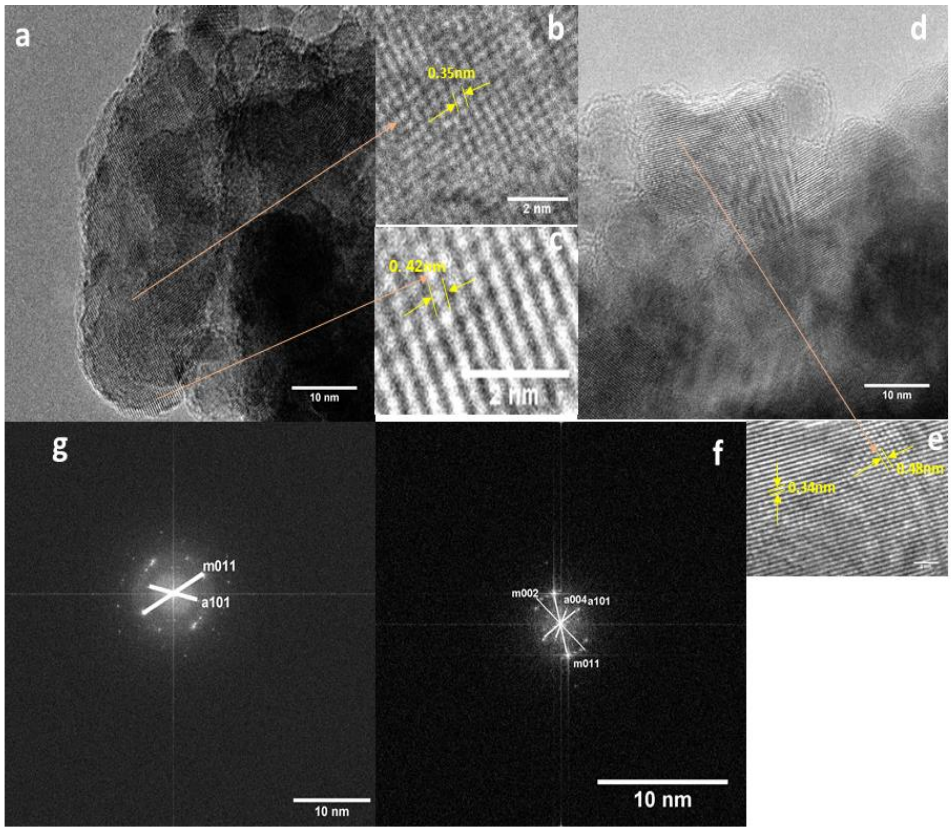

Fig. 5.12 TEM Micrograph of the films deposited over Ceramic substrates a) Layered film b,c)Cropped planes d) Composite ceramic film e) Cropped planes from the composite film f,g) FFT from the layered and composite films respectively

Fig. 5.12a and 5.12d also report the TEM micrographs of the layered and composite films respectively deposited over the AlPO ceramic substrate. Fig. 5.12c and d illustrate the FFT images of the micrographs where the same crystallographic planes of TO and BVO structures are involved as observed also observed for the films deposited over BK7 substrates. It is worth noting that irrespective of substrate nature and the film configuration (layered, composite), all TEM micrographs show nanocrystalline grains with well-defined boundaries.

The inter-reticular distance is calculated for both layered and composite films. It is found that, from fig. 5.12 b, the distance around 0.34nm corresponds to the 101 planes of TO existing in the layered and composite films respectively. From the fig. 5.12c, the distance of 0.42nm corresponds to the 011 plane of the m- BVO while from fig. 5.12e, the inter planar distance calculated at 0.48nm corresponds to the 101 planes of the m- BVO of the composite film. The grain size has been calculated for each film. And it is found that the composite films deposited on the BK7 substrate seem to have an average grain size of 19.33. Both the layered film on the BK7 substrate and Composite film on AlPO substrate possesses an average grain of 16nm and that of the layered film deposited on the AlPO substrate exhibited an average rain size of 15nm.

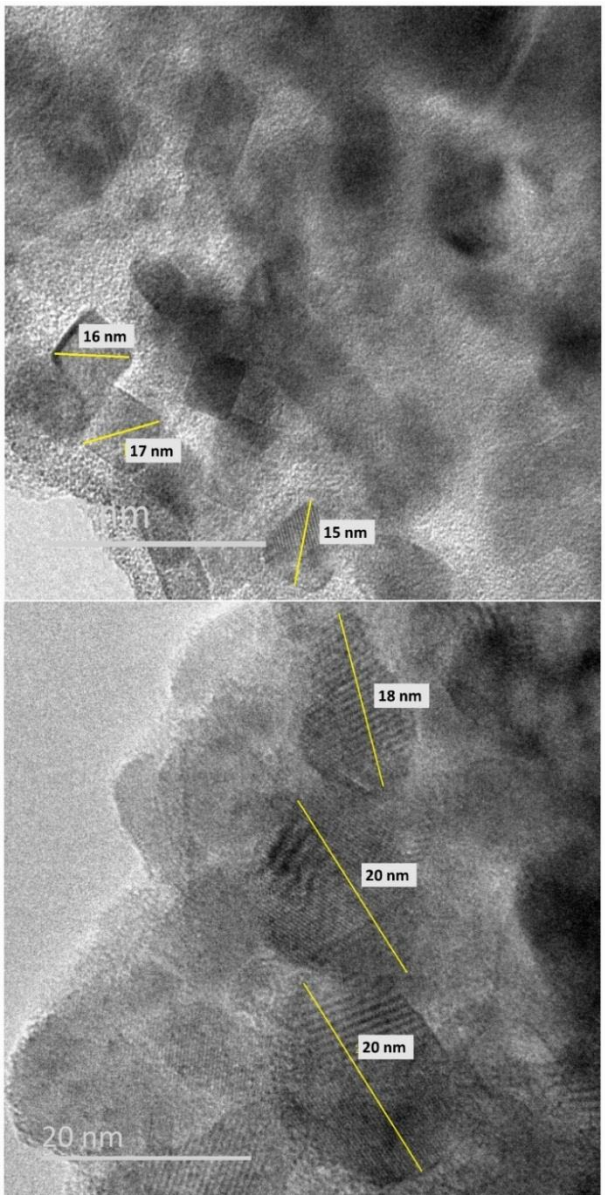

Fig. 5.13 a) Composite-BK7 b)Layered film-BK7

Table.5.3 Calculated grain size from TEM micrographs

Film type	**Average Grain size (nm)**
Composite film-BK7	19.3
Layered film-BK7	16
Composite film-Ceramic	16
Layered film-Ceramic	15

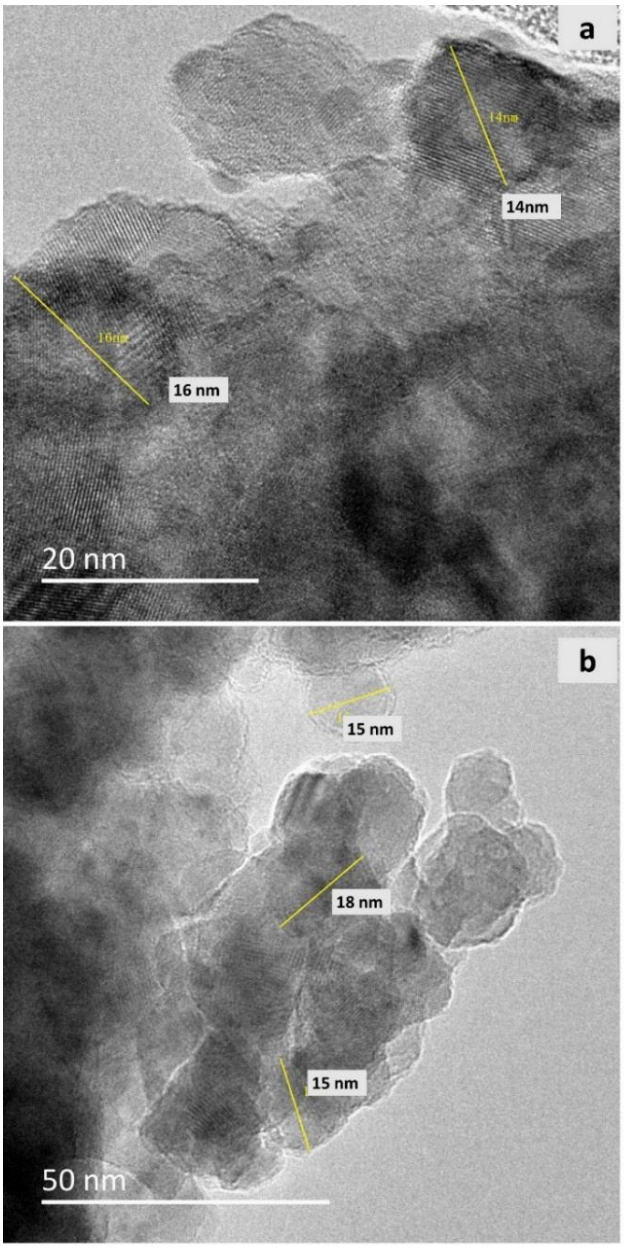

Fig. 5.14 c) Composite film-Ceramic substrate d) Layered film- Ceramic substrate

5.6 Profilometry analysis- Thickness measurement

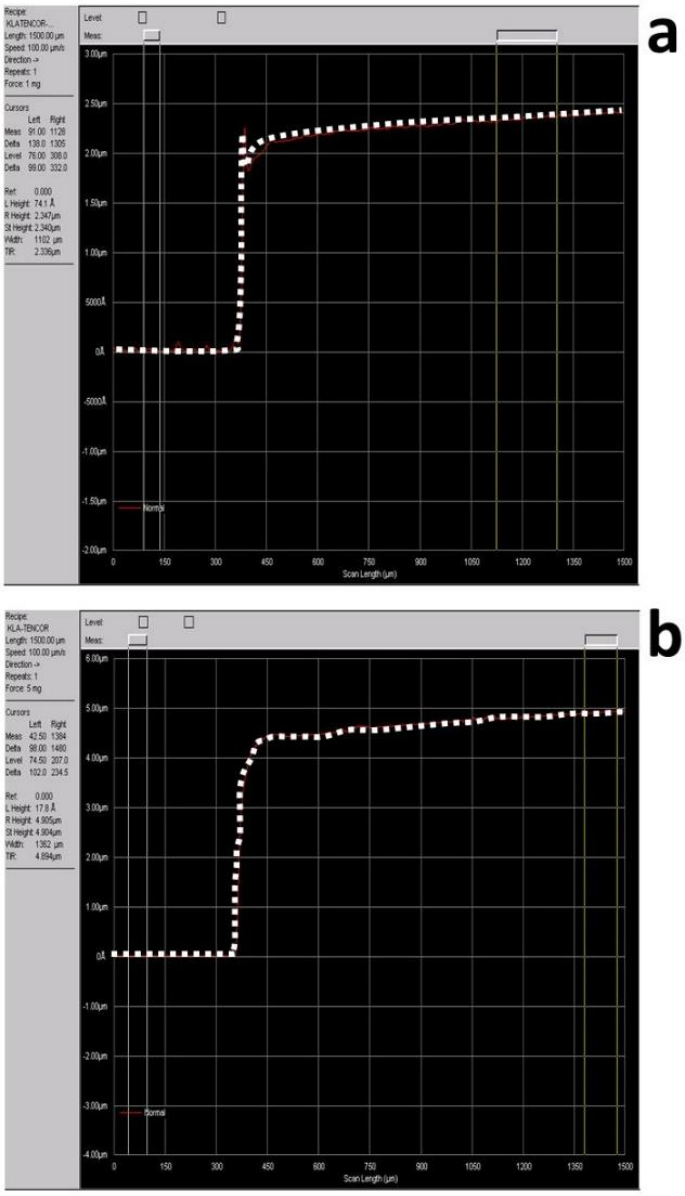

Fig. 5.15 a) Thickness measurement for the layered film b) Thickness measurement for the nanocomposite film

Both the ceramic and BK7 optical glass substrates have been used for the deposition of both types of films. The nanocomposite films deposited for 10 hours have a thickness around 4.5 micrometres (fig. 5.15b) and the films deposited as layered heterojunctions (fig. 5.15a) are with a thickness of around 2 micrometres. The deposition of the nanocomposite has been done for a continuous 10 hours and the rate of deposition of 450nm/hour. The deposition of the layered structure has been done in such a way that the rate of deposition of 200nm/hour.

5.7 Atomic Force Micrograph Analysis

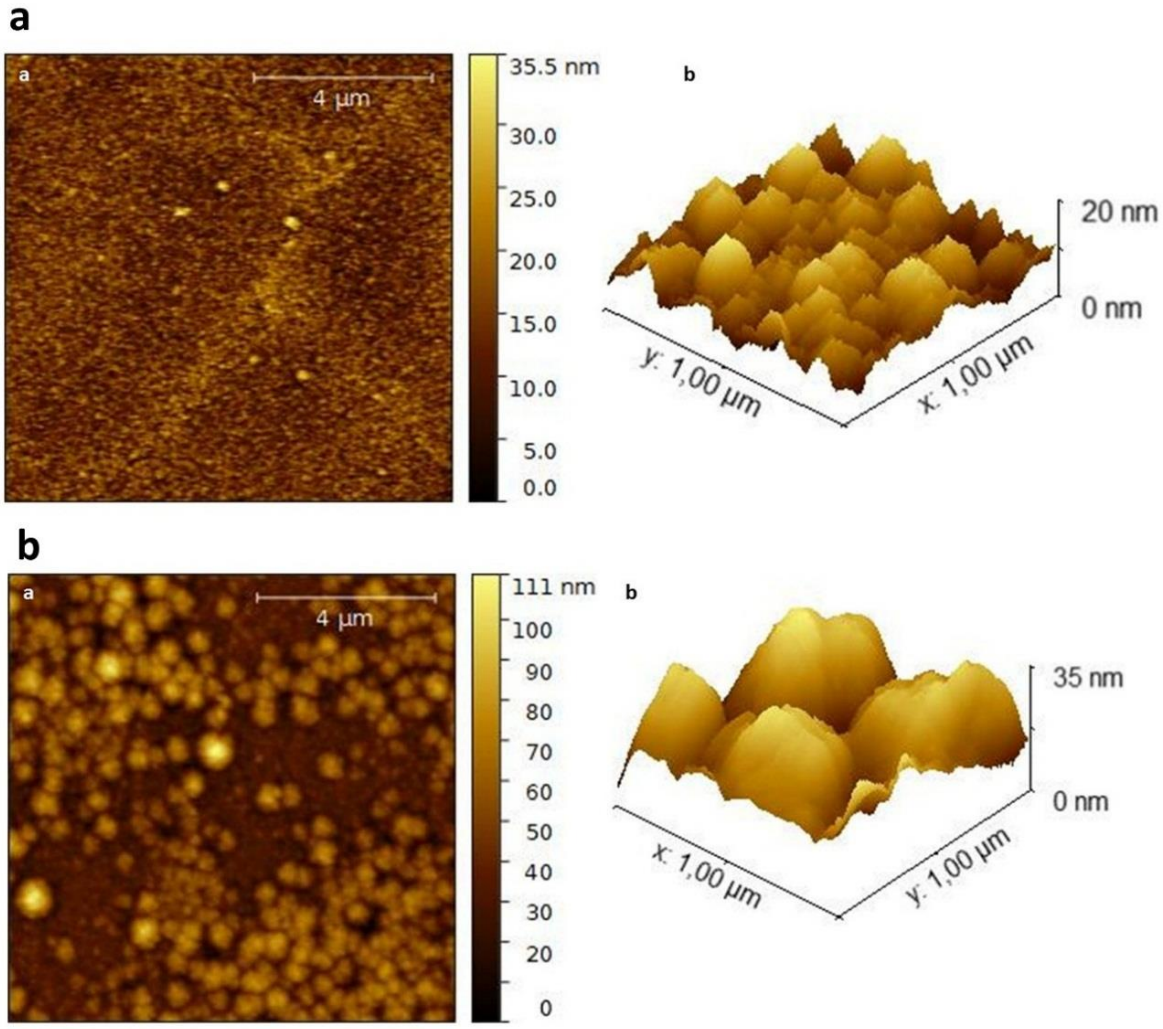

Fig. 5.16 a) Morphology of the layered film deposited on BK7 substrate by AFM- both a) 2D and b) 3D images, respectively, are illustrated **b**) Morphology of the composite film deposited on BK7 substrate by AFM- both a) 2D and b) 3D images, respectively

AFM micrographs of the films are given (fig. 5.16 a & b) two- and three-dimensional view of the surface is illustrated above. Several surface profile parameters can be estimated and account for the roughness and grain sizes. The film roughness was evaluated to be 12 nm for the composite film and for the layered film, a smaller roughness value of 3.6 nm was estimated. This higher roughness of the composite film can be due to its comparatively higher grain size [28]. Concerning the grain sizes smaller in the layered and composite films, we expect a higher contact area of the layered films with their surrounding environment compare to the composite ones. The surface seemed to be nano islands and these structures

reported to increase the surface area and hence contributes towards the efficient photocatalysis [5].

5.8 Photocatalytic degradation test

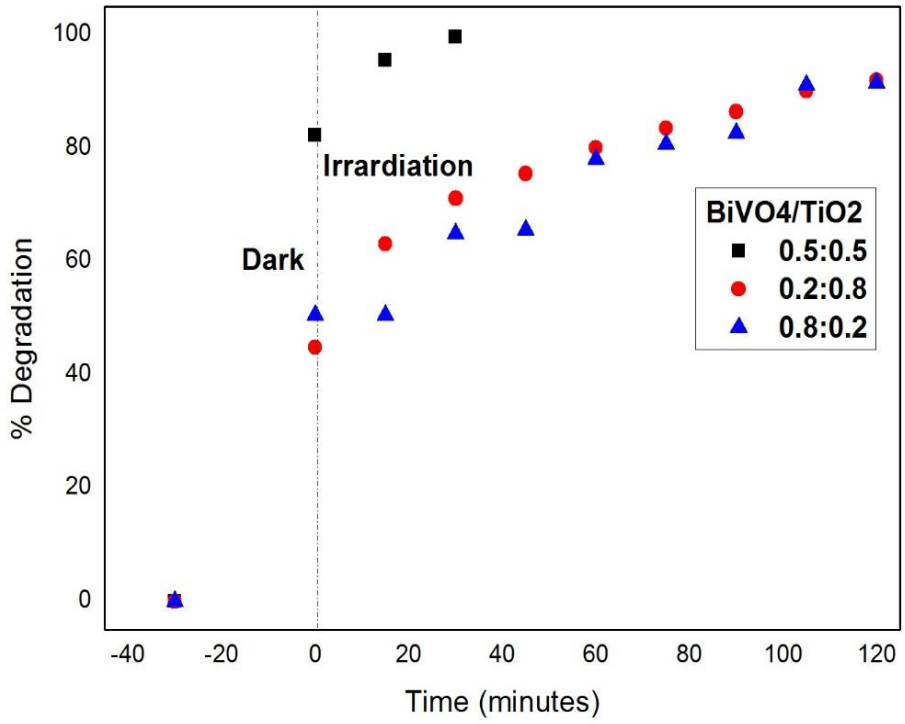

Fig. 5.17 Pc test for choosing the best composite; Methylene blue

For the deposition of the films, we have chosen a best composite considering the efficiency in the organic contaminant degradation. So here methylene blue (MB)was used as a model dye. Fig. 5.17 presents the tests carried out to choose the best sample for the deposition. 0.5:0.5 sample was chosen considering its MB degradation efficiency (fig. 5.17). The whole experiment was carried out for 120 minutes with the nanocomposites, and initially for 60 minutes, the sample-solution was kept under dark for an adsorption-desorption equilibrium. After 60 minutes, the 100ml methylene blue solution with nanocomposite concentration of 1 g/l was kept under irradiation to continue the pc process. The aliquot sample was taken from the solution during each interval.

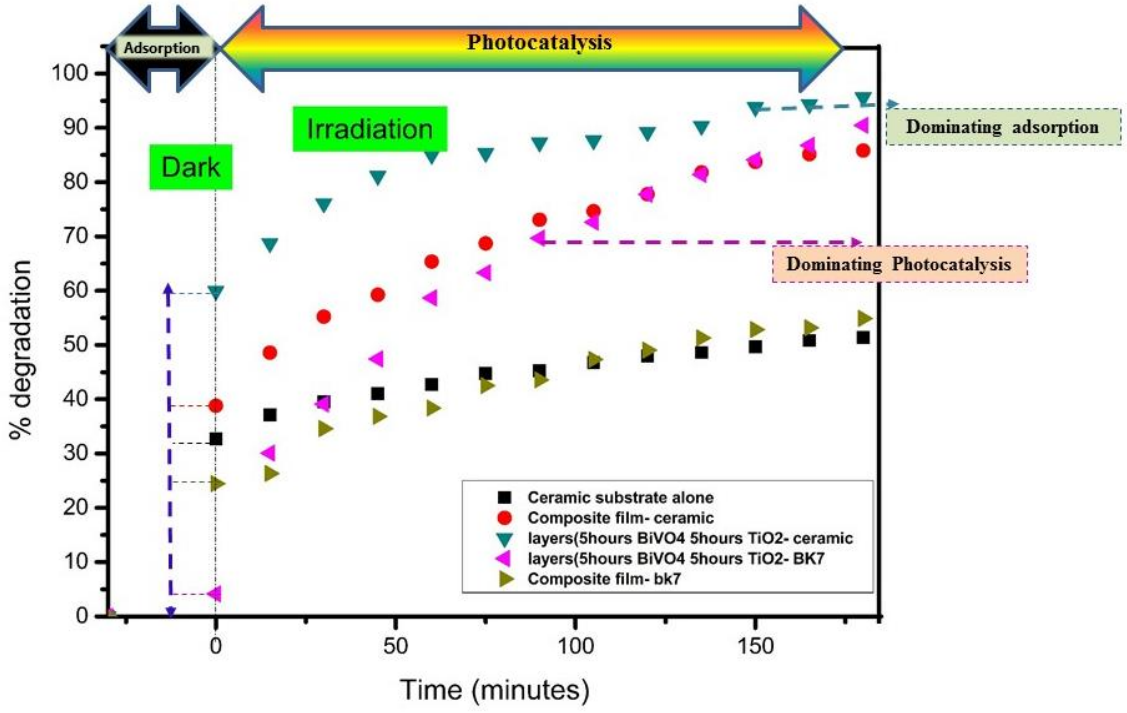

Fig. 5.18. Adsorption - photocatalysis effects in TO/BVO heterostructures deposited on BK7 and ceramic AlPO substrates.

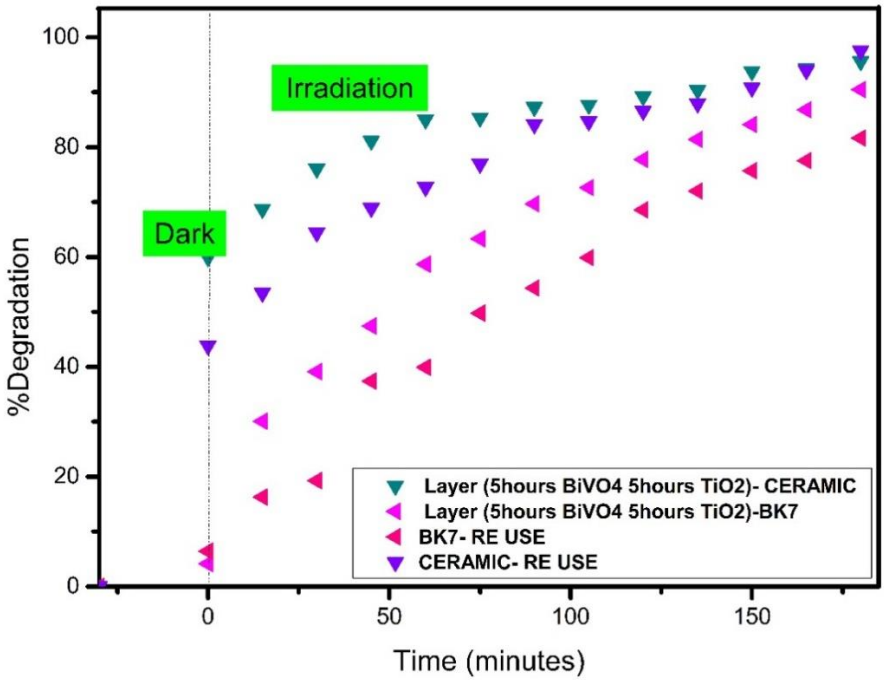

Fig. 5.19. Stability of the films as layered and composites as a function of their re-use in the heterogeneous photocatalysis process.

The degradation efficiency was calculated with the equation [29,30];

$$\% \textbf{ Degradation} = \frac{\mathbf{co-c}}{\mathbf{co}} * \mathbf{100} \qquad \textbf{(6)}$$

The pc degradation of MB was carried out using the deposited films; under the similar conditions used with the nanocomposite powder samples. But the test duration was 180 minutes.

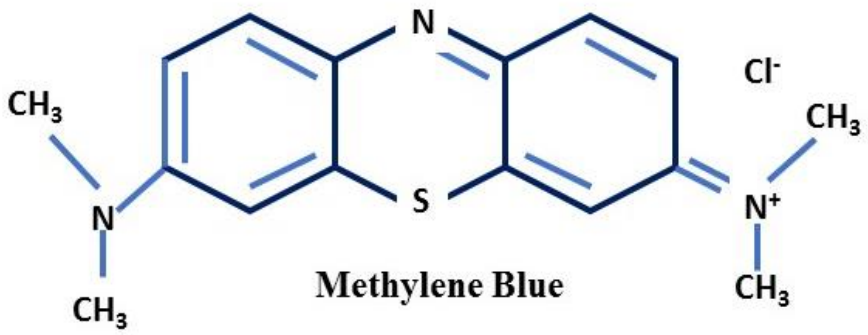

Fig. 5.20 Chemical structure of Methylene blue dye

Adsorption and photocatalysis processes are involved in the pc water treatment and act synergistically for degradation of pollutants from wastewater. The efficiency of these effects depends on the optical properties required for photoactivity and the microstructures of the compounds. In particular, the contact surface with the aqueous environment, the solid surface morphology, and roughness contributes critically to the adsorption-photocatalysis processes. However, while the adsorption effect may consist mainly in the fixation of the organic molecules on the available surface without their elimination, photocatalysis is the key process for the degradation of pollutants and is eco- friendly. The investigations of these phenomenon were carried out on photoactive films considering the band gap engineering of the heterostructures TO/BVO and their microstructures. The efficiency of degradation of the organic groups from solutions by the above processes was investigated and compared as a function of the nature of substrate and films. Fig.5.19 reports the kinetics of organic dye (MB) degradation from solutions based on the adsorption and photocatalysis processes. The degradation process is based on the photogenerated radicals (superoxide, hydroxyl), which cause the splitting of the chemical bonding [31], C-S^{+}=C functional groups and N=C bonds and breaking the aromatic rings of the MB. The pc process is achieved in the case of the complete mineralization of the organic dyes. The adsorption and photocatalysis coexist in the investigated films and show different efficiencies for the MB [32] degradation. For the

layered films on the ceramic substrate, the adsorption under darkness is the dominant process compared to the photocatalysis under simulated solar radiation. This behavior is understood by the high porosity of the ceramic substrate, which also contributes to modulate the microstructure of the deposited film. Contrarily, for the layered film deposited on a flat glass substrate (BK7), the principal process consists of the photocatalysis under irradiation with a high reaction rate and an efficiency of above 90% of MB degradation, which was higher compared to other films [33,34]. For the composite films, the adsorption phenomena is involved for both substrates (ceramic, glass BK7), indicating that the microstructure of composite film favors anchoring sites for MB groups. The efficiency of the visible-light-driven photocatalysis for the degradation of more than 85% of MB is pointed out for the composite film on the ceramic AlPO substrate in contrast to the film grown on BK7 substrate without noticeable effect. Thus, the combination of adsorption and photocatalysis leads to comparable degradation rates for the films deposited on AlPO ceramic substrate irrespective of their organization as a layered or composite film. The situation is of more contrast for the film deposited on the glass BK7 substrate. The layered film shows degradation efficiency at the same level as for films on ceramics. The efficiency of the layered film on BK7 was completely due to the photocatalysis process [35] since the graph itself shows the lesser influence of the adsorption. While the composite film on BK7 show the combined effect of adsorption and photocatalysis. As inferred from xrd studies, the composite film on BK7 shows the largest crystallite size (~28 nm) than in the other films (12 nm). The structural attributes are also indicative of lower crystalline order due to the low temperature of annealing. The impact of the crystallite size is plausibly the reason for the low efficiency on the pollutant degradation for composite films on BK7 substrate.

Many researches have already reported the formation of Type II (staggered) band alignment in the TO/BVO layered films that allows efficient charge transfer between the parent compounds[36,37], where electrons will be transferred between the conduction band of BVO to [38] the TO conduction band may act as an inter-band where the electrons may reside more time before the recombination. This allows enough time for the contaminant degradation by the redox reactions. This fact can be attributed to the case of the layered film deposited on the BK7substrate which has shown better pc efficiency compared to other samples.

Finally, it is worth noting that the films which have shown the best percentage degradation of contaminant that is above 90% (Layered on BK7 and composite on the ceramic) are

relatively stable against several cycles of the adsorption – photocatalysis tests (fig.5.20). The film was washed with de-ionized water before the re-usability tests [39]. The present work contributes to draw the best configurations of heterostructures TO/BVO, which offer good physical properties (morphology, crystalline structure, and suitable band gap) to ensure the best efficiency for environmental applications illustrated here by contaminant degradation.

References

[1] Abegunde, Olayinka Oluwatosin, et al. "Overview of Thin Film Deposition Techniques." AIMS Materials Science, vol. 6, no. 2, pp. 174–99, 2019.

[2] N. Patel *et al.*, "Efficient photocatalytic degradation of organic water pollutants using V–N-codoped TiO2 thin films," *Appl. Catal. B Environ.*, vol. 150–151, pp. 74–81, 2014.

[3] C. T. Tsai, D. S. Chuu, G. L. Chen, and S. L. Yang, "Studies of grain size effects in rf sputtered CdS thin films," *J. Appl. Phys.*, vol. 79, no. 12, pp. 9105–9109, 1996.

[4] Y. Leprince-Wang and K. Yu-Zhang, "Study of the growth morphology of TiO2 thin films by AFM and TEM," *Surf. Coatings Technol.*, vol. 140, no. 2, pp. 155–160, 2001.

[5] M. A. Ruiz-Preciado, A. Bulou, M. Makowska-Janusik, A. Gibaud, A. Morales-Acevedo, and A. Kassiba, "Nickel titanate (NiTiO3) thin films: RF-sputtering synthesis and investigation of related features for photocatalysis," *CrystEngComm*, vol. 18, no. 18, pp. 3229–3236, 2016.

[6] P. Pansila, N. Witit-Anun, and S. Chaiyakun, "Influence of sputtering power on structure and photocatalyst properties of DC magnetron sputtered TiO2 thin film," *Procedia Engineering*, vol. 32. pp. 862–867, 2012.

[7] T. M. Wang, S. K. Zheng, W. C. Hao, and C. Wang, "Studies on photocatalytic activity and transmittance spectra of TiO2 thin films prepared by r.f. magnetron sputtering method," *Surf. Coatings Technol.*, vol. 155, no. 2–3, pp. 141–145, 2002.

[8] V. I. Merupo, S. Velumani, G. Oza, M. Makowska-Janusik, and A. Kassiba, "Structural, electronic and optical features of molybdenum-doped bismuth vanadium oxide," *Mater. Sci. Semicond. Process.*, vol. 31, pp. 618–623, 2015.

[9] S. H. Nam, T. K. Kim, and J. H. Boo, "Physical property and photo-catalytic activity of sulfur doped TiO_2 catalysts responding to visible light," *Catal. Today*, vol. 185, no. 1, pp. 259–262, 2012.

[10] A. Y. Chen *et al.*, "Deposition-rate dependence of orientation growth and crystallization of Ti thin films prepared by magnetron sputtering," *Thin Solid Films*, vol. 574, pp. 71–77, 2015.

[11] N. Areerachakul, S. Sakulkhaemaruethai, M. A. H. Johir, and J. Kandasamy, "Journal of Water Process Engineering Photocatalytic degradation of organic pollutants from wastewater using aluminium doped titanium dioxide," vol. 27, no. December 2018, pp. 177–184, 2019.

[12] L. E. Peng, Z. Yao, Z. Yang, H. Guo, and C. Y. Tang, "Dissecting the Role of Substrate on the Morphology and Separation Properties of Thin Film Composite Polyamide Membranes: Seeing Is Believing," *Environ. Sci. Technol.*, vol. 54, no. 11,

pp. 6978–6986, Jun. 2020.

[13] W. Yu *et al.*, "Enhanced visible light photocatalytic degradation of methylene blueby F-doped TiO 2," *Appl. Surf. Sci.*, vol. 319, no. 1, pp. 107–112, 2014.

[14] I. Ben Jemaa, F. Chaabouni, and A. Ranguis, "Cr doping effect on the structural, optoelectrical and photocatalytic properties of RF sputtered TiO2 thin films from a powder target," *J. Alloys Compd.*, vol. 825, p. 153988, 2020.

[15] A. Arman, Ş. Ţălu, C. Luna, A. Ahmadpourian, M. Naseri, and M. Molamohammadi, "Micromorphology characterization of copper thin films by AFM and fractal analysis," *J. Mater. Sci. Mater. Electron.*, vol. 26, no. 12, pp. 9630–9639, 2015.

[16] M. S. Abdel-wahab, A. Jilani, I. S. Yahia, and A. A. Al-Ghamdi, "Enhanced the photocatalytic activity of Ni-doped ZnO thin films: Morphological, optical and XPS analysis," *Superlattices Microstruct.*, vol. 94, pp. 108–118, 2016.

[17] K. Venkateswarlu, M. Sandhyarani, T.A. Nellaippan, and N. Rameshbabu, "Estimation of Crystallite size Lattice Strain and Dislocation Density of Nanocrystalline Carbonate Substituted Hydroxyapatite by X-ray peak variance Analysis, " Mat. Sci., vol 5, pp. 212–221, 2014.

[18] O. G. Simionescu, C. Romanitan, O. Tutunaru, V. Ion, O. Buiu, and A. Avram, "RF magnetron sputtering deposition of TiO2 thin films in a small continuous oxygen flow rate," *Coatings*, vol. 9, no. 7, pp. 1–13, 2019.

[19] L. Ćurković, D. Ljubas, S. Šegota, and I. Bačić, "Photocatalytic degradation of Lissamine Green B dye by using nanostructured sol–gel TiO2 films," *J. Alloys Compd.*, vol. 604, pp. 309–316, 2014.

[20] L. E. Peng, Z. Yao, Z. Yang, H. Guo, and C. Y. Tang, "Dissecting the Role of Substrate on the Morphology and Separation Properties of Thin Film Composite Polyamide Membranes: Seeing Is Believing," *Environ. Sci. Technol.*, vol. 54, no. 11, pp. 6978–6986, 2020.

[21] W. Yu *et al.*, "Enhanced visible light photocatalytic degradation of methylene blueby F-doped TiO 2," *Appl. Surf. Sci.*, vol. 319, no. 1, pp. 107–112, 2014.

[22] G. Odling and N. Robertson, "BiVO 4 -TiO 2 Composite Photocatalysts for Dye Degradation Formed Using the SILAR Method," *ChemPhysChem*, vol. 17, no. 18, pp. 2872–2880, 2016.

[23] K. Ravichandran, R. Uma, S. Sriram, and D. Balamurgan, "Fabrication of ZnO:Ag/GO composite thin films for enhanced photocatalytic activity," *Ceram. Int.*, vol. 43, no. 13, pp. 10041–10051, 2017.

[24] A. R. Nanakkal and L. K. Alexander, "Graphene / BiVO 4 / TiO 2 nanocomposite : tuning band gap energies for superior photocatalytic activity under visible light," *J.*

Mater. Sci., vol. 52, no. 13, pp. 7997–8006, 2017.

[25] S. Ali *et al.*, "Plasmon aided (BiVO4)x–(TiO2)1−x ternary nanocomposites for efficient solar water splitting," *Sol. Energy*, vol. 155, pp. 770–780, 2017.

[26] M. Mehta, S. Krishnamurthy, S. Basu, T. P. Nixon, and A. P. Singh, "BiVO4/TiO2 core-shell heterostructure: wide range optical absorption and enhanced photoelectrochemical and photocatalytic performance," *Mater. Today Chem.*, vol. 17, p. 100283, 2020.

[27] Y.-R. Lv, C.-J. Liu, R.-K. He, X. Li, and Y.-H. Xu, "BiVO4/TiO2 heterojunction with enhanced photocatalytic activities and photoelectochemistry performances under visible light illumination," *Mater. Res. Bull.*, vol. 117, no. January, pp. 35–40, 2019.

[28] A. S. Bakri *et al.*, "Effect of annealing temperature of titanium dioxide thin films on structural and electrical properties," *AIP Conf. Proc.*, vol. 1788, 2017.

[29] Z. Adlan, M. Hir, P. Moradihamedani, A. H. Abdullah, and M. A. Mohamed, "crossmark," vol. 57, no. January 2016, pp. 157–165, 2017.

[30] J. Singh, S. A. Khan, J. Shah, R. K. Kotnala, and S. Mohapatra, "Nanostructured TiO 2 thin films prepared by RF magnetron sputtering for photocatalytic applications," *Appl. Surf. Sci.*, vol. 422, pp. 953–961, 2017.

[31] A. Ajmal, I. Majeed, R. N. Malik, H. Idriss, and M. A. Nadeem, "Principles and mechanisms of photocatalytic dye degradation on TiO 2 based photocatalysts: A comparative overview," *RSC Adv.*, vol. 4, no. 70, pp. 37003–37026, 2014.

[32] W. Halim, S. Coste, S. Zeroual, A. Kassiba, and S. Ouaskit, "Latex copolymer - assisted synthesis of metal - doped - TiO 2 mesoporous structures for photocatalytic applications under solar simulator," *J. Mater. Sci. Mater. Electron.*, vol. 31, no. 5, pp. 4161–4169, 2020.

[33] R. E. Marotti, P. Giorgi, G. Machado, and E. A. Dalchiele, "Crystallite size dependence of band gap energy for electrodeposited ZnO grown at different temperatures," *Sol. Energy Mater. Sol. Cells*, vol. 90, no. 15, pp. 2356–2361, 2006.

[34] Venkatesan, R., et al. "Nanostructured Bismuth Vanadate ($BiVO_4$) Thin Films for Efficient Visible Light Photocatalysis." Materials Chemistry and Physics, vol. 205, pp. 325–33, 2018.

[35] P. Jongnavakit, P. Amornpitoksuk, S. Suwanboon, and N. Ndiege, "Preparation and photocatalytic activity of Cu-doped ZnO thin films prepared by the sol-gel method," *Appl. Surf. Sci.*, vol. 258, no. 20, pp. 8192–8198, 2012.

[36] A. Houas, "Photocatalytic degradation pathway of methylene blue in water," *Appl. Catal. B Environ.*, vol. 31, no. 2, pp. 145–157, 2001.

[37] O. Monfort *et al.*, "Journal of Environmental Chemical Engineering Photooxidative

properties of various BiVO 4 / TiO 2 layered composite fi lms and study of their photocatalytic mechanism in pollutant degradation," vol. 5, pp. 5143–5149, 2017.

[38] X. Li, Z. Zhang, F. J. Zhang, J. Liu, J. Ye, and W. C. Oh, "Synthesis and photocatalytic activity of TiO2/BiVO4 layered films under visible light irradiation," *J. Korean Ceram. Soc.*, vol. 53, no. 6, pp. 665–669, 2016.

[39] Z. Zhu, Q. Han, D. Yu, J. Sun, and B. Liu, "A novel p-n heterojunction of BiVO4/TiO2/GO composite for enhanced visible-light-driven photocatalytic activity," *Mater. Lett.*, vol. 209, no. 3, pp. 379–383, 2017.

CHAPTER. 6

Conclusion

Visible light photoactive TO/BVO nanocomposite ratios were synthesized using a modified sol-gel methodology, which is a low-temperature processes that ensured the homogeneity and purity of the final products. The synthesized particles had homogeneous morphology with a high crystalline nature, exhibiting excellent visible light response with a reduced bandgap with photocatalytic activities within the visible light region. The effective bandgap of the composite showed a redshift as the BVO concentration increased. The TEM characterization of the composite structures supported results on the preferential orientations observed from the X-ray diffractograms. The slab models showed alternating bright and dark signal channels due to the monoclinic (211) and tetragonal (004) plane stacking generated during the grain growth, the overlapping planes from both BVO and TO, supporting the heterojunction formation. The measured bandgap values showed a marginal decrease in BVO content increases within the composition. The BET surface area measurement for the nanocomposites from morphological studies also exhibited slight increase as the BVO content increased.

The study investigated the nanocomposite material's performance using different TO/BVO compositions under visible light for degrading organic dyes. The results showed that decreased BVO content improves the composite's efficiency for the degradation of AB113 dyes, attributed to the low pc activity of BVO due to the fast recombination of the photogenerated electron-hole pairs. The electrochemical impedance analysis measuring the nanocomposites' flat band potential showed that 0.8:0.2 nanocomposite exhibited comparatively higher negative value for the flat band potential (V_{fb}=-1.01eV), which further indicates a lower conduction band minimum. Consequently, a reduced charge barrier separation occurs and enhances the composite's pc efficiency by improving the charge transfer process. Contrarily, the observed small crystallite size favors forming a heterojunctions area that supports charge transfer and enhances photogenerated charge carriers' lifetimes. The TO:BVO nanocomposites' optimal performance exhibited complete removal of AB113 dye under simulated visible light without any additional scavengers.

The studies on arsenic removal with the aid of Stratigraphic software using RSM methodology and other optimized parameters (pH, nanocomposite dosage) elucidated the performance of different TO/BVO sample compositions. The nanocomposite ratio of 0.8:0.2

showed lower performance towards the As removal process owing to the slightly high composition of BVO, thereby justifying further modification/optimization of the ratios. A TO/BVO nanocomposite with a %BVO of 1.5-2% yielded complete removal of As within 60 minutes of irradiation in the desired spectral region.

TO/BVO films' deposition using the RF-sputtering technique aimed at tackling common challenges posed by powder catalysts and potentially realizing high surface area with a particular interest for the expected pc activities. The sputtered layered films showed mesoscopic heterostructures with good crystalline behavior that enhances the charge transport and higher concentration of photogenerated charge carriers. The layered film had a bandgap of 2.48 eV, while the composite film has a bandgap of 2.95eV.

The sputtered films demonstrated nearly 95% degradation of the Methylene blue dye within 180 minutes of visible light radiation and a good response towards the reusability tests with the degradation of more than 80% within the same period of 180 minutes. The comparative study with substrates showed that ceramic substrate offers more adsorption support, attributed to the high porous organization of the constitutive alumino-phosphate media. In contrast, the BK7 glass substrate offers good photocatalytic efficiency and a relatively low adsorption effect and underlines its suitability for reusing cycles.

In summary, the present work has contributed to relevant architectures as efficient photocatalysts made by nanocomposites and heterostructures associating photoactive oxides of TO and BVO. Optimized features with crystalline structures for BVO and TO, high crystallinity of heterostructures, and reduced bandgap ensure efficient photocatalysts for the water remediation from pollutants such as organic groups and heavy metals.

Specific Conclusions:

- A sol-gel methodology was employed to synthesize the nanocomposites of TO/BVO with different stoichiometry. Two sets of nanocomposites were prepared with TO:BVO ratios, 0.2:0.8, 0.5:0.5, and 0.8:0.2. Structural, morphological, optical, and electrochemical analyses have been performed. The nanocomposites used for the contaminant degradation studies, with AB113 as a model organic contaminant yielded complete removal of the contaminant in 20 minutes of irradiation

- Other compositions were synthesized due to the above composites' low efficiency in As removal, the nanocomposites having a low weight percentage of BVO (%BVO=

0.5, 1, 1.5, 2, and 2.5). These composites show structural and morphological behavior similar to the above-considered ratios in point 1. The resultant synthesized nanocomposites showed complete removal of the As ions within 1 hour of irradiation. The pc test parameters were optimized using an experimental design procedure such as the Response Surface Method investigated in this work.

- The improvement of material processing and electronic bandgap engineering was carried out using films as composites with a high area of mesoscopic interfaces TO/BVO and alternatively as stacked layers TO on BVO/substrate. The deposition parameters were optimized to ensure suitable properties, and deposited films were subsequently analyzed for crystalline phases, the surface parameters and morphology, and optical features. Heterogeneous photocatalysis tests were realized on model solutions charged by organic dyes (Methylene blue as the model). Combined adsorption-photocatalysis were demonstrated with an emphasis on the role of the substrate on the reactional processes. Overall, 90-95% of the degradation was observed from the quasi-pure photocatalysis process for BK7 glass substrates, while a dominant adsorption mechanism occurred for AlPO ceramics, favored by their mesoporous structures.

List of Figures

Figure Number	Caption	Page Number
Fig. 1.1	Top 10 global risks in the next ten years; Global risk reports World economic forum 2020	2
Fig. 1.2	Different Oxide photocatalysts with band gap and energy levels of VB and CB compared to the redox potential of water.	4
Fig.1.3	Photons induced formation of electron-hole pairs in a SC material followed by the migration of charges to the SC surface where redox reactions occur.	5
Fig. 1.4a	Band edge positions of different semiconductors (pH = 0)	8
Fig. 1.4b	Band edge positions of TiO2 and BiVO4 at higher pH =12	8
Fig. 1.5	Photocatalysis scheme for coupled semiconductors system	10
Fig. 1.6	a) Rutile b) Anatase and c) Brookite phases of Titanium dioxide	11
Fig. 1.7	Electronic energy diagram of the monoclinic phase of BVO showing the possibility of visible light absorption	12
Fig. 1.8	(a)Tetragonal- scheelite structure b) Tetragonal- Zircon structure [Red; Vanadium, Purple; Bismuth, Grey; Oxygen. The Monoclinic- scheelite structure is very similar to tetragonal scheelite as in (a) with the exception of the changes in the atomic positions of each atom of Bi, V, and O	13
Fig. 2.1	Sol-gel Synthesis steps	24
Fig. 2.2	Plassys MP300 RF sputtering equipment	25
Fig. 2.3	Schematic representation of the sputtering process	25
Fig. 2.4	Schematic of the RF- sputter deposition of the films	27
Fig. 2.5	Illustration of the principle of xrd	28
Fig. 2.6	PANalytical Empyrean X-ray diffractometer	28
Fig. 2.7	WiTech Raman spectrometer	29

Fig. 2.8	Principle of Raman spectrum	30
Fig. 2.9	Representation of molecular scatterings	30
Fig. 2.10	Agilent Carry v-670 Spectrophotometer	31
Fig. 2.11	SEM-VEGA3 (CINVESTAV)	33
Fig. 2.12	JEOL JEM 2100 HR TEM (Jeol ltd.) (IMMM)	34
Fig. 2.13	FFT of a) amorphous and b) crystalline samples	35
Fig. 2.14	AFM- T-MDT, NTEGRA	36
Fig. 2.15	Dektat XT profilometer- with schematic diagram	37
Fig. 2.16	Quantachrome Absorber 1	38
Fig. 2.17	Autolab PGSTAT 302N Potentiostat	39
Fig. 2.18	Pc experimental set-up	40
Fig. 2.19	Calibration curve- Absorbance Vs Concentration	41
Fig.2.20	Plot of the reactant concentration versus time for a first order process	42
Fig. 3.1	Scheme of Method.1tried for the synthesis of the nanocomposites with desired crystalline phases	45
Fig. 3.2	Scheme of Method.2tried for the synthesis of the nanocomposites with desired crystalline phases	46
Fig. 3.3	Xrd patterns of the nanocomposites a) before and b) after calcination, compared with those of pure anatase TO (JCPDS 00-021-1272) and sol-gel synthesized BVO (JCPDS-00-075-1866). Before the calcination of the samples, the refinement of the patterns shows the formation of the orthorhombic phase of BVO.	48
Fig. 3.4	Raman spectra for nanocomposite samples (The Raman measurements show noticeable changes as a function of the composition of TO and BVO.	50
Fig. 3.5	SEM images of the samples before and after calcination 0.2:0.8, 0.5:0.5 and 0.8:0.2 - a,c,e) before calcination b,d,f) after calcination respectively	51
Fig. 3.6	Comparison of the bandgap energy of the synthesized nanocomposite samples with Anatase TO and synthesized	52

	monoclinic BVO nanoparticles with the Tauc plot in the inset.	
Fig. 3.7A	Micrographs of the 0.8:0.2 nanocomposite a) TEM micrograph of the whole area b) Selected area from the sample c) FFT diffraction pattern d) EDS chemical analysis e) Mapping of the samples	53-54
Fig. 3.7B	Micrographs of the 0.5:0.5 nanocomposite a) TEM micrograph of isolated particles b,c) bright and dark field analysis d) Mapping analysis of the sample e) FFT diffraction pattern f) elemental mapping and f)EDS analysis respectively	55
Fig. 3.7C	Micrograph of the nanocomposite 0.2:0.8 a) isolated particles b) bright-field image c) dark field image, d) FFT diffraction pattern	56
Fig. 3.8	TEM micrograph, FFT planes, and simulated crystalline models for the 0.8:0.2 composite. Regions A, B, and C correspond to pure BVO, TO anatase, and the junction of both crystalline phases, respectively	57
Fig. 3.9	Pc degradation of AB113 (a) Adsorption and self-degradation plots along with the comparison of pc activity of TO, BVO and the three nanocomposite ratios $[AB113]_0$= 40 mg/l, [nanocomposite, TO, BVO] = 1g/l pH_0=6. (b) $[AB113]_0$= 40 mg/l, [nanocomposite]= 1-5g/l pH_0=6 (c) Comparison of the activity of TO (Both adsorption and photocatalysis)	60
Fig. 3.10	The preliminary AB113 degradation test by each sample [Dosage] = 5g/l $[C_0]$ = 40mg/l	61
Fig. 3.11	Mott–Schottky curves of (a) BVO and TO and (b) TO/ BVO nanocomposites (0.8:0.2, 0.5:0.5 and 0.2:0.8 compositional ratio BVO: TO). The C_{sc} were obtained at 100 Hz in 0.05 M $NaClO_4$ aqueous solution	62
Fig. 3.12	Energy diagram proposed for TO/ BVO nanocomposites (0.8:0.2, 0.5:0.5 and 0.2:0.8 compositional ratio BVO: TO)	63

Fig. 3.13	Time evolution of the open circuit potential (OCP) in the dark (off) and under UV illumination (on) for the synthetized nanocomposites.	65
Fig. 3.14	Illustration of the circumstance that backs the synthesis of new set (Set B) of nanocomposites for the Arsenic (III) oxidation/removal	66
Fig. 4.1	Representation of the output from the 20 sets of experiments	78
Fig. 4.2	Standard pareto chat on the effect of the parameters on the process	78
Fig. 4.3	Response surface for different parameters	79
Fig. 4.4	a) X-ray diffractograms of the nanocomposites with the pristine materials b) Raman spectra of the samples c) Band gap analysis of the samples	80
Fig.4.5	a) SEM micrograph of the nanocomposite b) Mapping analysis c) Mapping analysis of the nanocomposite with 2%BVO d) EDS Chemical analysis	83
Fig.4.6	a) BET-Surface area analysis of the modified samples (in the inset Surface area vs. %BVO plot) b) Pore volume analysis of the samples	84
Fig.4.7	Calibration curves for AS(III) and As(V)	86
Fig.4.8	Comparison of the removal efficiency of nanocomposites with BVO= 1.5 & 2%, BVO and TO	87
Fig.4.9	Percentage removal of Arsenic total using optimized nanocomposite with BVO=2%. In the inset: percentage oxidation of As(III) to As(V)	87
Fig.4.10	Aliquot simples taken during different time intervals; under optimized conditions	89
Fig. 5.1	X-ray diffractogram for the identification of the AlPO Ceramic substrate material	96
Fig. 5.2	X-ray diffractograms of the composite film deposited under different chamber atmosphere	97
Fig. 5.3	X-ray diffractogram of the nanocomposite deposited at different incident power	99

Fig. 5.4	In-situ annealing X-ray diffractogram of the nanocomposite film (Optimization of the annealing temperature)	100
Fig. 5.5	X-ray diffractogram of the layered films over a) Ceramic and b) BK7 substrates compared to the fitted data from High score software.	101
Fig. 5.6	X-ray diffractogram of the Nanocomposite films deposited on Ceramic and BK7 substrates with the assignment of the Xrd lines to well defined crystalline structures.	102
Fig. 5.7	Dislocation density and lattice strain vs. Crystallite size	103
Fig. 5.8	Raman spectra of the layered films	105
Fig. 5.9	Raman analysis of the nanocomposite films	106
Fig. 5.10	Tauc- plot for the different RF-sputtered films with different compositions as BVO, TO, and TO/BVO heterostructures deposited over the BK7 substrate.	107
Fig. 5.11	TEM Micrograph of the films deposited over BK7 substrates a) Layered film b) Planes from the layered film c) Composite film d) Cropped planes from composite film e,f) FFT of the layered and composite films respectively	108
Fig. 5.12	TEM Micrograph of the films deposited over Ceramic substrates a) Layered film b,c)Cropped planes d) Composite ceramic film e) Cropped planes from the composite film f,g) FFT from the layered and composite films respectively	109
Fig. 5.13	a) Composite-BK7 b) Layered film-BK7	110
Fig. 5.14	c) Composite film-Ceramic substrate d) Layered film-Ceramic substrate	111
Fig. 5.15	a) Thickness measurement for the layered film b) Thickness measurement for the nanocomposite film	112
Fig. 5.16	a) Morphology of the layered film deposited on BK7 substrate by AFM- both a) 2D and b) 3D images, respectively, are illustrated b) Morphology of the composite film deposited on BK7 substrate by AFM- both a) 2D and b) 3D images, respectively	113

Fig. 5.17	Pc test for choosing the best composite; Methylene blue	114
Fig. 5.18	Adsorption-photocatalysis effects in TO/BVO heterostructures deposited on BK7 and ceramic AlPO substrates.	115
Fig. 5.19	Stability of the films as layered and composites as a function of their re-use in the heterogeneous photocatalysis process.	115
Fig. 5.20	Chemical structure of Methylene blue dye	116

List of Tables

Table Number	Caption	Page Number
Table 3.1.	Calculated crystal properties of the nanocomposite after calcination	49
Table 3.2	Calculated band gaps of BVO, TO, and its various nanocomposites	53
Table 3.3.	Flat band potential of synthetized materials.	63
Table. 4.1	Levels of the parameters studied in the Central Composite Design (CCD)	73
Table. 4.2	20 sets of experiments with different levels of Parameters (LE) (Input)	74
Table 4.3	Statistical analysis of vaiance (ANOVA) the input parameters	76
Table 4.4	Results of the 20 sets of experiments (Output)	77
Table 4.5.	factor Central Composite Design (CCD) matrix and the value of the response function	78
Table 4.6	FWHM and Crystalline size calculation	81
Table 4.7	Bandgap values of the nanocomposites and their components	82
Table 4.8	Comparison of some existing research on Arsenic removal	89
Table. 5.1	Structural parameter of the films.	102
Table.5.2	Percentage Composition of BVO & TO calculated using the integrated intensity of the peaks	104
Table.5.3	Calculated grain size from TEM micrographs	111

Titre : Synthèse et Propriétés Photocatalytiques des Nanocomposites et Hétérostructures $TiO_2/BiVO_4$

Mots clés : oxides Photoactifs, $TiO_2/BiVO_4$, Hétérostructures, Nanocomposites, Photocatalyse,

Résumé : Les travaux de thèse contribuent au développement de matériaux photocatalyseurs à base de $BiVO_4$ (BVO)/TiO_2 (TO) sous forme de nanocomposites et d'hétérostructures. Ces architectures sont dédiées à des applications photocatalytiques en lumière visible pour la dépollution de l'eau. Le choix des hétérostructures TO/BVO repose sur la compatibilité de la structure de bandes électroniques des composés pour des processus photcatalytiques. En particulier, on s'attend à ce qu'un alignement de bandes des hétérostructures de type II des phases BVO et TO favorise le transfert de charge entre les structures améliorant la durée de vie des porteurs de charge et donc l'efficacité des processus photocatalytiques.

Une importante contribution expérimentale a porté sur la synthèse par la méthode Sol-gel des nanocomposites TO/BVO avec différents taux des deux oxydes et des traitements thermiques pour favoriser les phases cristallines de TO (anatase) et de BVO (monoclinique scheelite). Les études structurales, morphologiques et celles portant sur les propriétés électroniques, optiques et électrochimiques ont été effectuées grâce aux méthodes de caractérisations (DRX, Raman, SEM, MET, Spectrométrie UV-Vis..).

La réalisation de composites avec des hétérojonctions aux dimensions mésoscopiques entre les deux constituents BVO et TO a bien été démontrée. La deuxième méthode de synthèse a porté sur la réalisation d'hétérostructures TO/BVO déposées par pulvérisation radiofréquence (rf) en utilisant différents substrats et selon deux configurations (bi-couches BVO/TO, films composites). L'optimisation des caractéristiques des films (cristallinité, états de surfaces) a nécessité des essais sur plusieurs facteurs tels que la pression dans l'enceinte de dépôt, la puissance, la nature des substrats et les températures de recuit. Les méthodes de caractérisation ont été utilisées pour l'analyse approfondie des caractéristiques des films en fonction des configurations considérées (composites, bi-couches) ainsi que de la nature des différents substrats. Les matériaux nanocomposites et les films TO/BVO ont fait l'objet d'études photocatalytiques appliquées au problème de l'assainissement de l'eau par la dégradation de colorants organiques ou l'oxydation de métaux lourds tels que l'arsenic. L'efficacité des procédés photocatalytiques a été comparée en fonction des caractéristiques des matériaux selon les configurations nanocomposites ou hétérostructures en films minces.

Titre : Synthesis and Photocatalytic properties of $TiO_2/BiVO_4$ Nanocomposites and Heterostructures

Keywrods : Photoactive oxides, $TiO_2/BiVO_4$, Heterostructures, Nanocomposites, Photocatalysis,

Abstract: The thesis work contributes to the development of pc materials based on TO/ BVO (TiO_2/ $BiVO_4$) abbreviated as (TO/BVO) nanocomposites and heterostructures. These architectures are dedicated to harvest the visible light with the aim of remediation processes for water treatment by pc processes. The relevance of the heterostructures TO/BVO for efficient pc processes can be apprehended by the model of the electronic band structures alignment. In particular, a type II band alignment at the interfaces of BVO and TO phases is expected to facilitate the charge transfer between the structures enhancing the lifetimes of charge carriers as required for efficient pc processes. An important experimental contribution was first devoted to the synthesis by the Sol-gel method of TO/BVO nanocomposites by varying the ratio between BVO and TO and performing different annealing treatments to ensure the stabilization of the required crystalline structures. The characterization studies were realized and deep analysis of the physical features was achieved on the considered materials architectures including structural, optical, morphological and electro-chemical properties by using characterizations methods (XRD, Raman, SEM, TEM, UVi-Vis Absorption,).

For the nanocomposite materials, the formation of mesoscopic heterojunctions was clearly demonstrated at the interfaces of BVO and TO phases. The second synthesis approach consists in thin films processing as heterostructures TO/BVO deposited by radio-frequency (rf) sputtering according to two configurations (double-layers, composites). on selected substrates. The optimization of rf-the film features (crystalline quality, surfaces states) required tests on different parameters such as the chamber atmosphere, deposition rate, substrates, and the annealing temperatures. Characterization methods were used for in depth analysis of the films features as function of the considered deposition configuration (composites, double-layers) as weel as the effect of the substrate nature. The nanocomposites materials and the heterostructures deposited as thin films were applied in pc studies devoted to the water remediation by the organic dyes degradation and by the oxidation of heavy metals such as As(III). The efficiency of the pc processes was compared on the different materials configurations such as nanocomposites and layered heterostructures with an emphasis on the role of the substrates.